IMAGE ANALYSIS & STEREOLOGY

formerly ACTA STEREOLOGICA

Journal Mission Statement. Image Analysis & Stereology is the official journal of the International Society for Stereology. It promotes the exchange of scientific, technical, organizational and other information on the quantitative analysis of data having a geometrical structure, including stereology, differential geometry, image analysis, image processing, mathematical morphology, stochastic geometry, statistics, pattern recognition, and related topics. The fields of application are not restricted and range from biomedicine, materials sciences and physics to geology and geography.

Publications. The journal publishes three types of papers. First, original research papers (full-length research papers and short communications) pertaining to various aspects of image analysis and stereology and related quantitative methods for geometric structures, texture and patterns, from instrumentation to computational and statistical methods, mathematics and stochastic geometry, both theoretical and applied. Second, review articles written in a form understandable to a non-specialist. Third, book reviews, news, communications and notes pertaining to the life and work of stereologists and their organizations. Prospective authors of the third type of publications should contact the Editorial Office before submission of a manuscript.

This journal is regularly indexed or abstracted in: Chemical Abstracts, Current Contents®/Engineering Computing and Technology, Current Index to Statistics (CIS), DOAJ, EBSCO, INSPEC, Journal Citation Reports/Science Edition, Math Reviews, MATH-SciNet, METADEX, Referativnyj Zhurnal, Science Citation Index Expanded (SciSearch®), SCOPUS, Web of Knowledge, and Zentrallblatt MATH.

The Journal **Impact Factor** for 2012 is **0.639**.

The journal's owner is the Slovenian Society for Stereology and Quantitative Image Analysis. The Journal is financially supported by the International Society for Stereology and the Slovenian Book Agency.

Apart from potential supplementary material the electronic version of papers is identical to the printed version. **In the case of any discrepancies the electronic version is treated as reference.**

Price and Subscription Conditions
The journal is issued three times yearly. Annual subscription price (excluding bank charges) is €76 for European countries and €97 outside Europe. The journal subscription is included in the basic, student or emeritus ISS membership. All payments should be addressed to Slovenian Society for Stereology and Quantitative Image Analysis, Korytkova 2, SI-1000 Ljubljana, Slovenia. Payment are acceptable by a bank to bank transfer to the Society's account at *NOVA LJUBLJANSKA BANKA, d.d., Ljubljana,*
IBAN: SI56020140015049611, S.W.I.F.T. Code: LJBASI2X
with obligatory notification "*NN for Image Analysis & Stereology*". Please mail a copy of the receipt for the money transfer order to the Editorial Office.

Copyright/Off-prints
Authors submitting a manuscript to Image Analysis and Stereology do so on the understanding that if it is accepted for publication, exclusive copyright of the paper shall be assigned to the journal. There will be no limitation on the personal freedom of the author to use material contained in the paper in other works. No free off-prints are available, but they may be ordered by the authors at extra cost according to the special price list that will be sent to the authors together with an order form.

Printed by Littera picta d.o.o., Rožna dolina, c. IV/32/34, Ljubljana, Slovenia.

Editorial Office

Image Analysis and Stereology Editorial Office
Institute of Anatomy, Medical Faculty, Korytkova 2
SI-1000 Ljubljana, Slovenia
Phone: +386-1-543-7300
Fax: +386-1-543-7301

IAS@mf.uni-lj.si (all inquiries)
Editor.IAS@mf.uni-lj.si

http://www.ias-iss.org

Inquiries

Please contact the Editorial Office for

- ❑ general inquiries
- ❑ subscription
- ❑ requests for permission to reproduce figures, tables and articles
- ❑ information on purchasing reprints of articles
- ❑ manuscript inquiries

Image Anal Stereol is listed in the Registry of Accredited Publications under the registration number 656. Revija Image Anal Stereol je vpisana v Razvid medijev pri Ministrstvu za kulturo pod številko 656. Naklada: 400 izvodov

CONTENTS

Original research papers

Image Anal Stereol 2013;32:65-75 doi:10.5566/ias.v32.p65-75
Original Research Paper

QUANTITATIVE CHARACTERIZATION OF MICROSTRUCTURE OF PURE COPPER PROCESSED BY ECAP

ONDŘEJ ŠEDIVÝ✉,[1], VIKTOR BENEŠ[1], PETR PONÍŽIL[2], PETR KRÁL[3] AND VÁCLAV SKLENIČKA[3]

[1]Department of Probability and Mathematical Statistics, Faculty of Mathematics and Physics, Charles University in Prague, CZ-18675 Prague, Czech Republic; [2]Department of Physics and Material Engineering, Faculty of Technology, Tomas Bata University in Zlín, CZ-76272 Zlín, Czech Republic; [3]Institute of Physics of Materials, Academy of Sciences of the Czech Republic, CZ-61662 Brno, Czech Republic
e-mail: sedivy@karlin.mff.cuni.cz, benesv@karlin.mff.cuni.cz, ponizil@ft.utb.cz, pkral@ipm.cz, sklen@ipm.cz
(Received August 9, 2012; revised February 4, 2013; accepted March 17, 2013)

ABSTRACT

Orientation imaging microscopy (OIM) allows to measure crystallic orientations at the surface of a material. Digitalized data representing the orientations are processed to recognize the grain structure and they are visualized in crystal orientation maps. Analysis of the data firstly consists in recognition of grain boundaries followed by identification of grains themselves. Knowing the grain morphology, it is possible to characterize the grain size homogeneity and estimate structural parameters related to the physical properties of the material. The paper describes methods of imaging and quantitative characterization of the grain boundary structure in metals based on data from electron backscatter diffraction (EBSD). These methods are applied to samples of copper processed by equal-channel angular pressing (ECAP).

Keywords: electron backscatter diffraction, equal-channel angular pressing, random marked sets, second-order analysis.

INTRODUCTION

In microstructural research of metallic materials, methods allowing direct evaluation of the grain structure are often limited to investigation of 2D sections. Planar quantities are used to estimate parameters of the original 3D structure with usual stereological methods. One general limitation is that the estimators of the structural parameters are highly influenced by the resolution given by the grid step of the subsample where the measurements are provided. On the other hand, given the experimental setting, one has comprehensive information about the orientations in grains and disorientations in grain boundaries which can be further analysed with various methods. This paper presents basic principles of processing data from 2D scanning electron microscopy (SEM), describes methods of quantitative characterization of the observed microstructure based on second-order analysis of random marked sets and demonstrates the methods on particular samples.

To describe the structure of polycrystalline materials, modern attitude consists in the characterization of different types of boundaries present in the material and their connectivity in the grain boundary network (Rohrer, 2011). With data from 3-dimensional electron backscatter diffraction (EBSD; Calcagnotto *et al.*, 2010; Wilkinson and Britton, 2012) it is possible to explore the entire 5-parametrical distribution of the grain boundaries where three parameters are related to the disorientation and the other two represent orientation of the interface plane. Despite of limitations of 2-dimensional observations, it still provides great potential for statistical analysis and it allows to process greater amount of observations than space- and time-consuming 3D methods. It is also possible to estimate the 3-dimensional microstructure on the basis of statistical analyses of the data obtained from the 2-dimensional EBSD.

Electron backscatter diffraction is a scanning electron microscope (SEM) based technique which has become well known as a powerful and versatile experimental tool for materials scientists, physicists, geologists and other scientists and engineers (Randle, 2009). It allows the measurement of microtexture (Jiang *et al.*, 2008), microstructure quantification (Bastos *et al.*, 2006), grain and phase boundary characterization (Randle *et al.*, 2008), phase identification (Perez *et al.*, 2006) and strain determination (Britton and Wilkinson, 2012) in crystalline multiphase materials of any crystal structure.

The aim of the present paper is a systematic characterization of Cu processed by equal-channel angular pressing (ECAP) before creep testing. The creep behaviour of ECAPed materials probably belongs to the fewest examined properties of materials processed by ECAP. Creep behaviour was usually investigated in materials which were prepared by severe plastic deformation (SPD) technique at room temperature. For this reason, the creep tests were performed at higher temperatures than the processing temperature of SPD technique was. It is generally accepted that tensile samples are put into the furnace interior and then heated to the creep temperature. It is important to note that each specimen was heated to the testing temperature in the furnace of the creep testing machine up to creep temperature. For this reason, the microstructure is statically annealed and significantly influenced by temperature-induced changes like grain growth, recovery, recrystallization etc.

The systematic characterization of microstructure in Cu specimens processed by ECAP before loading can be important for better understanding of the unusual creep behaviour of ECAPed Cu (Dvořák *et al.*, 2010). Despite of extensive interest in SPD material, there is no systematic work describing real microstructure of ECAP materials before loading when testing temperature in the creep testing machine was reached and stabilized.

To describe the microstructure, statistical methods characterizing spatial distribution of the boundaries marked by their disorientations are introduced. They basically work with a single mark determined by the disorientation angle θ but even more complex information about the disorientation can be used by distinguishing different types of "special" boundaries. The methods are applied on samples of copper processed by ECAP followed by annealing with different times and temperatures. Effect of different number of passes on the grain structure was examined in previous studies (Ilucová *et al.*, 2007; Král *et al.*, 2011).

The rest of the paper is organized as follows. The next section describes the experimental set-up including preparation of the samples and their microscopical observations. The following section introduces basics of image processing of these observations. Further, the processed data are used for quantitative analysis of grain boundaries and this analysis is followed by numerical results. Conclusions are made in the final section.

EXPERIMENTAL BACKGROUND

The microstructure of specimens was examined by scanning electron microscope Jeol 6460 equipped with an EBSD unit operating at an accelerating voltage of 20 kV with specimen tilted at 70°. Results presented in the paper come from the research of copper (99.99% purity) processed by ECAP which involves pressing of a sample through a die within a channel that is bent into an L-shaped configuration (Fig. 1).

The billets in the cast state with 10 mm × 10 mm cross section and 60 mm length were processed by ECAP at room temperature using a die with two perpendicular channels. Each billet was processed by a selected number of ECAP passes. The ECAP was performed using route Bc (Furukawa *et al.*, 1998) in which the billet was rotated around the longitudinal axis by 90° clockwise between the passes. Each pass corresponds to an additional strain value approximately equal to 1. After ECAP, billets were annealed at 373 K, 423 K, 473 K or 573 K for 10 hours. The microstructure analyses were focused on samples processed by 8 ECAP passes. The microstructure changes of pure Cu (99.99%) processed by 8 ECAP passes occurring during the annealing caused considerable decrease of hardness (Fig. 2).

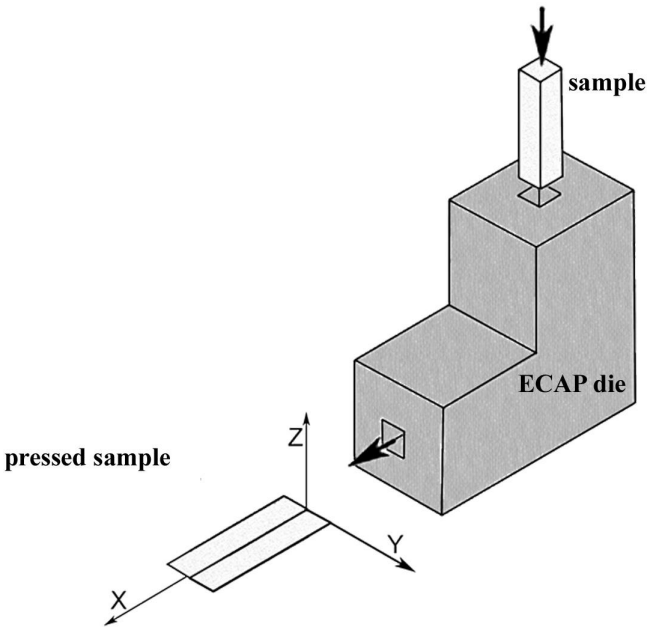

Fig. 1. *Scheme of equal-channel angular pressing (ECAP) facility with definitions of the directions X, Y and Z. A sample of metallic material is pressed through an L-shaped channel.*

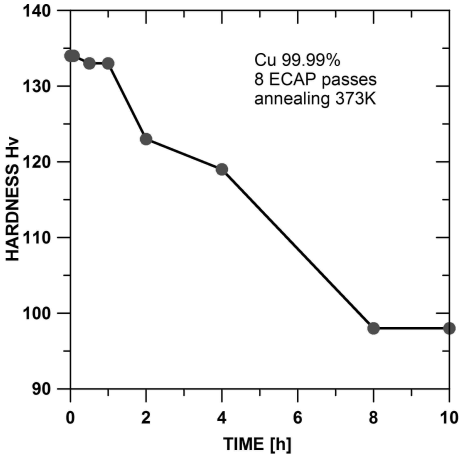

Fig. 2. *Hardness of Cu processed by 8 ECAP passes and annealed at 373 K up to 10 h.*

The specimens for microstructure analyses were cut using electro spark process in an oil bath which minimalizes the effect of deformation and temperature on the surface. The specimens were grinded by 600–4000 SiC paper and water was used as the lubricant during grinding. The specimens were grinded by 600 SiC paper until their surfaces were flat. The surfaces of grinded specimens were checked by light microscope Neophot 32. The specimens were rotated by 90° between subsequent grinding steps and grinded perpendicular to the scratches which were created in the former grinding step until these scratches disappeared. Last grinding step was performed using 4000 SiC paper in order to reduce time of electrolytic polishing. It is generally accepted that electropolishing is a widely used method for final step preparation because it removes the strains induced by mechanical grinding. Finally, the specimens were electropolished using 250 ml phosphoric acid, 250 ml ethanol, 50 ml propylalcohol and 500 ml water for 60 s at room temperature.

All the three cross sections XY, XZ and YZ were examined but the analyses were especially focused on the section XZ. The area from which the EBSD patterns is acquired with an electron beam focused on a 70° tilted sample, is approximately elliptical (Humphreys, 2001). For this reason, resolution perpendicular and parallel to the tilt axis can be distinguished, see Fig. 3 in Humphreys (2001). The major axis, which is perpendicular to the tilt axis, is about three times longer than the minor axis.

The electron beam is deflected and the orientation data are acquired and stored in each point of selected area. The point-to-point step size is based on the expected microstructure and examined size region. In the present work, the size of the image window was selected as 128×96 μm and the step of the EBSD was ~ 0.5 μm for the annealed specimens and these parameters were 40×30 μm and ~ 0.07 μm for the specimen only processed by ECAP.

Each EBSD pattern is analyzed and the solution is found when at least 4 diffraction lines are used for its determination. When the number of determined lines is lower the solution is not found and non-indexed data point is assigned. In the case that the number of non-indexing points is low, the data can be repaired by clean-up procedure. This procedure ensures that data points with the probability > 0.95 of correct indexing are retained in the analysis. The points where the probability of correct indexing is lower (points with low pattern quality) are re-assigned to neighbouring regions of similar orientation. The procedure assumes that low pattern quality points are associated with grain boundaries or regions of high dislocation density. It is known that EBSD lines are not always ideal and for this reason, the standard angle difference of 2.5° between acquired lines and lines of the solution is adjusted.

The quality map of EBSD patterns with the demonstration of an EBSD pattern is in Fig. 3. The light points denote high quality and the black points denote non-indexable EBSD patterns. The inspection of Fig. 3 shows that quality of EBSD patterns was high. The number of indexable EBSD patterns was approximately 97–98% in the annealed specimens and 79% in the specimens only processed by ECAP.

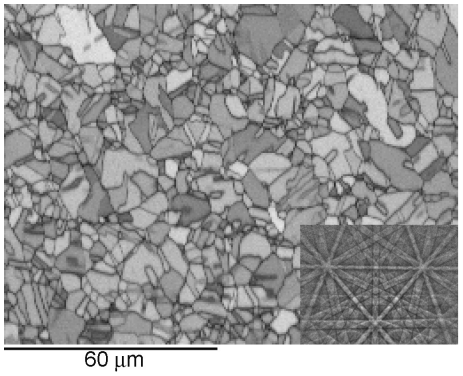

Fig. 3. *EBSD pattern quality map of Cu annealed at 573 K for 10 h with the corresponding EBSD pattern. Window size 128 × 96 μm, grid step 0.5 μm.*

IMAGE PROCESSING

The main information measured by EBSD are Euler angles $\varphi_1, \Phi, \varphi_2$ representing the crystal orientation in each grid point (Fig. 4). These three parameters are sufficient to describe the mutual position of a reference coordinate system and orientation of the crystal lattice.

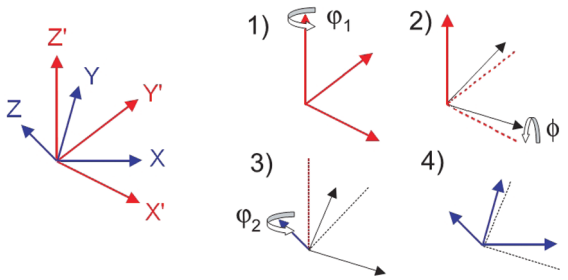

Fig. 4. *Definition of the Euler angles* $\varphi_1, \Phi, \varphi_2$. *The crystal coordinate system (red) can be superimposed onto the sample system (blue) by three rotations: 1) rotation by* φ_1 *around the Z axis of the crystal coordinate system, 2) rotation by* Φ *around the new X axis and 3) rotation by* φ_2 *around the new Z axis. The dotted lines show the positions of the axes before the last rotation.*

Fig. 5a describes the definition of a crystal direction $[uvw]$. Further, it is common to denote $\langle uvw \rangle$ all crystalographically-related directions, *i.e.*, the directions coincident with $[uvw]$ with respect to all symmetries of the crystal lattice. Supposing the difference in orientations between two neighbouring points which is called their *misorientation*, it is common to use an angle-axis representation $\theta\langle uvw \rangle$ based on the fact that one orientation can be matched to another using rotation by an angle θ around an axis $\langle uvw \rangle$. Because of non-uniqueness of this transformation especially in highly symmetric systems, only the solution with the minimum angle θ is considered and such a transformation $\theta\langle uvw \rangle$ is called *disorientation*. Results presented in this paper come from a research of metals with cubic crystal systems where the upper limit for the angle θ is about 62.8°. Details of conversion among Euler angles, transformation matrices and angle-axis representation can be found in (Engler and Randle, 2010).

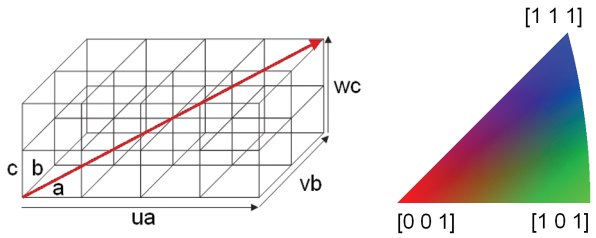

(a) (b)

Fig. 5. *(a) Meaning of a crystal direction* $[uvw]$ *in a crystal lattice with length parameters* a, b, c *of a unit cell. The direction shown here is* [422]. *(b) Inverse pole figure as a colour scheme for orientation imaging.*

Data obtained from EBSD can be immediately displayed in a pixel image where each pixel corresponds to one grid point and its colour is related to the crystal orientation (Fig. 9 in the section Numerical results). To represent each orientation by a single colour, an inverse pole figure shown in Fig. 5b is used as a colour scheme. Every orientation is located there according to the direction of one chosen axis of a reference coordinate system with respect to the crystal coordinate system in the given point. For instance, pure blue (vertex [111]) reveals that the chosen reference axis is parallel to the body diagonal of a unit cubic crystal cell. Because of invariance under rotations around the reference axis, this representation is not sufficient but still very illustrative for recognizing differences in orientations. Grain boundaries with the disorientation angle exceeding a limit value Δ, which is equal to 15° in Fig. 9, are coloured white. Another possibility often used is colouring the grains with random colours in order to distinguish them easily (Fig. 7).

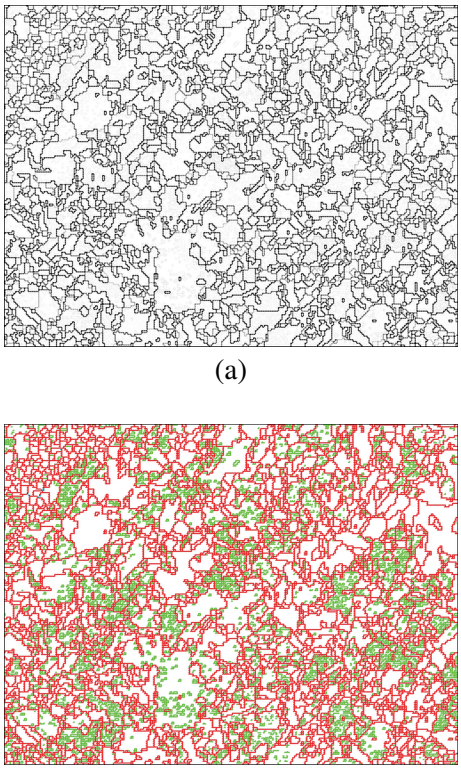

(a) (b)

Fig. 6. *Grain and subgrain boundaries in a sample of copper after 8 ECAP passes annealed for 10 hours at 373 K, section XZ, window size 128×96 µm, grid step 0.5 µm. (a) Darkness of a boundary corresponds to its disorientation angle* θ. *Pure white for* $\theta \leq 5°$ *changes linearly to pure black for* $\theta = 62.8°$. *(b) Boundaries are divided into two types – green low angle boundaries* ($\theta \leq 15°$) *and red high angle boundaries* ($\theta > 15°$).

When focusing just on the grain boundaries, we can draw them dependently on the disorientation angle θ. In Fig. 6a the darkness of each boundary is related to the disorientation angle; pure black colour corresponds to the maximum angle 62.8°. In Fig. 6b two types of boundaries are distinguished – green low angle boundaries with $\theta \leq 15°$ and red high angle boundaries with $\theta > 15°$. In a similar way it is also possible to visualize some special boundaries according to their coincidence site lattice (CSL) type.

QUANTITATIVE ANALYSIS OF GRAIN BOUNDARIES

To specify a grain boundary, five parameters are needed in general. Three of them are related to its misorientation (*e.g.*, Euler angles) and the other two describe the orientation of the interface plane (*e.g.*, spherical angles of the plane normal). However, characterizing the whole five-parameter distribution requires a large population of observable grain boundaries. In that case it is possible to use statistical methods developed for estimating the distribution density. For better insight, only changes in several parameters fixing the other ones are actually investigated which usually leads to some discretization of the parametrical space. In what follows, we will focus just on the misorientations of grain boundaries, especially the disorientation angle. This quantity represents a real-valued mark of the grain boundary network which allows to characterize it by the means of random marked closed sets (RMCS). In the following, the terminology and notation from (Ballani *et al.*, 2012) are used.

We consider a *random marked closed set* (Y,Z) in the d-dimensional Euclidean space $\mathbb{R}^d$ as a random function Z defined on a random domain $Y \subset \mathbb{R}^d$. RMCS is *stationary* if its distribution is invariant under translations and it is *isotropic* if its distribution is invariant under rotations.

For any $\varepsilon \geq 0$ define the random field

$$Z_\varepsilon(x) = \begin{cases} \max\limits_{y \in Y \cap B_\varepsilon(x)} Z(y) & \text{for } x \in Y_{\oplus\varepsilon}\,, \\ 0 & \text{otherwise,} \end{cases}$$

where $B_\varepsilon(x)$ denotes the Euclidean ball in $\mathbb{R}^d$ with centre x and radius ε, $Y_{\oplus\varepsilon}$ is a dilated set $Y_{\oplus\varepsilon} = Y \oplus B_\varepsilon(o)$.

Second-order characteristics of RMCS (Y,Z) for $x,y \in \mathbb{R}^d$ are defined as follows. Let us define

$$\kappa_f(x,y) = \lim_{\varepsilon \downarrow 0} \mathbb{E}[f(Z_\varepsilon(x), Z_\varepsilon(y)) \,|\, x,y \in Y_{\oplus\varepsilon}], \qquad (1)$$

whenever $\kappa_{|f|}(x,y) < \infty$ and $\mathbb{P}(x,y \in Y_{\oplus\varepsilon}) > 0$ for all $\varepsilon > 0$, otherwise $\kappa_f(x,y)$ is undefined. Eq. 1 is a limit of conditional expectation given the two points x,y lie in the dilated set. Common choices of f are

$$e(m,n) = m\,, \quad c(m,n) = mn\,,$$
$$v(m,n) = m^2, \quad g(m,n) = (m-n)^2.$$

Then define the conditional mean mark and the mark covariance function

$$E_\kappa(x,y) = \kappa_e(x,y)\,, \qquad (2)$$
$$\mathrm{cov}_\kappa(x,y) = \kappa_c(x,y) - \kappa_e(x,y)\kappa_e(y,x)\,. \qquad (3)$$

Further express the mark correlation function

$$\mathrm{cor}_\kappa(x,y) = \frac{\kappa_c(x,y) - \kappa_e(x,y)\kappa_e(y,x)}{\sqrt{(\kappa_v(x,y) - \kappa_e(x,y)^2)(\kappa_v(y,x) - \kappa_e(y,x)^2)}} \qquad (4)$$

and the mark variogram

$$\gamma_\kappa(x,y) = \frac{\kappa_g(x,y)}{2} = \frac{\kappa_v(x,y) + \kappa_v(y,x)}{2} - \kappa_c(x,y)\,. \qquad (5)$$

Another characteristic is the Stoyan's k_{mm} function (Stoyan *et al.*, 1995)

$$k_{mm}(x,y) = \bar{m}^{-2}\kappa_c(x,y)\,, \quad \bar{m} = \mathbb{E}[Z(x) \,|\, x \in Y]\,.$$

Under the assumptions of stationarity and isotropy of the RMCS (Y,Z), the characteristics defined in Eq. 1 are functions of the distance $r = ||x-y||$ only. For their estimation on a bounded window $W \subset \mathbb{R}^d$, choose a finite set of test points $T \subset W$ such that for a fixed $\varepsilon > 0$ and for suitable interpoint distances $r \in \mathbb{R}^+$, the sets

$$N^{(1)}_{\varepsilon,T}(r) = \{x \in Y_{\oplus\varepsilon} \cap T : \exists\, y \in Y_{\oplus\varepsilon} \cap T : ||x-y|| = r\}$$
$$N^{(2)}_{\varepsilon,T}(r) = \{(x,y) \in (Y_{\oplus\varepsilon} \cap T)^2 : ||x-y|| = r\}$$

are nonempty. For κ_e, κ_v and κ_c we use the following statistical estimators:

$$\widehat{\kappa_e}(r) = \frac{1}{|N^{(1)}_{\varepsilon,T}(r)|} \sum_{x \in N^{(1)}_{\varepsilon,T}(r)} Z(x) \qquad (6)$$

$$\widehat{\kappa_v}(r) = \frac{1}{|N^{(1)}_{\varepsilon,T}(r)|} \sum_{x \in N^{(1)}_{\varepsilon,T}(r)} Z(x)^2 \qquad (7)$$

$$\widehat{\kappa_c}(r) = \frac{1}{|N^{(2)}_{\varepsilon,T}(r)|} \sum_{(x,y) \in N^{(2)}_{\varepsilon,T}(r)} Z(x)\,Z(y) \qquad (8)$$

$$\widehat{\kappa_g}(r) = \frac{1}{|N^{(2)}_{\varepsilon,T}(r)|} \sum_{(x,y) \in N^{(2)}_{\varepsilon,T}(r)} (Z(x) - Z(y))^2 \qquad (9)$$

where $|\cdot|$ stands for cardinality of the set. Under some additional assumptions, these estimators are asymptotically unbiased when $\varepsilon \downarrow 0$.

Taking into account the grain boundary structure with almost constant marks along its edges, it is reasonable to consider whether a given pair of points lies on the same edge or not. An important feature of the estimators introduced above is that marks in a small distance are highly correlated simply because of the fact that the pair of points often belongs to the same edge. However, correlations just among different edges can give us more valuable information about the second-order structure. In what follows, we denote by $x \sim y$ the relation that the points x and y belong to ε-neighbourhood of one edge and by $x \not\sim y$ the opposite case. Under stationarity and isotropy we define

$$\tilde{N}^{(1)}_{\varepsilon,T}(r) = \{x \in N^{(1)}_{\varepsilon,T}(r) : \exists y \in N^{(1)}_{\varepsilon,T}(r) : x \not\sim y\}$$
$$\tilde{N}^{(2)}_{\varepsilon,T}(r) = \{(x,y) \in N^{(2)}_{\varepsilon,T}(r) : x \not\sim y\}$$

and $\widehat{\tilde{\kappa}}_e(r), \widehat{\tilde{\kappa}}_v(r), \widehat{\tilde{\kappa}}_c(r), \widehat{\tilde{\kappa}}_g(r)$ can be defined in a similar way like Eqs. 6-9, using non edge-related sets $\tilde{N}^{(1)}_{\varepsilon,T}(r), \tilde{N}^{(2)}_{\varepsilon,T}(r)$ instead of $N^{(1)}_{\varepsilon,T}(r), N^{(2)}_{\varepsilon,T}(r)$. Benefit of these estimators is that they suppress the effect of high correlation of pairs of points belonging to the same edge.

Another approach to characterizing the grain boundary structure as a marked fibre process consists in investigating several types of special boundaries dominantly influencing properties of the material. Let us suppose that each point of the grain boundary network is given a categorical mark $Z(x) \in \mathscr{Z} = \{1,2,\ldots,m\}$ which is constant for points belonging to the same edge. For each pair of values $i, j \in \mathscr{Z}$, we define the cross K-function

$$K_{i,j}(r) = \frac{1}{\lambda_i \lambda_j \delta(A)} \mathbb{E}\,[\int_Y \int_{Y \cap A} 1_{[||x-y|| \le r]}\, \mathrm{d}x\, \mathrm{d}y \,| \, Z(x) = i, Z(y) = j]\,, \quad (10)$$

where λ_i is an intensity function of a fibre subprocess of edges with the mark $i \in \mathscr{Z}$ and $A \in \mathscr{B}_0$ is an arbitrary bounded Borel set with positive Lebesgue measure $\delta(A) > 0$. To estimate Eq. 10 it is necessary to provide a segmentation of pixellated grain boundaries (Arnould *et al.*, 2001; Jeulin and Moreaud, 2008). During this smoothing procedure, the grain boundaries are identified as lines or curves separating different phases in the image. On the segmented fibre structure Y_s we firstly define a simple intensity estimator of λ_i

$$\widehat{\lambda_i} = \frac{1}{\delta(W)} \int_{Y_s} 1_{[Z(y)=i]}\, \mathrm{d}y\,.$$

Based on the set of test points $V_i \subset \{y \in Y_s : Z(y) = i\}$, an estimator of Eq. 10 can be expressed as

$$\widehat{K_{i,j}}(r) = \frac{\sum_{x \in V_{i,\ominus r}} (\int_{Y_s} 1_{[||x-y|| \le r, Z(y)=j]}\, \mathrm{d}y)}{\hat{\lambda}_i \hat{\lambda}_j \delta(W_{\ominus r}) |V_{i,\ominus r}|}\,,$$

where $W_{\ominus r} = W \ominus B_r(o)$ is eroded window providing the edge effects correction and $V_{i,\ominus r} = V_i \cap W_{\ominus r}$.

The K-function can be useful for interpretation of clustering of different types of grain boundaries. For instance, higher values of $K_{i,j}(r)$ indicate clustering of edges with the mark j around edges with the mark i.

NUMERICAL RESULTS

The methods were applied to data obtained from EBSD of copper processed by equal-channel angular

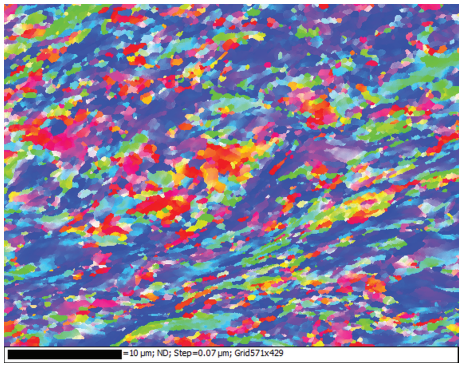

Fig. 7. *Crystal orientation map of Cu after 8 ECAP passes with randomly coloured grains. Window size 40 × 30 µm, grid step 0.07 µm.*

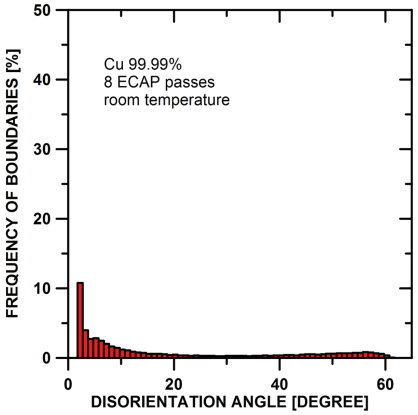

Fig. 8. *Histogram of disorientation angles of Cu after 8 ECAP passes.*

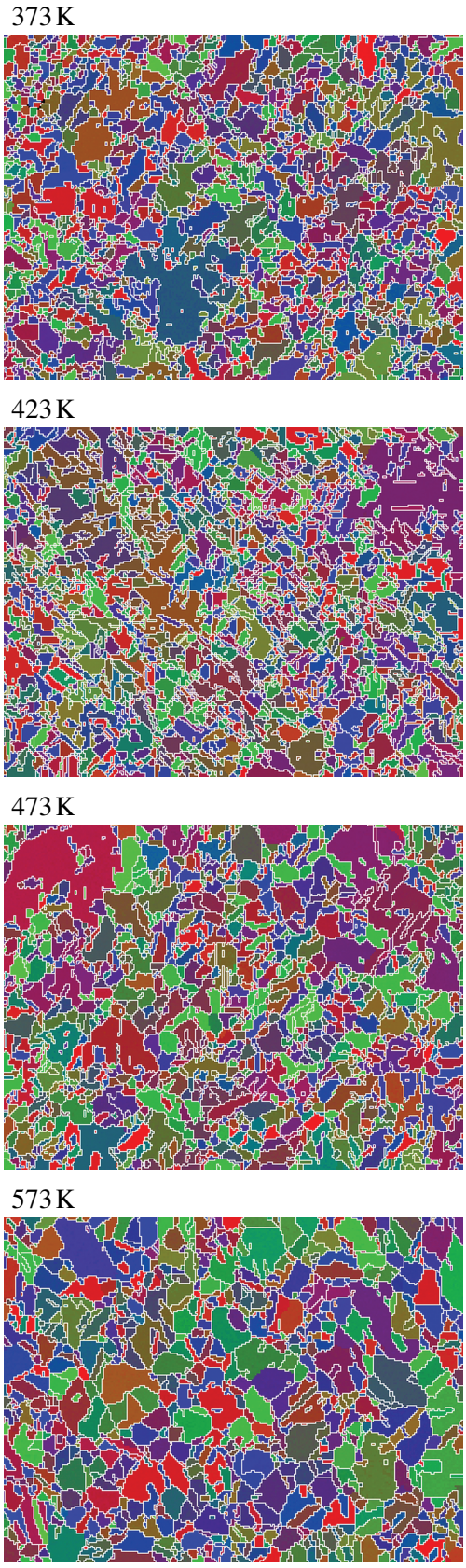

Fig. 9. *Crystal orientation maps of Cu after 8 ECAP passes annealed for 10 hours at 373 K, 423 K, 473 K or 573 K. Window size 128 × 96 µm, grid step 0.5 µm.*

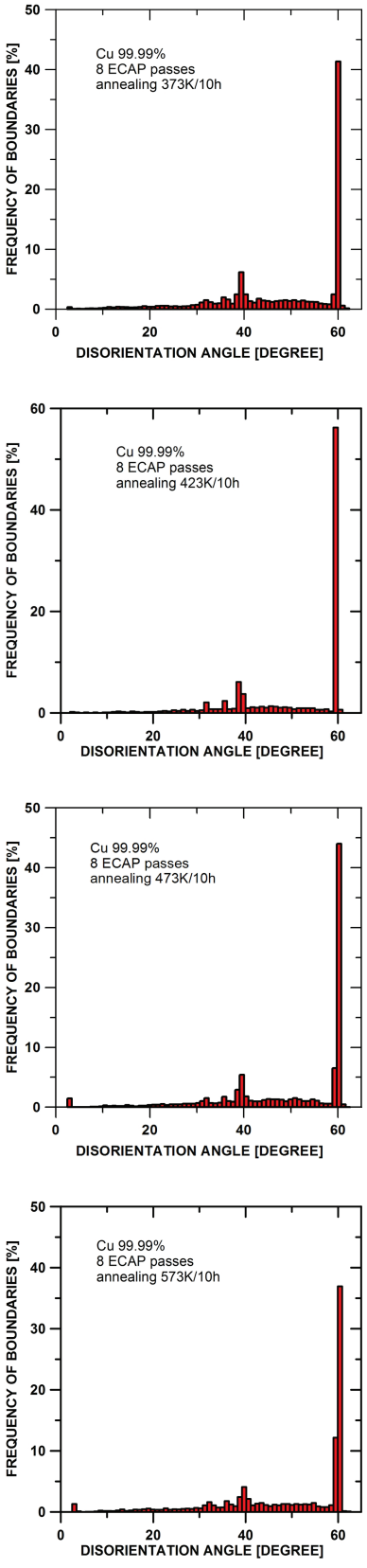

Fig. 10. *Histograms of disorientation angles of four examined samples from Fig. 9.*

pressing. After 8 passes through the die, the samples were annealed for 10 hours at different temperatures – 373 K, 423 K, 473 K and 573 K (Fig. 9). It is obvious that the temperature of annealing influences the microstructure.

To indicate changes in the average grain size, Table 1 summarizes the mean areas of grain profiles and their variation coefficients, *i.e.*, ratio of the standard deviation and the mean area, in observed cross section.

Table 1. *Mean profile areas in* μm^2 *and their variation coefficients in the sample without annealing and four annealed samples.*

no annealing	373 K	423 K	473 K	573 K
0.97	4.90	3.21	7.01	10.57
0.01	0.20	0.26	0.29	0.12

Increasing tendency in average grain size also influences the lengths of the edges of the grain boundaries observed in the cross sections. Fig. 11 shows that the majority of them lies below 2 µm (edges shorter than 0.5 µm were excluded during the segmentation) but especially in the last sample even several times longer edges are present.

Histograms of disorientation angles in Fig. 10 indicate among others a high fraction of $\Sigma 3$ boundaries with $\theta = 60°$, mostly being so called *twin boundaries* with axis of rotation $\langle 1,1,1 \rangle$, and $\Sigma 9$ boundaries with $\theta \doteq 39°$. However, in the microstructure of copper processed by 8 ECAP passes rather low-angle grain boundaries (LAGB's) and random high-angle grain boundaries (HAGB's) predominated. From Table 2 it is apparent that frequency of random HAGB's remains about 40-50% while frequency of twin boundaries rapidly increases when the material is annealed.

Table 2. *Frequency of selected boundaries in microstructure of pure copper processed by ECAP and subsequent annealing at different temperatures for 10h.*

specimen	LAGB's	$\Sigma 3$	$\Sigma 9$	HAGB's
no annealing	57.92	2.57	0.25	39.26
373 K	2.50	35.83	6.75	54.92
423 K	2.10	54.30	7.42	36.18
473 K	2.89	41.43	6.15	49.53
573 K	3.08	40.13	5.09	51.70

Observation of high frequency of twins is fully consistent with the investigation of the role of shear stress in formation of annealing twin boundaries in copper (Field *et al.*, 2006). Field et al. revealed that the twin content in rolled copper with 92% reduction is significantly lower than that in any copper deformed by ECAP, regardless of the annealing temperature. (Molodova *et al.*, 2007) found a very low thermal stability of pure copper processed by ECAP. They observed that in the microstructure of pure copper processed by 12 ECAP passes, large recrystallized grains can be already found even after annealing at 393 K for 10 min and 423 K for 2 min. In our study, the occurrence of large recrystallized grains was observed at all annealed temperatures with markedly local character.

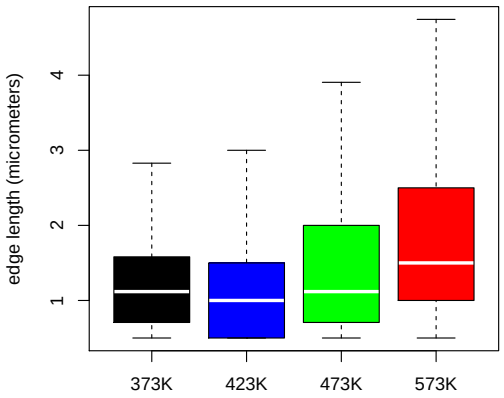

Fig. 11. *Box plots of lengths of the grain boundaries of four examined samples. The plots show median, the first and the third quartile and 1.5 multiple of the interquartile range. Outliers are not figured.*

Occurrence of high frequency of twin boundaries in the microstructure of annealed copper samples before loading in the creep testing machine can significantly influence creep behaviour. It was found (Watanabe and Tsurekawa, 1999; Watanabe, 2011) that a high fraction of strong low-Σ boundaries is a key factor controlling intergranular brittleness. The control of intergranular fracture and intergranular brittleness can be achieved by reduction of random boundaries or conversely by increasing the fraction of LAGB's or special low Σ coincidence boundaries resistant to fracture.

It is generally accepted that the damage near grain boundaries is one of the key factors controlling creep life because many cracks are initiated at grain boundaries and frequently major degradation phenomena in materials are subjected to the creep exposure. Furthermore, grain boundaries can influence creep behaviour of ultrafine-grained materials due to synergetic effect of additional operating creep mechanisms like grain boundary sliding (GBS), intergranular cavitation or more intensive grain

boundary diffusion (Král *et al.*, 2012). Nevertheless the ability of GBS takes place more significantly at a random grain boundary compared with low-Σ boundaries (Kokawa *et al.*, 1981; Watanabe *et al.*, 1984).

With the characteristics introduced in the previous section, we aim at characterizing the microstructure in a more complex view. The following results show that even though the marginal distribution of disorientation angles and the fraction of special boundaries can be similar, their arrangement in the grain boundary network can differ crucially. The second-order characteristics describe these aspects on the basis of correlations and clustering of different grain boundary types measured in a small distance radius. The quantities defined in Eq. 1 are estimated using a set of test points T given by all the grid points of the EBSD measurement and a fixed $\varepsilon > 0$ given by the grid step. The cross K-function Eq. 10 is estimated using a set of test points V_i given by midpoints of the i-th type boundaries, $i \in \mathscr{X} = \{3, 9, L, H\}$, where the marks correspond to Σ3, Σ9, LAGB's and random HAGB's.

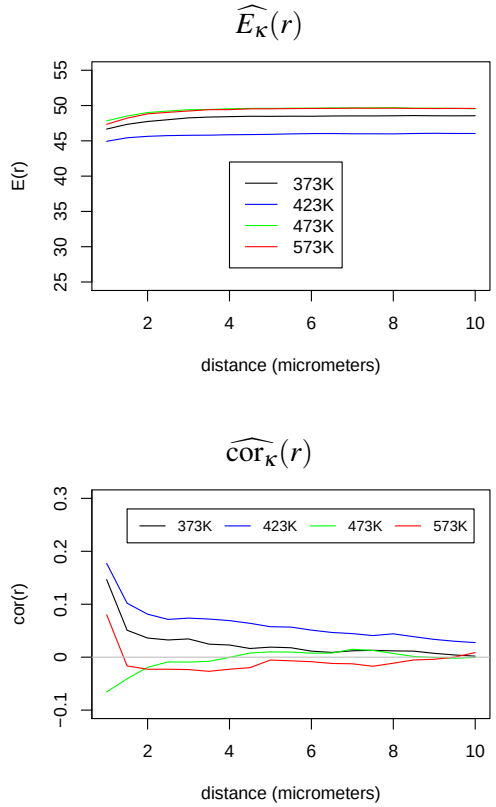

Fig. 12. *Estimators of the mark expectation* $\widehat{E_\kappa}(r) = \widehat{\kappa}_e(r)$ *and the mark correlation function* $\widehat{\mathrm{cor}_\kappa}(r) = \widehat{\kappa}_c(r) - \widehat{\kappa}_e(r)^2$ *of four examined samples.*

Fig. 12 shows the estimators of the mark expectation $\widehat{E_\kappa}(r) = \widehat{\kappa}_e(r)$ and the mark correlation function $\widehat{\mathrm{cor}_\kappa}(r) = \widehat{\kappa}_c(r) - \widehat{\kappa}_e(r)^2$ of four examined samples. The first estimator is almost constant because for every step distance r plotted there, the set $\tilde{N}^{(1)}_{\varepsilon,T}(r)$ contains almost every point $x \in Y_{\oplus\varepsilon} \cap T$ and in this case the estimator equals to the unconditional mean mark with respect to T. With increasing annealing temperature, we can observe increasing trend of the mark expectation and decreasing trend of the mark correlation function. In other words, increase in the annealing temperature leads to more random arrangements of edges within the distance r in the sense of their disorientation angles.

In the next we aim at localization of the dominant Σ3 boundaries near the other boundary types. Fig. 13 shows the estimators of the cross K-functions $\widehat{K_{3,3}}(r)$, $\widehat{K_{9,3}}(r)$, $\widehat{K_{L,3}}(r)$ and $\widehat{K_{H,3}}(r)$, which help to interpret the occurrence of Σ3 boundaries in neighbourhoods of Σ3, Σ9, LAGB's or random HAGB's. While Table 2 shows the marginal proportions of different boundary types, these K-functions bring an additional information about their mutual positions in the structure. We see that in the samples with higher annealing temperature, values $\widehat{K_{3,3}}(r)$ and $\widehat{K_{9,3}}(r)$ are generally lower which indicates higher regularity of Σ3 boundaries with respect to themselves or Σ9 boundaries. On the other hand, the situation is different in the neighbourhood of less dominant boundary types where these functions are minimal for the low-temperature annealed 423 K sample but any clearly interpretable trend is missing here.

It was found (Molodova *et al.*, 2007; Saxl *et al.*, 2010) that application of ECAP method could lead to the formation of the bimodal or even multimodal microstructures. The bimodality can depend on an appropriate thermal or creep loading conditions. It is widely accepted that the co-existence of larger recrystallized grains in the bimodal structure can improve deformation behaviour and thereby a ductility of ultrafine-grained material by relaxation of the stress concentration, created by GBS, through plastic deformation inside of larger grains (Ma, 2003; Koch, 2003; Fan *et al.*, 2006). By contrast, a very recent report on creep ductility of ultrafine-grained materials did not confirm general acceptance of this view (Sklenička *et al.*, 2012).

CONCLUSIONS

The present paper defines the grain boundary structure as a random marked closed set which

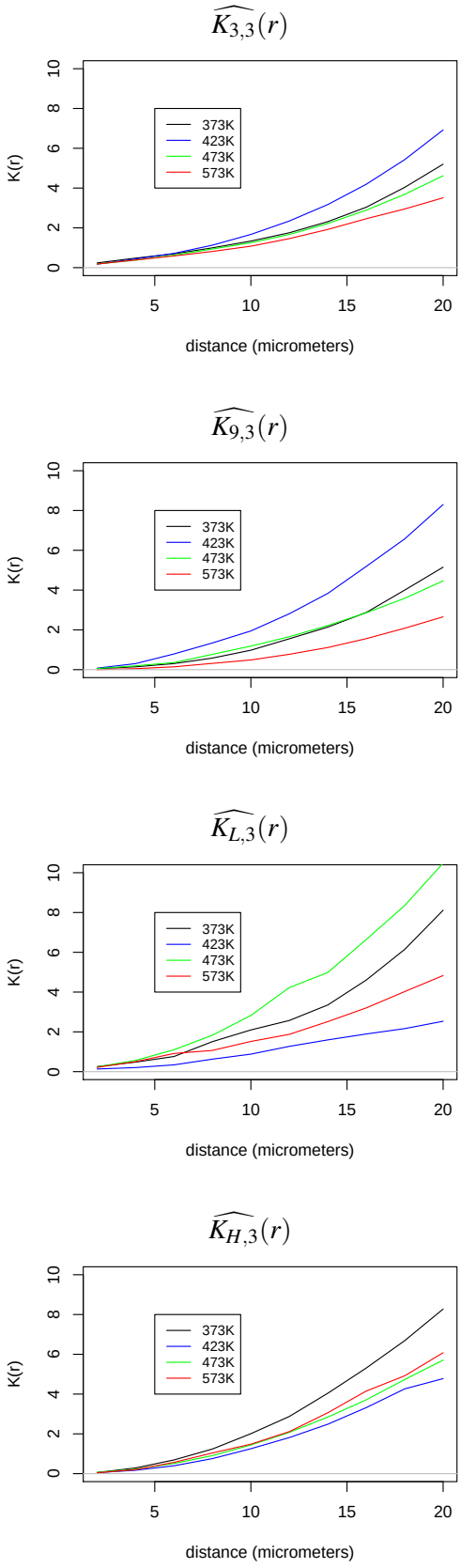

Fig. 13. *Estimators of the cross K-functions* $\widehat{K_{3,3}}(r)$, $\widehat{K_{9,3}}(r)$, $\widehat{K_{L,3}}(r)$ *and* $\widehat{K_{H,3}}(r)$ *of four examined samples where the indexes* $3,9,L,H$ *represent* $\Sigma 3$, $\Sigma 9$, *LAGB's and random HAGB's.*

is observable in a planar section with the use of orientation imaging microscopy. To characterize its spatial distribution, it is useful to extend the common attitude based on marginal distributions to the second-order analysis. Methods of estimation of the second-order characteristics are provided and their use on particular specimens of metallic material is shown. To reveal the dependency between disorientations as a function of distance in a stationary and isotropic structure, appropriate estimators of second-order characteristics of the marks are defined which suppress the effect of high correlation of the marks along particular edges.

The methods are demonstrated on grain boundary structures marked by the disorientation angle or equipped with categorical marks indicating specialness of boundaries according to their CSL type. The subsequent annealing of the microstructure of pure copper processed by 8 ECAP passes led to the formation of the bimodal microstructure containing high fraction of low-Σ coincidence boundaries. The second-order characteristics provide an additional information about arrangements of different boundary types in the structure. Our results show that increasing temperature of annealing leads to decreasing tendency of $\Sigma 3$ boundaries to form clusters but more likely to be placed regularly or create longer paths in the microstructure.

ACKNOWLEDGEMENT

The research was supported by the Czech Science Foundation, project P201/10/0472, and Operational Program Research and Development for Innovations co-funded by the European Regional Development Fund (ERDF) and national budget of the Czech Republic, within the framework of project Centre of Polymer Systems (reg. number: CZ.1.05/2.1.00/03.0111). Special thanks belong to Jiří Dvořák for preparation of the samples and operation with the ECAP facilities. The topic of this paper was presented at the S4G Conference, June 25-28, 2012 in Prague, Czech Republic.

REFERENCES

Arnould X, Coster M, Chermant J-L, Chermant L, Chartier T, Elmoataz A (2001). Segmentation and grain size of ceramics. Image Anal Stereol 20:131–5.

Ballani F, Kabluchko Z, Schlather M (2012). Random marked sets. Adv Appl Probab 44(3):603–16.

Bastos A, Zaefferer S, Raabe D, Schuh C (2006). Characterization of the microstructure and texture of nanostructured electrodeposited NiCo using electron backscatter diffraction (EBSD). Acta Mater 54:2451–62.

Britton TB, Wilkinson AJ (2012). Stress fields and geometrically necessary dislocation density distributions near the head of a blocked slip band. Acta Mater 60:5773–82.

Calcagnotto M, Ponge D, Demir E, Raabe D (2010). Orientation gradients and geometrically necessary dislocations in ultrafine grained dual-phase steels studied by 2D and 3D EBSD. Mater Sci Eng A 527:2738–46.

Dvořák J, Sklenička V, Král P, Svoboda M, Saxl I (2010). Characterization of creep behaviour and microstructure changes in pure copper processed by equal-channel angular pressing. Part I. Creep behaviour. Rev Adv Mater Sci 25:225–32.

Engler O, Randle V (2010). Introduction to texture analysis – macrotexture, microtexture and orientation mapping. 2nd Ed. CRC Press.

Fan GJ, Choo H, Liaw PK, Lavernia EJ (2006). Plastic deformation and fracture of ultrafine-grained Al-Mg alloys with a bimodal grain size distribution. Acta Mater 54:1759–66.

Field DP, Eames RC, Lillo TM (2006). The role of shear stress in the formation of annealing twin boundaries in copper. Scripta Mater 54:983–6.

Furukawa M, Iwahashi I, Horita Z, Nemoto M, Langdon TG (1998). The shearing characteristics associated with equal-channel angular pressing. Mater Sci Eng A 257: 328–32. .

Humphreys FJ (2001). Grain and subgrain characterisation by electron backscatter diffraction. J Mater Sci 36:3833–54.

Ilucová L, Saxl I, Svoboda M, Sklenička V, Král P (2007). Structure of ECAP aluminium after different number of passes. Image Anal Stereol 26:37–43.

Jeulin D, Moreaud M (2008). Segmentation of 2D and 3D textures from estimates of the local orientation. Image Anal Stereol 27:183–92.

Jiang J, Godfrey A, Liu W, Liu Q (2008). Microtexture evolution via deformation twinning and slip during compression of magnesium alloy AZ31. Mater Sci Eng A 483–4:576–9.

Koch CC (2003). Optimization of strength and ductility in nanocrystalline and ultrafine grained metals. Scripta Mater 49:657–62.

Kokawa H, Watanabe T, Karashima S (1981). Sliding behaviour and dislocation structures in aluminium grain boundaries. Philos Mag A 44:1239–54.

Král P, Dvořák J, Kvapilová M, Svoboda M, Beneš V, Ponížil P, Šedivý O, Sklenička V (2011). Quantitative characterization of microstructure in copper processed by equal-channel angular pressing. Mat Sci Forum 667–9:235–40.

Král P, Svoboda M, Dvořák J, Kvapilová M, Sklenička V (2012). Microstructure mechanisms governing the creep life of ultrafine-grained Cu-0.2wt.% Zr alloy. Acta Phys Pol A 122:457–60.

Ma E (2003). Instabilities and ductility of nanocrystalline and ultrafine-grained metals. Scripta Mater 49:663–8.

Molodova X, Gottstein G, Winning M, Hellmig RJ (2007). Thermal stability of ECAP processed pure copper. Mater Sci Eng A 460–1:204–13.

Perez M, Kenik E, Keefe OM, Miller F, Johnson B (2006). Identification of phases in zinc alloy powders using electron backscatter diffraction. Mater Sci Eng A 424:239–50.

Randle V, Rohrer G, Miller H, Coleman M, Owen G (2008). Five-parameter grain boundary distribution of commercially grain boundary engineered nickel and copper. Acta Mater 56:2363–73.

Randle V (2009). Electron backscatter diffraction: strategies for reliable data acquisition and processing. Mater Charact 60:913–22.

Rohrer GS (2011). Measuring and interpreting the structure of grain-boundary networks. J Am Ceram Soc 94(3):633–46.

Saxl I, Sklenička V, Ilucová L, Svoboda M, Král P, Dvořák J (2010). Characterization of creep behaviour and microstructure changes in pure copper processed by equal-channel angular pressing. Part II. The microstructural characteristics. Rev Adv Mater Sci 25: 233–40.

Sklenička V, Dvořák J, Král P, Svoboda M, Kvapilová M, Langdon TG (2012). Factors influencing creep flow and ductility in ultrafine-grained metals. Mat Sci Eng A 558:403–11.

Stoyan D, Kendall WS, Mecke J (1995). Stochastic geometry and its applications. 2nd Ed. New York: Wiley.

Watanabe T (2011). Grain boundary engineering: historical perspective and future prospects. J Mater Sci 46:4095–115.

Watanabe T, Kimura S-I, Karashima S (1984). The effect of a grain boundary structural transformation on sliding in $\langle 1010 \rangle$-tilt zinc bicrystals. Philos Mag A 49:845–64.

Watanabe T, Tsurekawa S (1999). The control of brittleness and development of desirable mechanical properties in polycrystalline systems by grain boundary engineering. Acta Mater 47:4171–85.

Wilkinson AJ, Britton TB (2012). Strains, planes, and EBSD in materials science. Mater Today 15:366–76.

Image Anal Stereol 2013;32:77-87 doi:10.5566/ias.v32.p77-87
Original Research Paper

CHARACTERIZATION OF THE FORMATION OF FILTER PAPER USING THE BARTLETT SPECTRUM OF THE FIBER STRUCTURE

MARTIN LEHMANN[1], JOBST EISENGRÄBER-PABST[1], JOACHIM OHSER✉,[2] AND ALI MOGHISEH[2]

[1]Mann+Hummel GmbH, Hindenburgstr. 45, D-71638 Ludwigsburg, Germany; [2]Univ. Appl. Sci. Darmstadt, Dept. Math & Nat. Sci., Schöfferstr. 3, D-64295 Darmstadt, Germany
e-mail: martin.lehmann@mann-hummel.com, jobst.eisengraeber-pabst@mann-hummel.com, jo@h-da.de, ali.moghiseh@h-da.de
(Received December 20, 2012; revised May 22, 2013; accepted June 10, 2013)

ABSTRACT

The formation index of filter paper is one of the most important characteristics used in industrial quality control. Its estimation is often based on subjective comparison chart rating or, more objective, on the power spectrum of the paper structure observed on a transmission light table. It is shown that paper formation can be modeled by means of Gaussian random fields with a well-defined class of correlation functions, and a formation index which is derived from the density of the Bartlett spectrum estimated from image data: the mean of the Bessel transform of the correlation function taken for wave lengths between 2 and 5 mm. Furthermore, it is shown that a considerable variation of the local grammage can be observed also in cases where the the fibers are uniformly and independently scattered in the paper sheet.

Keywords: Bartlett spectrum, chart cloudiness, fiber system, filter paper, formation, image analysis.

INTRODUCTION

Filter papers are used in a wide variety of fields, ranging from air to oil filters (Durst *et al.*, 2007). They consist of fibers, which are more or less randomly distributed. Except the specific paper weight (*i.e.*, the weight per unit area, also called the nominal grammage), the weight *distribution* is a very important characteristic of paper. It influences many properties of filter papers such as flow rate, particle collection, efficiency, wet strength, porosity and dust holding capability. Thus, characterization of the weight distribution is important for industrial quality control as well as for the development of new filter materials and technologies of manufacture.

It is easy to get an impression of the weight distribution when holding a sheet of paper up against light and observing the distribution of the optical density, known as the paper formation, chart cloudiness or flocculation. Assuming a constant absorption coefficient for the solid constituents of the paper structure, the local intensity of the transmitted light can be related to the local weight density by Lambert-Beer's law. As a consequence, there is a close relationship between weight distribution and formation and, in fact, often one does not distinguish between both. See Van den Akker (1949), McDonald *et al.* (1986) and Lien and Liu (2006) for the computation of the grammage from the absorption of visible light. The use of soft X-radiation is suggested in Farrington (1988), and the influence of the choice of radiation on transmittance is investigated for nonwoven fabrics in Boeckerman (1992) and for paper in Norman and Wahren (1976) and Bergeron *et al.* (1988).

Usually, the formation is experimentally determined based on two-dimensional (2D) images of the paper structure. A transmission light table is used in order to ensure a homogeneous illumination and the images are acquired by a CCD-camera having a linear transfer function, such that the pixel values can be assumed to be approximately proportional to the corresponding local intensities. In the simplest case, a paper structure inspection can be based on subjective comparison chart rating, supported by an industrial standard consisting on well-formulated rules for image acquisition and rating. Nevertheless, the valid industrial norm on paper, board, pulps and related terms gives only a rough description of the terms 'formation' (manner in which the fibers are distributed, disposed and intermixed to constitute the paper) and 'lock-through' (structural appearance of a sheet of paper observed in diffuse transmitted light), ISO 4046(E/F), 2012. Inspection systems based on image analysis include computation of a (more or less objective) value for a 'formation index' (or a 'formation number') from the image data. One should keep in mind that such a formation index estimated from image data is (widely) independent of the nominal grammage as well as on the variance of the

local paper weight. But what is exactly meant by the 'formation index', and is it sufficient to characterize paper formation by only one number?

There is a huge number of publications on the characterization of paper formation (Kallmes, 1984; Cresson, 1988; Cherkassky, 1999; Drouin *et al.*, 2001), see also Waterhouse *et al.* (1991) and Praast and Göttsching (1991) for a very good survey on literature from the late 1980th and Chinga-Carrasco (2009) for newer developments. An intuitive characteristic for the formation is the mean paper flock size, going back to Robertson (1956), but until now there is no convincing method for segmenting flocks in gray-tone images. More useful methods are based on measuring the variance of the pixel values or, more general, the co-occurrence matrix of the image data (Yuhara *et al.*, 1986; Cresson, 1988; Cresson and Luner, 1990a;b). The approach presented in Pourdeyhimi and Kohel (2002) is motivated by a Poisson statistics for the centers of paper flocks (objects). On the one hand, these centers cannot safely be detected and, on the other hand, the computation of the 'uniformity intex' of the paper formation is based on the variation of the area fraction in a binarized image but even not on the flock centers.

In the carefully written monograph of Deng and Dodson (1994) a formation number $n = \mathrm{var}_r/\mathrm{var}_0$ is defined as ratio of variances var_r and var_0 of integrated local grammage, where the integration is over a square of edge length 1 mm. In this approach, var_r is the variance for the real structure and var_0 is the variance for a reference model (a Boolean segment process). This approach goes back to earlier works, *e.g.* Norman and Wahren (1974) and is frequently cited also in current literature, *e.g.*, Sampson (2009). A similar approach is used in Farnood *et al.* (1995), where the fluctuation of the local grammage is modeled as a Poisson shot noise process (or a dilution model) of sperical flocks. I'Anson and Sampson (2003) discussed the relationship between Farnood's flocculation characteristic and the spectral density of paper formation.

Since woven textiles have a (more or less) periodic pattern, it seems to be obvious to apply Fourier methods for quality inspection, see *e.g.*, Wang *et al.* (2011) and references therein, where slight deviations from the periodicity are detected based on the correlation function of the pattern or, analogously, its counterpart in the inverse space – the so-called power spectrum. The use of Fourier transform for an identification of periodic patterns in paper and board traces back to I'Anson (1995). In Sara (1978), Norman (1986), Cresson (1988), Provatas *et al.* (1996), Cherkassky (1998) and Lien and Liu (2006), the correlation function and the power spectrum are also suggested as characteristics for cloudiness of (non-periodic but macroscopically homogeneous) nonwovens and paper formation, respectively (Section 2.2 in Alava and Niskanen, 2006). Sometimes the range of interaction , *i.e.*, integral of the correlation function (also known as the integral range), is used as a formation index. Instead of a Fourier transform, Scharcanski (2006) uses a wavelet transform to extract a spectral density from the sheet formation.

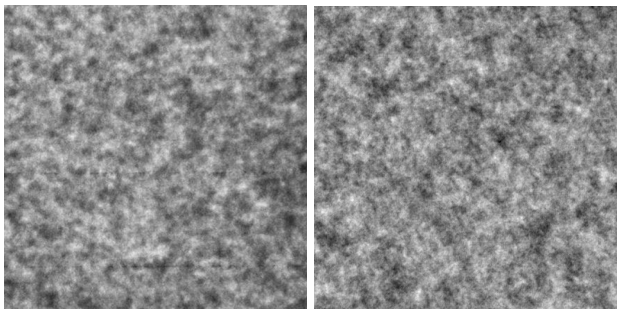

Fig. 1. *An image showing the formation of a filter paper (left) and a realization of a macroscopically homogeneous and isotropic GRF (right) with* $k(x) = \mathrm{e}^{-\lambda\|x\|}$ *and* $\lambda = 0.6\,mm^{-1}$*; the edge length of the images 102.4 mm.*

Mathematical modeling of paper structure on a mesoscale can lead to a deeper understanding, *e.g.*, of the phenomenon of formation (Cresson, 1988; Cherkassky, 1998; Antoine, 2000; Gregersen and Niskanen, 2000; Provatas *et al.*, 2000; Sampson, 2009), where the model parameters – so far they can easily be estimated from image data – serve as formation characteristics. Further approaches are based on modeling random structures by *Markow Random Fields* (MRF) and decomposing the image of the structure into "different scales", evaluating the degree of homogeneity on each scale and computing an overall degree of homogeneity. Scholz and Claus (1999) applied this approach originally on the structure of nonwovens (fleeces and felts), but in principle this works also for the evaluation of paper structures, where the degree of homogeneity can be seen as a formation index. Notice that the "different scales" mentioned above are also known as the *Laplacian pyramid* of image data (Burt and Adelson, 1983).

In the present article we use *Gaussian Random Fields* (GRFs) for modeling paper formation and, following the suggestion made in Xu (1996) and Lien and Liu (2006), a Fourier approach is applied for computing characteristics of paper formation. More precisely, we show that the formation of the investigated filter papers can be characterized by the density of the Bartlett spectrum, *i.e.*, a spectral representation of the correlation function,

which can be estimated by the method of Koch *et al.* (2003). Using a parametric approach for the Bartlett spectrum, we introduce one of its parameters as a characteristic for paper formation. Nevertheless, to be independent of the fitting of a theoretical function to the experimental data, the formation index is determined directly from estimates of the spectral density.

Finally, it is shown by an example that the spectral density of the paper structure can contain high fractions of long waves even if no flocculation occurs, *i.e.*, the fibers are uniformly and independently scattered in the paper sheet.

MODELING PAPER FORMATION BY GAUSSIAN RANDOM FIELDS

Visual inspection of Fig. 1 shows that the formation of filter paper is surely one of the most convincing applications for GRFs. The difference among the real structure on the left-hand side and the realization on the right-hand side, which is obtained from the adapted GRF, can be recognized only by experts. This is very important since, if formation can really be modelled by GRFs, then the Bartlett spectrum of a GRF uniquely specifies formation.

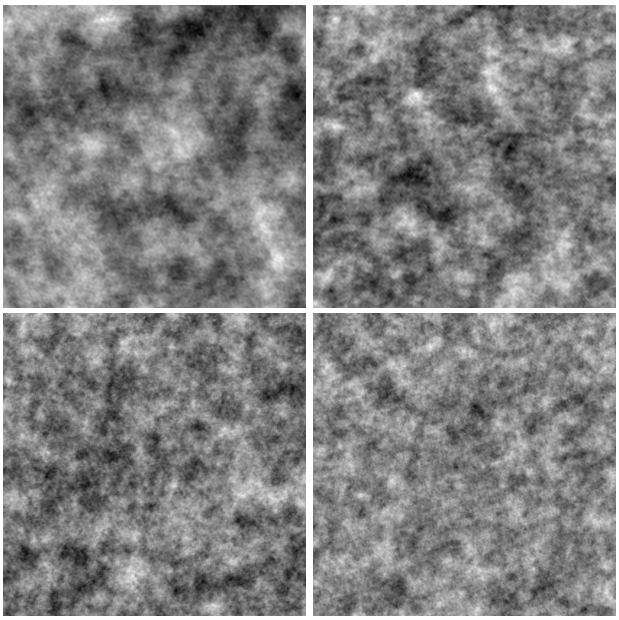

Fig. 2. *Realizations of macroscopically homogeneous and isotropic GFRs for constant* μ *and* σ^2 *and exponential correlation function* $k(x) = \mathrm{e}^{-\lambda\|x\|}$ *with parameters* $\lambda = 0.1\,mm^{-1}, \ldots, \lambda = 0.4\ mm^{-1}$, *lexicographic order. The edge length of the images is 102.4 mm.*

As it is well known, a random field $\Phi(x)$ is a 2-dimensional, real-valued random function. The function $\Phi(x)$ is called macroscopically homogeneous (or stationary in the strict sense), if $\Phi(x)$ is invariant with respect to translations, *i.e.*, its finite-dimensional distributions are translation invariant. Furthermore, $\Phi(x)$ is said to be isotropic, if it is invariant with respect to rotations around the origin. Finally, a random field $\Phi(x)$ is a *Gaussian Random Field* (GRF) if all its finite-dimensional distributions are multivariate normal distributions (see, *e.g.*, Adler, 1981; Abrahamsen, 1985 and Adler and Taylor, 2007 for introductions to GRFs).

A macroscopically homogeneous GRF $\Phi(x)$ is uniquely specified by its mean $\mu = \mathbb{E}\Phi(x)$, its variance $\sigma^2 = \mathbb{E}\Phi^2(x) - \mu^2$, and the covariance function

$$\mathrm{cov}(x) = \mathbb{E}\big((\Phi(y)-\mu)(\Phi(y+x)-\mu)\big)\,, \quad x \in \mathbb{R}^2\,,$$

which is independent of $y \in \mathbb{R}^2$ and positiv definite. The normalized function $k(x) = \mathrm{cov}(x)/\sigma^2$ is known as the (auto-) correlation function. The expectation μ is the first order characteristic of $\Phi(x)$ while σ^2 and k are second order characteristics. All higher order characteristics depend only on μ, σ and k. This is a direct consequence of the Gaussianity (Abrahamsen, 1985), which means that our attention can be payed exclusively on the first and second order characteristics and their estimation.

Four realizations of GRFs $\Phi_\lambda(x)$ with an exponential correlation function $k(x) = \mathrm{e}^{-\lambda\|x\|}$, $x \in \mathbb{R}^2$, are shown in Fig. 2. It turns out that the distributional properties of $\Phi_\lambda(x)$ distinguish by the positive scaling parameter, *i.e.*, it holds $\Phi_\lambda(x) \stackrel{d}{=} \Phi_1(\lambda x)$, and realizations of $\Phi_\lambda(x)$ can be obtained from realizations of $\Phi_1(x)$ by scaling.

If a GRF is well adapted to the image data of a paper structure, then the interpretation of its characteristics μ, σ^2 and k is as follows: The mean μ is the brightness, σ corresponds to the image dynamics, and k is the correlation function of the pixel values. Under some technical conditions (using of a CCD camera allowing photometric measurements, high gray-tone resolution, constant gain, *etc.*), assuming Lambert-Beer's law for light absorption and knowing the initial light intensity, the nominal paper grammage and the weight variance can roughly be estimated from μ and σ^2, respectively. As a consequence, the correlation function k characterizes the paper formation uniquely. Fig. 3 shows realizations of two GRFs with the same μ and k but different σ. One feels subjectively that the formation is the same in both images.

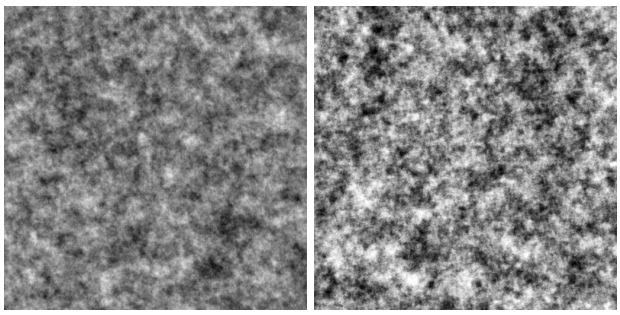

Fig. 3. *Realizations of two macroscopically homogeneous and isotropic GRFs with constant* μ *and* $k(x) = \mathrm{e}^{-\lambda\|x\|}$ *with* $\lambda = 0.5\,mm^{-1}$*; left: small* σ*, right: larg* σ*. The edge length of the images is 102.4 mm.*

Finally, we remark that in the isotropic case the correlation function k depends on only the radial coordinate $r = \|x\|$ of x, *i.e.*, there is a function k_1 such that $k(x) = k_1(\|x\|) = k_1(r)$. Clearly, the exponential correlation function mentioned above is such a function.

THE SPECTRAL REPRESENTATION OF THE CORRELATION FUNCTION

First of all, we recall Bochner's theorem which states that the covariance function $\mathrm{cov} = \sigma^2 k$ of a macroscopically homogeneous random field $\Phi(x)$ can be represented by a non-negative, bounded measure Γ_Φ – the so-called spectral measure or the Bartlett spectrum of $\Phi(x)$. A proof is given *e.g.*, in Katznelson (2004), p. 170. This important theoretical result is also useful in applications, since efficient Monte Carlo techniques of generating realizations of GRFs as well as fast algorithms for estimating their second order characteristics are based on spectral representations. In this article we restrict ourselves to the particular cases in which the Bartlett spectrum Γ_Φ has a density γ_Φ, which is also known as the spectral density of $\Phi(x)$. If $\hat{k}$ denotes the Fourier transform of k, then $\gamma_\Phi = \sigma^2\hat{k}$. In the usual setting, k and $\hat{k}$ are related to each other by

$$\hat{k}(\xi) = \frac{1}{2\pi}\int_{\mathbb{R}^2} k(x)\,\mathrm{e}^{-ix\xi}\,\mathrm{d}x\,, \qquad \xi \in \mathbb{R}^2\,, \quad (1)$$

and vice versa

$$k(x) = \frac{1}{2\pi}\int_{\mathbb{R}^2} \hat{k}(\xi)\,\mathrm{e}^{ix\xi}\,\mathrm{d}\xi\,, \qquad x \in \mathbb{R}^2\,. \quad (2)$$

For short, we use the symbols $\mathscr{F}$ and $\bar{\mathscr{F}}$ for the Fourier transform and its co-transform, which allows to rewrite $\hat{k} = \mathscr{F}k$ and $k = \bar{\mathscr{F}}\hat{k}$.

In isotropic case $\hat{k}$ depends only on the corresponding radial coordinate $\rho = \|\xi\|$, and $\hat{k}_1(\rho) = \hat{k}(\xi)$ is the Fourier-Bessel transform of $k_1(r)$,

$$\hat{k}_1(\rho) = \frac{1}{2\pi}\int_0^\infty r\,k_1(r)\,\mathscr{J}_0(r\rho)\,\mathrm{d}r\,, \qquad \rho \geq 0\,, \quad (3)$$

where $\mathscr{J}_0$ is the Bessel function of the first kind of order 0. It is well known that the Fourier-Bessel transform of the exponential correlation function is

$$\hat{k}_1(\rho) = \sqrt{\frac{2}{\pi}}\,\frac{\lambda}{(\lambda^2+\rho^2)^{3/2}}\,, \qquad \rho \geq 0\,. \quad (4)$$

Graphs of this function are shown in Figs. 7 to 9 (red curves).

To be more flexible in modeling and characterizing paper formation, we introduce a generalized version of the exponential correlation function which depends on an additional positive parameter: the modified Bessel correlation function which is defined as

$$k_1(r) = \frac{(\lambda r)^\nu}{2^{\nu-1}\,\Gamma(\nu)}\,\mathscr{K}_\nu(\lambda r)\,, \qquad r \geq 0\,, \quad (5)$$

where Γ denotes Euler's Γ-function and $\mathscr{K}_\nu$ is the modified Bessel function of second kind of order ν. It is also here $k_1(r) \to 1$ as $r \downarrow 0$, and for $\nu = 1/2$ the exponential correlation function is obtained. The spectral density of the modified Bessel correlation function is

$$\hat{k}_1(\rho) = \frac{1}{2^{\nu-1}\,\Gamma(\nu)}\,\frac{\lambda^{2\nu}}{(\lambda^2+\rho^2)^{\nu+1}}\,, \qquad \rho \geq 0\,, \quad (6)$$

(Yaglom, 1986, p. 368).

A GEOMETRIC INTERPRETATION

Bochner's theorem states that a spectral representation exists for every continuous, positive definite function, *i.e.*, also for functions which are not necessarily covariance functions of GRFs. To give an example, we consider a macroscopically homogeneous and isotropic 2D Boolean model Ξ with identically distributed and pairwise independent random segments (Stoyan *et al.*, 1995). In fact, Boolean segment processes may serve as models for fiber systems of paper, where the fibers are 'scattered independently and uniformly' in the paper sheet. For example, Deng and Dodson (1994) and Provatas *et al.* (2000) used a Boolean segment processes for modeling fiber deposition.

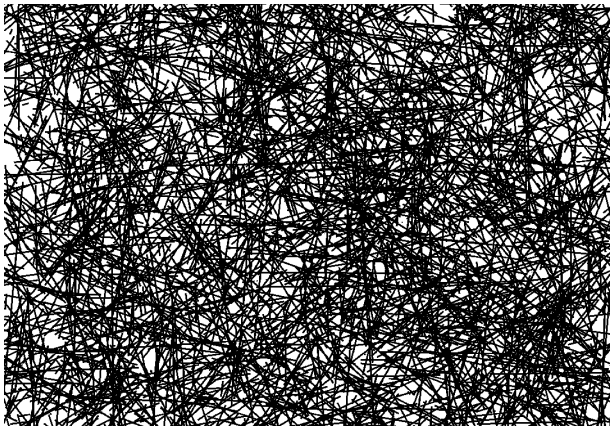

Fig. 4. *A realization of an isotropic Boolean model with segments of uniformly distributed directions and exponentially distributed lengths,* $1/\alpha = 2$ *mm,* $N_A = 10\ mm^{-2}$*; image size* $20 \times 14.1\ mm^2$.

In the following we assume that the length of the segments is exponentially distributed with the parameter α, see Fig. 4 for a realization. Then the Boolean model Ξ is uniquely characterized by the parameter α of the exponential distribution and the specific line length L_A, *i.e.*, the mean of the total segment length per unit area. Notice that $1/\alpha$ is the mean fiber length, and $N_A = \alpha L_A$ is the mean number of fibers per unit area. Then

$$g(r) = 1 + \frac{\alpha}{N_A \pi r} \mathrm{e}^{-\alpha r}, \qquad r > 0\,,$$

is the so-called pair correlation function of Ξ, defined as the density of the reduced second moment measure which is associated with random length measure L of Ξ. An explanation and a general formula of the reduced second moment measure K of Boolean segment processes is given in Stoyan *et al.* (1995), p. 186.

In order to obtain a GRF from the Boolean segment process, Ξ is smoothed with a kernel function. Let $\kappa : \mathbb{R}^2 \mapsto \mathbb{R}$ be a non-negative and bounded kernel function with $\int_{\mathbb{R}^2} \kappa(x)\,\mathrm{d}x = 1$. By $\kappa^*(x) = \kappa(-x)$ we denote the reflection of κ, and $\kappa * f$ is the convolution of the a functions with the kernel κ. Furthermore, let $u : \mathbb{R} \mapsto \mathbb{R}^2$ be an arclength parametrization of a finite immersed curve φ in $\mathbb{R}^2$, that is $\varphi = \{u(s) : 0 \le s \le \ell\}$, where u is twice continuously differentiable and ℓ is the curve length. Similar to the convolution of functions we consider the convolution of a function with a measure (in our case the length measure associated with φ), where the convolution $\varphi * \kappa$ may be defined as

$$\big(\varphi * \kappa\big)(x) = \int_0^\ell \kappa\big(x - u(s)\big)\,\mathrm{d}s\,, \qquad x \in \mathbb{R}^2\,,$$

(Katznelson, 2004). Then $\Psi(x) = \big(\Xi * \kappa\big)(x)$ is a macroscopically homogeneous random field with $\mathbb{E}\Psi(x) = L_A$, but $\Psi(x)$ is of course not a GRF. (The random field $\Psi(x)$ forms a Poisson shot noise process with respect to a random response function, Matérn, 1986, p. 31.)

If we choose κ such that it decreases sufficiently fast as $\|x\| \to \infty$, then from the central limit theorem (CLT) it follows that

$$\Phi(x) = \lim_{N_A \to \infty} \frac{1}{N_A}\big(\Xi * \kappa - L_A\big)(x)\,, \qquad x \in \mathbb{R}^2\,, \quad (7)$$

forms a GRF with $\mu = 0$ (Lane, 1984). The covariance function of $\Phi(x)$ is $\mathrm{cov}(x) = \alpha^2\big((\kappa * \kappa^*) * h\big)(x)$, where $h(x) = g(\|x\|) - 1$.

Let now $\{\kappa_\varepsilon\}_{\varepsilon>0}$ be a family of non-negative kernel functions of bounded support, $\kappa_\varepsilon(x) = 0$ for $\|x\| \le \frac{1}{\varepsilon}$. Then it follows that $\mathrm{cov}(x) \to \sigma^2 h(x)$ as $\varepsilon \downarrow 0$ for all $x \in \mathbb{R}^2$.

In the line with the above, we are setting $h_1(r) = g(r) - 1$ and call h_1 the correlation function of the Boolean model Ξ. It holds that $h_1(r) \to \infty$ as $r \downarrow 0$, *i.e.*, $h_1(r)$ is not a correlation function of a GRF. Nonetheless, the covariance measure corresponding to $h_1(r)$ is positive definite (Section 6.4 in Ohser and Schladitz, 2009) and, therefore, from Bochner's theorem it follows that there exists a Bartlett spectrum of Ξ. Moreover, the Bartlett spectrum has a density, *i.e.*, the Bessel transform

$$\hat{h}_1(\rho) = \frac{1}{\pi N_A} \frac{\alpha}{\sqrt{\alpha^2 + \rho^2}}\,, \qquad \rho \ge 0$$

of h_1 exists, which is, up to a constant factor, the same as $\hat{k}_1$ given in Eq. 6 for $\nu = -\frac{1}{2}$. This is surprising, since the curve shape of h_1 basically differs from that of k_1 given in Eg. 5, where the parameter α plays the same role as the patameter λ of the Bessel correlation function.

In other words, the GRF $\Phi(x)$ constructed by Eq. 7 inherits the second order properties of the Boolean model Ξ. This shows that there is a close relationship between 'independent and uniform scattering' of fibers in the plane (observable on a microscale) and paper formation (observable on a mesoscale), where the fiber mean length $1/\alpha$ corresponds to the formation index. However, 'independent and uniform scattering' of fibers means that there is no tendency to form fiber clusters (flocks) induced *e.g.*, by adhesion. Nevertheless, a significant formation is observable even if the fibers are 'independently and uniformly scattered', see Fig. 5 for an example.

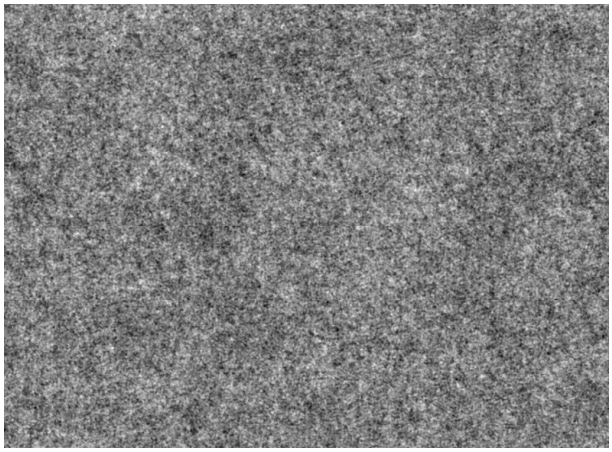

Fig. 5. *A realization of a GRF based on an isotropic Boolean model with segments of exponentially distributed lengths,* $1/\alpha = 2$ *mm, where the smoothing kernel* κ *is the probability density of the isotropic 2D Gauss distribution with* $\sigma = 0.02$ *mm. The width of the image is 102.4 mm.*

Finally we remark, that the geometric model for the fiber structure introduced above is neither the only possible nor the most simplest one. In particular, in Deng and Dodson (1994) one can find suggestions for more realistic distributions of the fiber length. However, the above model useful to derive a closed relationship between the fiber structure and the paper formation without any assumptions on flocculation.

MONTE CARLO SIMULATION

We follow the spectral approach developed by Shinozuka and Jan (1972) and others where realizations of a GRF are generated in the following two steps:

1. Let u be a random number uniformly distributed on the interval $[0,1]$, and let v be a random vector distributed with respect to the probability measure $\Gamma_\Phi/2\pi$ on $\mathbb{R}^2$. If u and v are independent, then

$$\Psi_x = \sqrt{2}\cos(2\pi u + vx)\,, \qquad x \in \mathbb{R}^2\,,$$

forms a macroscopically homogeneous and isotropic random field with mean $\mu = 0$, variance $\sigma^2 = 1$ and correlation function k.

2. Let now $\Psi_x^{(1)}, \ldots, \Psi_x^{(m)}$ are mutually independent and identically distributed random fields with $\mu = 0$, $\sigma^2 = 1$ and k. Define

$$\phi_x^{(m)} = \frac{1}{\sqrt{m}} \sum_{i=1}^{m} \Psi_x^{(i)}, \qquad x \in \mathbb{R}^2\,.$$

Then the CLT it yields that

$$\Phi(x) = \sigma \lim_{m\to\infty} \phi_x^{(m)} + \mu\,, \qquad x \in \mathbb{R}^2\,,$$

is a macroscopically homogeneous and isotropic GRF with μ, σ^2 and k.

Further details and an overview of alternative approaches are given in Lantuéjoul (2002).

But how large must m be such that $\phi_x^{(m)}$ can be accepted as a realization of $\Phi(x)$? The usual way for a suitable choice of m is based on the Berry-Esseen inequality (Korolev and Shevtsova, 2010). For the realizations of the GRFs shown in Figs. 1 to 3 the number m was empirically chosen as $m = 4\,096$, which surely is large enough as $\hat{k}(\rho)$ vanishes rapidly at infinity, see also the remark in Lantuéjoul (2002), p. 192.

ESTIMATION OF $\hat{k}$

In this section we assume that the Bartlett spectrum Γ_Φ of the observed random field $\Phi(x)$ has a density. We start from an observation of the normalized random field $f(x) = (\Phi(x) - \mu)/\sigma$ having the expectation 0 and the variance 1. In applications the field f is observed through a compact window $W \subset \mathbb{R}^2$ with the indicator function $\mathbf{1}_W$ defined as $\mathbf{1}_W(x) = 1$ if $x \in W$ and $\mathbf{1}_W(x) = 0$ otherwise. This means that the masked function $f_W(x) = f(x) \cdot \mathbf{1}_W(x)$ is considered. One should keep in the mind that the image data can be seen as a realization of f_W, where W is the (rectangular) image frame. Furthermore, we introduce a window function c_W of W defined as the auto-correlation function of the function $\mathbf{1}_W$, $c_W = \mathbf{1}_W * \mathbf{1}_W^*$, called the set covariance in Stoyan *et al.* (1995).

The function c_W is bounded and of bounded support, and thus its Fourier transform $\hat{c}_W$ exists. From the Wiener-Khintchine theorem it follows that $\mathscr{F}(c_W \cdot k) = 2\pi\,\mathbb{E}|\hat{f}_W|^2$. The power spectrum $\mathbb{E}|\hat{f}_W|^2$ of f_W is integrable, and hence the inverse Fourier transform $\bar{\mathscr{F}}$ can be applied, which yields

$$c_W \cdot k = 2\pi\,\bar{\mathscr{F}}\left(\mathbb{E}|\hat{f}_W|^2\right)\,.$$

Assume now that the origin belongs to W. Then c_W is positive for all x belonging to the interior of W, and it follows that

$$\frac{2\pi\,\bar{\mathscr{F}}\left(|f_W|^2\right)(x)}{c_W(x)} \tag{8}$$

is an unbiased estimator of $k(x)$ for all x in the interior of W.

In the isotropic case the rotation average of an estimation of k can be performed (rotation around the origin), which gives an estimation of the radial

function k_1. This leads to an estimation of the density $\hat{k}_1$ of the Bartlett-Spectrum using the 1-dimensional Fourier-Bessel transform as defined by Eq. 3.

An overview of the whole estimation procedure is given in Fig. 6. Clearly, kc_W can also be computed by auto-correlation (red marked path in Fig. 6).

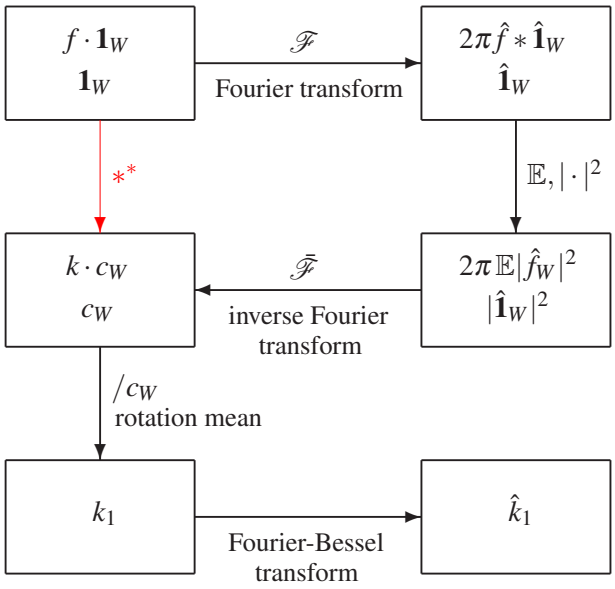

Fig. 6. *Scheme of the computation of the density function $\hat{k}_1(\rho)$. The symbol $*^*$ stands for auto-correlation of functions (convolution with the reflected function).*

It is well known that the correlation function k can be computed using the Fast Fourier Transform (FFT) with a complexity in $\mathscr{O}(n \log n)$, where n is the number of pixels of a image of $\Phi(x)$. Notice that also the window function can efficiently be computed via the inverse space using $c_W = \bar{\mathscr{F}}|\mathscr{F}\mathbf{1}_W|^2$. In the rectangular case, c_W is explicitly known (Ohser and Mücklich, 2000, p. 356). Furthermore, discrete version of the Bessel transform (necessary for computing $\hat{k}_1$ from k_1) can be based on numerical integration, *e.g.*, by Romberg's rule.

Unfortunately, the assumption of periodicity in the discrete Fourier transform (dFT) causes an overlapping effect (edge effect). This effect can be eliminated by expanding the function f_W to the window $2W$, where f_W is padded with zeros, that is $f_{2W}(x) = f_W(x)$ if $x \in W$, and $f_{2W}(x) = 0$ if $x \in 2W \setminus W$. This increases the pixel number to $4n$, still the complexity of the FFT applied to f_{2W} belongs to $\mathscr{O}(n \log n)$, which is a considerable gain compared to the usual estimation of kc_W based on auto-correlation, Fig. 6 (red path), which is of complexity $\mathscr{O}(n^2)$. Notice that data windowing using a 2D analogue of the Welch, Hann (Hamming) or Bartlett window (Press *et al.*, 2007) avoids any window expansion, but the unbiasedness of the estimator given by Eq. 8 gets lost.

The dFT (and its inverse) is usually based on a modified setting of the continuous Fourier transform. The main difference to be aware of, is that in Eqs. 1 and 2 the angular frequency $\omega = 2\pi\xi$ substitutes the frequency ξ. This has an impact on the scaling of the estimated spectral density.

Finally, we remark that sampling of f on a homogeneous point lattice induces a sampling of $\hat{f}$ on the inverse lattice, where the relationship between the original lattice and its inverse is as follows: Let U be a matrix of which the column vectors are forming a basis of the original lattice. Then the column vectors of the matrix $(U')^{-1}$ form a basis of the inverse lattice (Ohser and Schladitz, 2009, p. 66). In terms of a dFT applied to a 2D image with $n_1 \cdot n_2$ pixels of size $a_1 \cdot a_2$, the transformed image also consists of $n_1 \cdot n_2$ pixels but of size $\hat{a}_1 \cdot \hat{a}_2$, where $\hat{a}_1 = 1/(n_1 a_1)$ and $\hat{a}_2 = 1/(n_2 a_2)$.

EXPERIMENTAL RESULTS

The applicability of the method presented above is now demonstrated for three filter papers produced by wet laid cellulose fibers. The material No. 1 has a nominal grammage of 200 g/m^2 and a mean thickness of about 0.9 mm, the material No. 2 is of 90 g/m^2 and about 0.25 mm thick, and the material No. 3 is of 170 g/m^2 and about 0.7 mm thick. The mean fiber length in these materials was much longer than 2 mm.

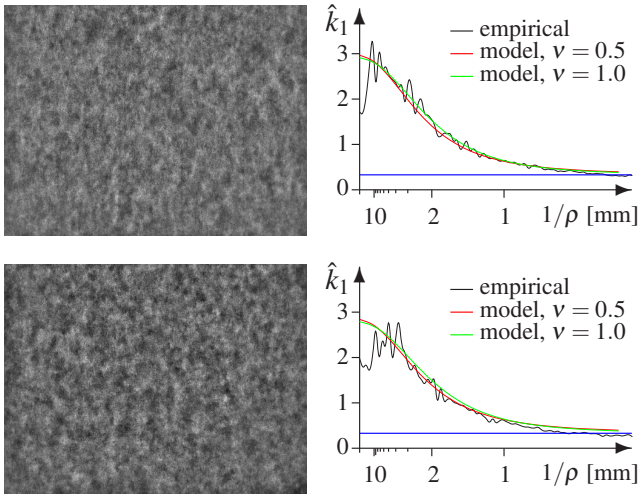

Fig. 7. *Images showing the formations of the filter papers Nr 1a (top) and Nr 1b (bottom), respectively, as well as the densities of their Bartlett spectra.*

In order to estimate the spectral density and to determine a formation index, various filter papers are scanned in the light transmission mode using a conventional CCD camera, see Figs. 7 to 9 (left) for examples. The 8-bit gray-tone images are of $1\,580 \times 1\,200$ pixels with a lateral resolution of 0.177 mm per pixel and, thus, the effective image size amounts $279.66 \times 212.40\,\mathrm{mm}^2$. The wet laying process induces a slight sheet inhomogeneity appearing as a long wave shading in the corresponding images. This shading was corrected based on a reference image which was obtained by smoothing the image data using a large Gaussian filter with the parameter $\sigma = 17.4$ mm, and where the reference image was subtracted from the original one.

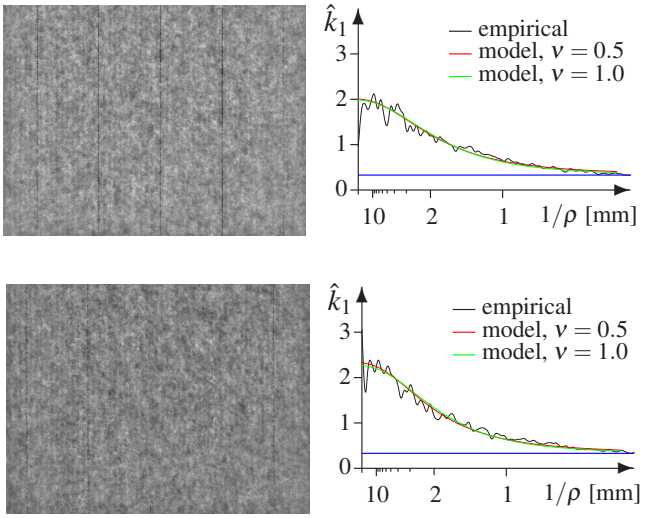

Fig. 8. *The filter papers Nr 2a (top) and Nr 2b (bottom).*

The function $\hat{k}_1$ is estimated from the image data using the method described in the previous section. The graphs of the estimates are shown in Figs. 7 to 9 (right), where $\hat{k}_1$ is given in mm^2. Note that the relative small values of the empirical $\hat{k}_1$ for wave lengths $1/\rho$ less than 10 mm might be a consequence of the applied shading correction. Generally, it is a hard problem to remove an unknown long wave shading under simultaneous keeping the spectrum of long waves in the real structure. Furthermore, because of data windowing, the fractions of long waves are estimated with a larger error than those of short waves. Nonetheless, analysis of realizations of GRFs with comparable spectral densities shows that for wave lengths less than 10 mm the function $\hat{k}_1$ is estimated from the image data with sufficiently small errors.

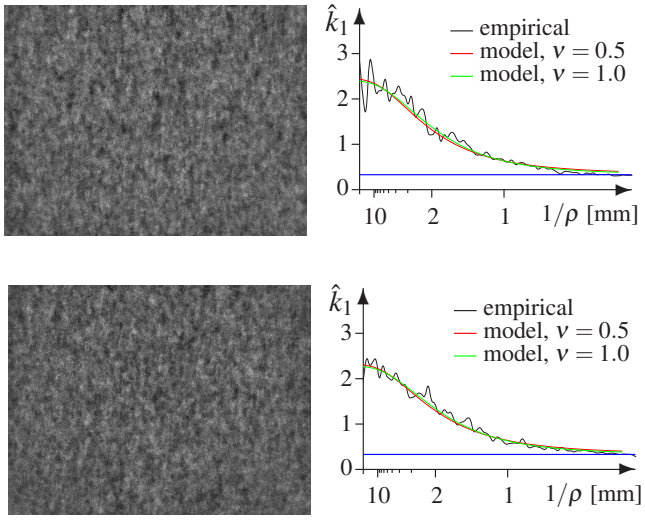

Fig. 9. *The filter papers Nr 3a (top) and Nr 3b (bottom).*

Obviously, there is a white noise observable as an additive constant c of $\hat{k}_1$,

$$c = \lim_{\rho \to \infty} \hat{k}(\rho) \approx 0.33\,\mathrm{mm}^2$$

(the blue lines in Figs. 7 to 9, right). The reason for this is not clear. Probably, a considerable fraction of this noise comes from image acquisition.

Moreover, for fixed ν the theoretical function given by Eq. 6 was fitted to the experimental data for $\rho \leq 10$ mm, where the parameter λ was estimated based on a least squares method (Figs. 7 to 9). The estimates of λ are widely independent of ν (Tab. 1), and in the most cases the fit for $\mu = 1$ is better than for $\mu = \frac{1}{2}$.

Table 1. *The formation index β and the numerical values λ for the adapted function given by Eq. 6.*

material nr.	specimen nr.	β [mm^2]	λ [mm^{-1}] $\nu = 0.5$	$\nu = 1$
1	1a	2.6	0.550	0.557
1	1b	2.3	0.564	0.568
2	2a	1.9	0.689	0.694
2	2b	2.1	0.632	0.637
3	3a	2.2	0.615	0.619
3	3b	2.1	0.635	0.638

Finally, a formation index β is the determined as the mean of the density $\hat{k}_1$ for wave lengths between 2 and 5 mm, which are relevant for industrial application.

DISCUSSION

Throughout this article it is assumed that the paper structure is isotropic, but most papers produced on papermaking machines such as those based on the principles of the Fourdrinier Machine show a clear anisotropic formation, see also Schaffnit and Dodson (1993), Scharcanski and Dodson (1996, 2000) and Sampson (2009), where the anisotropy of formation is discussed in detail. Here we only remark that anisotropic paper formation corresponds to an anisotropic spectral density $\hat{k}(\xi)$, and from an estimate of $\hat{k}$ one can derive two quantities β_1 and β_2 describing the paper formation. Let (ρ, φ) denote the polar coordinates of ξ with $\rho \geq 0$ and $0 \leq \varphi < \pi$. Then the formation index β_1 can be computed from $\hat{k}(\rho, \varphi_1)$, where φ_1 is the processing direction of paper making, and β_2 is obtained from $\hat{k}(\rho, \varphi_2)$ for the direction φ_2 perpendicular to φ_1. Usually, $\beta_1 \geq \beta_2$, and $\beta_1 = \beta_2$ in the isotropic case.

For fixed φ_1 and φ_2, the functions $\hat{k}_1^{\perp}(\rho) = \hat{k}(\rho, \varphi_1)$ and $\hat{k}_2^{\perp}(\rho) = \hat{k}(\rho, \varphi_2)$ can be seen as planar sections profiles of the spectral density $\hat{k}(x)$. From the projection slice theorem (Kuba and Hermann, 2008) it immediately follows that $\hat{k}_1^{\perp}(\rho)$ and $\hat{k}_2^{\perp}(\rho)$ can be obtained as a cosine transform of the orthogonal projections $k_1^{\perp}(r)$ resp. $k_2^{\perp}(r)$ of the estimated correlation function $k(x)$ onto the corresponding section planes, *i.e.*, the rotation mean in the scheme of Fig. 6 is replaced with the orthogonal projections onto the two section planes, and the Fourier-Bessel transform is now a simple cosine transform.

As pointed out in this article, there is a 'basic formation' related to an 'independent and uniform scattering' of the paper fibers, and even this 'basic formation' can probably not be effected by technological measures. This means that the possibility to reduce paper formation by an improved paper making technology is limited. For a paper with a given formation, the question is as follows: What is the difference between the given and the 'basic' formation? Unfortunately, the 'basic formation' can be estimated only roughly from the distribution of the fiber lengths and until now there is no safe method to find out whether the formation of a paper can be reduced or not. Notice that just Deng and Dodson stated in their monograph "that the power spectrum can give information on the flock sizes, by isolating the variance components between two scales for inspection zones" (Deng and Dodson, 1994, p. 107).

The computation of the formation index from images of transmitted light via frequency space is very efficient. However, the results from different laboratories are comparable only under the condition that the spectral density of the intensity of the transmitted light is (nearly) the same as the spectral density of the local paper grammage. Thus, when implementing a laboratory system for industrial quality control one should take care of the wavelength of the applied light, the homogeneity of illumination, the image acquisition, a possible inhomogeneity of the paper, and the edge effects involved in the computation of the spectral density. It is very helpful to make tests as the following one: the increase of the paper weight should not influence the formation and, therefore, the paper formation of a single paper sheet must be the same as that of a double sheet (both sheets of the same formation and one sheet on top of the other). Furthermore, the estimation of the spectral density should be robust with respect to variations of the lateral resolution, *i.e.*, varying the pixel size (in the range from 0.05 to 0.2 mm) should lead to only small changes in the estimated spectral density. Finally, the size of the paper sheet (*i.e.*, the size of the window W) should be large enough such that the statistical errors of the estimates are limited. From our experience we can say that an A4-sheet is sufficient. More precisely, let $\Phi(x)$ be a Gaussian random field with an exponential correlation function, $\lambda \gtrsim 0.5\,\mathrm{mm}^{-1}$, observed through a rectangular window W of the size $210 \times 297\,\mathrm{mm}^2$, then simulation studies show that the relative statistical error of estimation of $\hat{k}_1(\rho)$ is less than 5 % for all wave lengths $1/\rho \leq 5\,\mathrm{mm}$.

ACKNOWLEDGEMENT

This work was supported by the German Federal Ministry of Education and Research (BMBF) under grant MNT/03MS603C/AMiNa.

REFERENCES

Abrahamsen P (1985). A review of random fields an correlation functions, 2nd ed. Tech. Rep. 314, Blindern, Oslo.

Adler RJ (1981). The geometry of random fields. New York: John Wiley & Sons.

Adler RJ, Taylor J (2007). Random fields and geometry. New York: Springer.

Alava M, Niskanen K (2006). The physics of paper. Rep Prog Phys 69:669–723.

Antoine C (2000). GRACE, a new tool to simulate paper optical properties. In: van Lieshout M, ed., New characterisation models for fibres, pulp and paper. Joint publication of the COST action E11 working group paper.

Bergeron M, Bouley R, Drouin B, Gagnon R (1988). Simultaneous moisture and basis weight measurement. Pulp and Paper Magazine of Canada 89:173–6.

Boeckerman PA (1992). Meeting the special requirements for on-line basis weight measurements of lightweight nonwoven fabrics. Tappi J 75:166–72.

Burt BJ, Adelson EH (1983). The Laplacian pyramid as a compact image code. IEEE Trans Comm 31:532–40.

Cherkassky A (1998). Analysis and simulation of nonwoven irregularity and nonhomogeneity. Textile Res J 68:242–53.

Cherkassky A (1999). Evaluating nonwoven fabric irregularity on the basis of Linnik functionals. Textile Res J 69:701–8.

Chinga-Carrasco G (2009). Exploring the multi-scale structure of printing paper – a review of modern technology. J Microsc 234:211–42.

Cresson TM (1988). The sensing, analysis and simulation of paper formation. Ph.D. thesis, State University, New York.

Cresson TM, Luner P (1990a). The characterization of paper formation, Part 2: The texture analysis of paper formation. Tappi J 12:175–84.

Cresson TM, Luner P (1990b). Description of the spatial gray level dependence method algorithm. Tappi J 12:220–2.

Deng M, Dodson C (1994). Paper: an engineered stochastic structure. Tappi Press.

Drouin B, Gagnon R, Cheam C, Silvy J (2001). A new way for testing paper sheet formation. Compos Sci Techn 61:389–91.

Durst M, Klein GM, Moser N, Trautmann P (2007). Filtration und Separation in der Automobiltechnik. Chem Ing Techn 79:1845–60.

Farnood RR, Dodson CTJ, Loewen SR (1995). Modeling flocculation. Part I: Random disc model. J Pulp and Paper Sci 21:J348–56.

Farrington TE (1988). Soft X-ray imaging can be used to asses sheet formation and quality. Tappi J 71:140–4.

Gregersen ØW, Niskanen K (2000). Measurement and simulation of paper 3D-structure. In: van Lieshout M, ed., New characterisation models for fibres, pulp and paper. Joint publication of the COST action E11 working group paper.

I'Anson S (1995). Identification of periodic marks in paper and board my image analysis using two-dimensional fast Fourier transforms. Tappi J 78:97–106.

I'Anson S, Sampson WW (2003). Determination of spatial domain formation statistics using fast Fourier transform. Paperija Puu 85:403–8.

ISO 4046(E/F) (2012). International standard on paper, board, pulps and related terms – Vocabularity, Part 1–5. ISO Copyright Office, Geneva.

Kallmes OJ (1984). The measurement of formation. Tappi J 67:117–26.

Katznelson Y (2004). An introduction to harmonic analysis. Cambridge Mathematical Library. Cambridge: Cambridge University Press, 3rd ed.

Koch K, Ohser J, Schladitz K (2003). Spectral theory for random closed sets and estimating the covariance via frequency space. Adv Appl Prob 35:603–13.

Korolev VY, Shevtsova IG (2010). On the upper bound for the absolute constant in the Berry-Esseen inequality. Th Prob Appl 54:638–58.

Kuba A, Hermann G (2008). Some mathematical concepts for tomographic reconstruction. In: Banhart J, ed., Advanced tomographic methods in materials science and engineering. Oxford: Oxford University Press, 19–36.

Lane JA (1984). The central limit theorem for the Poisson shot-noise process. J Appl Prob 21:287–301.

Lantuéjoul C (2002). Geostatistical simulation – models and algorithms. Berlin: Springer.

Lien HC, Liu CH (2006). A method of inspecting non-woven basis weight using the exponential law of absorption and image processing. Textile Res J 76:547–58.

Matérn B (1986). Spatial variation. Berlin: Lecture notes in statistics 36, Springer-Verlag.

McDonald JD, Rarrell WR, Stevens RK, Hussain SM, Roche AA (1986). Using an on-line light transmission gauge to identify the source of grammage variations. J Pulp and Paper Sci 12:J1–9.

Norman B (1986). The formation of paper sheets, Chapter 6. In: Bristow AJ, Kolseth P, eds, Paper, structure and properties, vol. 8 of Int Fiber Sci and Techn Series. Marcel Dekker.

Norman B, Wahren D (1974). The measurement of mass distribution in paper sheets using a beta radiograph method. Svensk Papperstilding 11:397–406.

Norman B, Wahren D (1976). Mass distribution and sheet properties of paper. In: Fundamental properties of paper to its end uses, Trans. Symp. London: B.P.B.I. F.

Ohser J, Mücklich F (2000). Statistical analysis of microstructures in materials science. Chichester, New York: J Wiley & Sons.

Ohser J, Schladitz K (2009). 3D images of materials structures – processing and analysis. Weinheim, Berlin: Wiley VCH.

Pourdeyhimi B, Kohel L (2002). Area-based strategy for determining web uniformity. Textile Res J 72:1065–72.

Praast H, Göttsching L (1991). Formation graphischer

Papiere. Das Papier 45:333–47.

Press WH, Teukolsky SA, Vetterling WT, Flannery BP (2007). Numerical recipes – The art of scientific computating, 3rd Ed. Cambridge University Press.

Provatas N, Alava MJ, Ala-Nissila T (1996). Density correlations in paper. Phys Rev E 54:R36–8.

Provatas N, Haataja M, Asikainen J, Majaniemi S, Alava M, Ala-Nissila T (2000). Fiber deposition models in two and three dimensions. Colloids Surfaces A 165:209–29.

Robertson AA (1956). The measurement of paper formation. Pulp and Paper Magazine of Canada 55:119–27.

Sampson WW (2009). Modelling stochastic fibrous materials with mathematica. Engineering materials and processes. London: Springer.

Sara H (1978). The characterization and measurement of paper formation with standard deviation and power spectrum. Ph.D. thesis, Helsinki University, Helsinki.

Schaffnit C, Dodson CTJ (1993). A new analysis of fiber orientation effects on paper formation. Paperija Puu 75:68–75.

Scharcanski J (2006). Stochastic texture analysis for measuring sheet formation variability in the industry. IEEE Trans Instrum Meas 55:1778–85.

Scharcanski J, Dodson CTJ (1996). Texture analysis for estimating spatial variability and anisotropy in planar structures. Opt Eng J 35:2302–8.

Scharcanski J, Dodson CTJ (2000). Stochastic texture image estimators for local spatial anisitropy and its variability. IEEE Trans Instrum Meas 49:971–9.

Scholz M, Claus B (1999). Analysis and simulation of nonwoven textures. Z Angew Math Mech 79:237–40.

Shinozuka M, Jan CM (1972). Digital simulation of random processes and its applications. J Sound Vibration 25:111–28.

Stoyan D, Kendall W, Mecke J (1995). Stochastic geometry and its applications. Chichester: J. Wiley & Sons, 2nd ed.

Van den Akker JA (1949). Scattering and absorption of light in paper and other diffusing media. Tappi J 32:498–501.

Wang X, Georganas ND, Petriu EM (2011). Fabric texture analysis using computer vision techniques. IEEE Trans Instrum Meas 60:44–56.

Waterhouse JF, Hall MS, Ellis RL (1991). Strength improvement and failure mechanisms, 2. Formation. Tech Rep Project 3469, Report II, Institute of Paper Science and Technology (API), Atlanta, Gorgia.

Xu B (1996). Identifying fabric structures with fast Fourier transform techniques. Textile Res J 66:496–506.

Yaglom AM (1986). Correlation theory of stationary and related random functions I: Basic results. Springer Series in Statistics. New York: Springer.

Yuhara T, Hasuike M, Murakami K (1986). Application of image processing technique for analysis on sheet structure of paper, Part 1: quantitative evaluation of 2-dimensional mass distribution. Japan Tappi 40:85–91.

Image Anal Stereol 2013;32:89-99 doi:10.5566/ias.v32.p89-99
Original Research Paper

AUTOMATIC OBJECT DETECTION AND SEGMENTATION OF THE HISTOCYTOLOGY IMAGES USING RESHAPABLE AGENTS

MEHDI ALILOU✉,[1,2] AND VASSILI KOVALEV[2]

[1]Department of Computer Science, Khoy Branch, Islamic Azad University, Khoy, Iran; [2]Department of Biomedical Image Analysis, United Institute of Informatics Problems, National Academy of Sciences, Minsk, Belarus
e-mail: me.alilou@gmail.com, vassili.kovalev@gmail.com
(Received December 15, 2012; revised May 14, 2013; accepted June 11, 2013)

ABSTRACT

The aim of this study is to suggest a method for automatic detection and segmentation of the target objects in the microscopic histology/cytology images. The detection is carried out by rectangular shapes then segmentation process starts utilizing flexible agents which are able to move and change their shapes according to a cost function. The agents are rectangular at the beginning then they gradually fit to the corresponding objects using a stochastic reshaping algorithm. The iterative reshaping process is controlled by a cost function and it is resulted in a finer segmentation of the target objects. The cost functional of the proposed method comprised of three terms including the prior shape, regional texture and gradient information. The experiments were carried out using a publicly available microscopy image dataset which contains 510 manually-labeled target cells. The segmentation performance of the proposed method is compared with another state of the art segmentation method. The results demonstrate satisfactory detection and segmentation performance of the proposed method.

Keywords: histocytology images, object detection, reshapable agents, segmentation.

INTRODUCTION

Automated image analysis of cells and tissues has been an active research field in biomedical informatics for the past three decades (Mulrane *et al.*, 2008; Gurcan *et al.*, 2009). However, it has recently attracted increased attention due to developments in computer and microscopy hardware. Nowadays with everlasting perfection of microscopy imaging technology, an increasing volume of high quality medical images becomes available. This huge volume of images, both in routine clinical work and in research and development, calls for an increasing degree of automation of image analysis processes.

The aim of any segmentation method is to extract boundary elements belonging to the same structure and integrate these elements into a coherent and consistent model of the structure. The recent literature suggests that investigation for robust and practical cell/nuclei segmentation methods, as a critical step of automated image analysis, is still on its way. According to Wang *et al.* (2007) the automated approaches to segmentation could be categorized generally in three different classes: supervised (model based), unsupervised (inspired by low level image properties) and weakly supervised approaches.

Supervised segmentation methods use classification algorithms such as k-nearest-neighbor, Bayes classifier, Neural Networks, and Support Vector Machines (SVMs). These classifiers learn models of the characteristics of different tissue types from labeled examples and adapting the resultant models for segmenting new images. Supervised algorithms could be slow to train and may require a substantial amount of manually segmented data. In contrast, unsupervised segmentation methods divide an image into homogeneous regions based on an objective measure of homogeneity. Such unsupervised techniques do not require any training data. However they can lead to groupings that do not correspond to the desired conceptual tissue categories. Furthermore, their ad-hoc nature prevents them to be applied to a wide range of microscopy images. Weakly supervised approaches arise from the idea of using together a large amount of unlabeled data which is often easy to obtain and a few of labeled data which is hard to obtain, since it requires human experts.

To overcome the segmentation problem in histocytology images, a number of different approaches have been proposed in context of various biomedical applications. Thresholding approaches with a fixed or adaptive threshold values are the most straightforward techniques of segmentation which have been employed in Korde *et al.* (2009) for nuclei segmentation of bladder and skin tissue images. However, the global thresholding technique supposes that the nuclei have a range of intensities

that is sufficiently different from the background. This is generally not true, since the background varies significantly. The result may be improved by adaptive thresholding, but large intensity variations between and within the nuclei will cause the segmentation procedure to fail.

Moreover, there have been other approaches that incorporate more complex segmentation techniques such as region growing, active contours and edge/contour based methods. Region growing methods are based on the assumption that the objects consist of connected regions of similar pixels. Region growing and merging methods are commonly used for segmentation of cells and nuclei from fluorescence microscopy images as shown in Adiga *et al.* (2006). However, large intensity variations between and within the nuclei may cause these methods to fail.

Although active contour models or snakes are widely used in medical image segmentation, these methods are sensitive to initialization of a start contour or a seed inside each object of interest. Furthermore, they may lead to poor segmentation results if applied to cluttered images. Several methods have been proposed to adapt active contours to the nature of histocytology images. For instance, a method suggested in Ali and Madabhushi (2012) utilizes active contour algorithm for segmentation of histopathological images of breast and prostate tissues.

Edge/contour based methods are another class of methods that have been used widely in medical image segmentation. Typically they are considered as unsupervised or automatic methods. In recent years there have been efforts to apply these methods on histocytology images. For instance, a gradient flow tracking method which is used for segmentation of touching cells is proposed in Li *et al.* (2008). Another recent study that uses a contour-based cell detection and segmentation algorithm is proposed in Wienert *et al.* (2012). However, these methods can fail due to complicated spatial and color patterns of the histocytology images.

The aim of this paper is to develop a method for localization and segmentation of the target objects in histocytology images. Unlike fully automatic (unsupervised) methods, which are suitable for very specific kinds of microscopy images, the proposed method is model based. That is, to achieve more flexible and general solution the features of the interested object samples are given to system through a training stage. The framework of the proposed approach is depicted in Fig. 1. The input images are processed in five steps including preprocessing, object detection by rectangular window, stochastic reshaping and contour's cost evaluation.

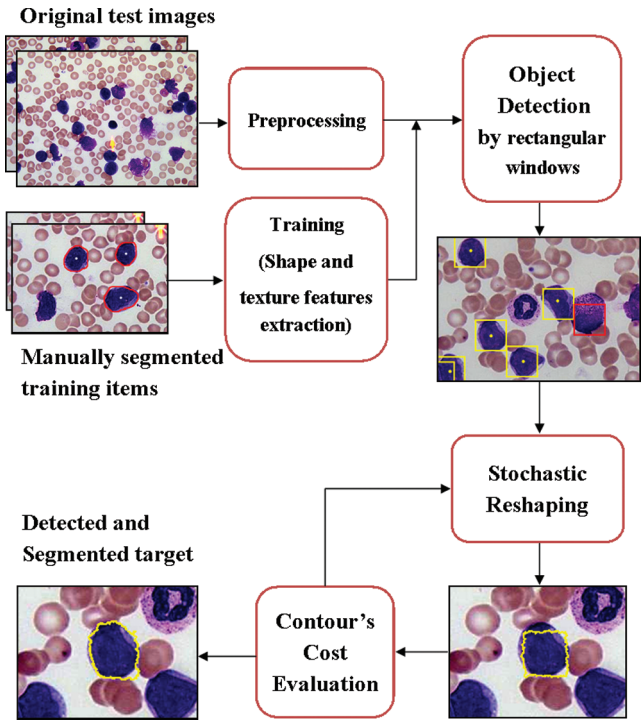

Fig. 1. *The framework of the proposed method.*

Localization of the potential objects is carried out through scanning the whole images and matching the rectangular regions of an image with a template obtained from the training stage. Afterwards, the contours of detected rectangular regions are reshaped iteratively to achieve finer segmentation levels. An iterative stochastic contour reshaping algorithm is proposed to reshape the contours and to fit the objects of the interest properly. The reshaping process is controlled by a cost function including the prior shape, regional texture and gradient terms. The performance of the proposed method is evaluated in both detection (rectangular regions) and finer segmentation levels and compared with the well-known region growing method. The precision and recall measures are used for the assessment of the object localization. Furthermore, the segmentation performance is compared against the manually segmented ground truth using the Jaccard and Zijdenbos similarity indices.

The reminder of this paper is organized as follows: the next section introduces the dataset and describes preprocessing stage. Then, rectangular detection of the target objects will be described next. Afterwards, we describe the stochastic contour reshaping algorithm which is proposed to finer segmentation of the rectangular detected objects. The results section reports the detection and segmentation performance results of the proposed method. Finally we conclude with a discussion of our results.

MATERIALS AND METHODS

As a publicly available dataset, the acute lymphoblastic leukemia image database (ALL-IDB1) is employed in our experiments. It is introduced in Labati *et al.* (2011) and includes 109 images in JPG format with 24 bit color depth. The images are captured with a PowerShot G5 camera and their resolution is 2592×1944. The dataset contains about 39000 blood elements, where the lymphoblasts (immature lymphocytes) as the target objects have been labeled by the oncology experts. The number of labeled lymphoblasts presented in the ALL-IDB1 is 510. An example image of the dataset is depicted in Fig. 2. The target objects are identified by the yellow dots.

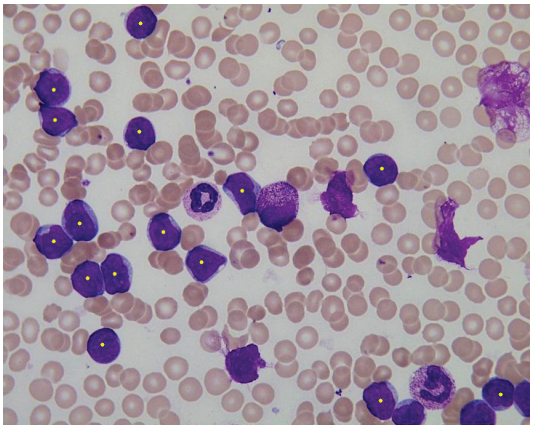

Fig. 2. *An example image of the ALLIDB1 dataset. The lymphoblasts (target objects) are labeled by yellow dots inside.*

PREPROCESSING

Prior to applying the method to dataset images, a preprocessing step is carried out. This step includes color quantization of the images. Since the co-occurrence matrices are used for describing the image content, depending to intensity or color ranges, their dimensionality could be too large. Fortunately the stained blood smear or tissue images have considerably limited color spectrum. As confirmed by the sample image presented in Fig. 2, there are few dominant colors (hues of blue, purple and pink) in the images obtained from staining techniques. Thus, this allows us to efficiently reduce the color space down to k quantized colors using uniform quantization algorithm. To avoid large and sparse color co-occurrence matrices, which affects the time performance of the method, the number of quantized colors should be small. On the other hand, it should be large enough such that different regions of the image can be described and identified correctly. Depending to the spatial structure and color patterns of the images the value of k could be 16, 32 or even more quantized colors. In this paper regarding the time efficiency and detection performance issues we have selected 32 quantized colors experimentally.

TRAINING

A training set S_l of regions representing the structure of the interest (lymphoblasts) is obtained before starting of the detection procedure. Each region, $Reg \in S_l$, of the training set consists of a set of pixels whose texture characteristics are described by the color co-occurrence matrices, as shown in Kovalev *et al.* (2011). The texture sufficiently represented by a three dimensional matrix $W(\Delta_{ij}, ci, cj)$ where ci and cj are indices of suitably quantized RGB color intensities of the pixels i and j, Δ_{ij} is the Euclidean distance between pixels i, $i = (x_i, y_i)$ and j, $j = (x_j, y_j)$ and W is the frequency of the spatial occurrence of such elementary image structures on the image plane.

As it can be seen from the Fig. 2 the target objects (lymphoblasts) are similar to each other, whereas remaining objects of the non-target classes (*i.e.,* any types of objects except the lymphoblasts) are visually different from the target class. This is confirmed by the multidimensional scaling analysis of the texture feature vectors of the samples belonging to the target and other non-target classes. Fig. 3 depicts an approximated 2D distance distribution of the scaled feature vectors belonging to the mentioned samples. The green circles in Fig. 3 represent the scaled vectors of the target class, the red ones represent the background of the images (red blood cells), the black, the yellow and the pink icons represent other types of white blood cells like basophils, eosinophils, monocytes and non-blast lymphocytes. The target samples are close to each other in the feature space whereas other samples of non-target classes are spread over. Since the lymphoblasts can be distinguished and separated from the others by their distance in the feature space, we considered lymphoblast as the only class in the training set and all the remaining objects are considered as the background.

According to the mentioned reasons, there is no need to annotate too many objects as the training samples. The ratio of the annotated items with regard to the total number of the target objects is about 10% (51 annotated out of 510 manually labeled target items). Moreover, due to homogeneity of the target objects they can be distinguished from the others by a proper distance threshold in the feature space as confirmed in Fig. 3. Therefore there is no need to employ classifiers like SVM.

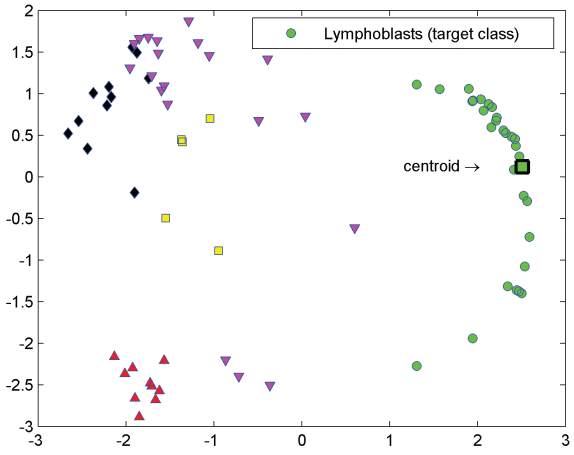

Fig. 3. *The results of multidimensional scaling analysis of the samples belonging to various classes. The green circles represent samples of the target class (lymphoblasts). The red, black, yellow and the pink icons represent other types of blood cells (non-target classes).*

DETECTION OF THE TARGET OBJECTS

The detection procedure is carried out by scanning the images with a rectangular scanning object. Since the size of lymphoblasts is homogeneous, the rectangular scanning object's size, s_{rec}, is determined based on average size of the bounding boxes in the training set. The detection procedure consists of 3 main steps which are executed iteratively until complete scanning of an image. The first step is moving the rectangular scanning object over an image. It starts from (0,0) coordinate of the image and moves to the end of it row by row in 10 pixels increments. The second step is texture feature extraction of a region identified by the rectangular object which is carried out by computing the co-occurrence matrix (W) of that region. The third and most critical part is the classification of the rectangular region. The decision whether a region is belong to the target class or not, is resolved by measuring the distance between feature vectors of that region and centroid of the training set in the feature space. Let us denote v, $v \in \mathbb{R}^n$ as the co-occurrence matrix of an image region identified by the rectangular scanning object during detection process, and u, $u \in \mathbb{R}^n$ as the texture vector of the training set's centroid which is obtained from the co-occurrence matrices of the training set items. To classify the region into the proper class, the v and the u vectors are normalized via:

$$\hat{v} = \frac{v}{\|v\|}, \qquad \hat{u} = \frac{u}{\|u\|}, \tag{1}$$

then the city block distance of normalized vectors is determined by:

$$d_c = \sum_{i=1}^{n} |\hat{v}_i - \hat{u}_i| \ . \tag{2}$$

Having $\bar{d}_c$ normalized to [0,1], if the value of $\bar{d}_c$ is less than or equal to a distance threshold t_{dist}, $t_{\text{dist}} \in [0,1]$, the region is regarded as a target region otherwise it will be considered as background class. To optimize the detection performance, a range of t_{dist} values is examined in our experiments and the optimum t_{dist} value is selected regarding the precision and recall values of the detection procedure.

The graphical output of applying detection procedure to an example image is depicted in Fig. 4. The yellow rectangles show the correctly detected target objects whereas the red ones indicate the false alarms.

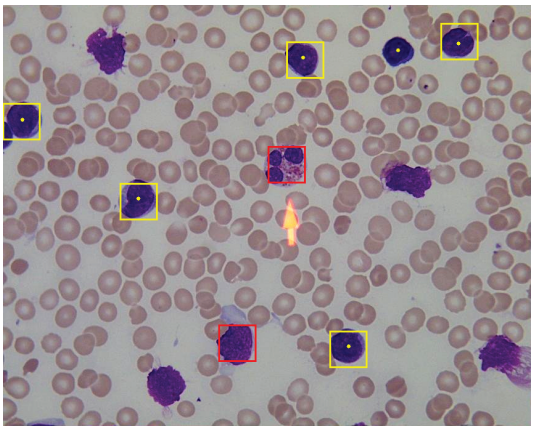

Fig. 4. *The result of rectangular detection procedure applied to an example image. The yellow rectangles represent true positives, the red ones represent false positives.*

As a result of this phase we end up with the localization (detection) of the target objects. The contour pixels of a rectangular agent indicating to a target object will be regarded as the initial set of pixels of an reshapable agent. The agents will be reshaped in the next phase of the method's processing pipeline to achieve finer segmentation of the target objects.

STOCHASTIC RESHAPING

To accomplish segmentation of the targets, stochastic reshaping contour algorithm is proposed. It is a customized implementation of region-, shape- and gradient based active contours. The notion of active contours is utilized and adapted to make it applicable to a range of histology/cytology images. It is known that the basic idea of active contour

model is to evolve a curve, subject to constraints from a given image I, in order to achieve an optimal state and therefore to outline the object. Active contours and level set methods have been widely used and progressively improved for medical image segmentation. The concept of active contours was introduced in Kass *et al.* (1988) for segmentation of objects in images using dynamic curves.

Let Ω be a bounded open subset of $\mathbb{R}^2$, with $\partial\Omega$ as its boundary. Let $I : \bar{\Omega} \to \mathbb{R}$ be a given image. Usually, $\bar{\Omega}$ is a rectangle in the plane and I takes values between 0 and 255. Denote by $C(S) : [0,1] \to \mathbb{R}^2$ a parameterized curve. According to Chan and Vese (2001) the energy functional of the active contour model is expressed as:

$$E(C) = E_1(C) - E_2(C) \,. \tag{3}$$

The first term controls the rigidity and elasticity of the contour and represents the internal energy of the active contour and is defined as:

$$E_1(C) = \alpha \int_0^1 \left|C'(s)\right|^2 \mathrm{d}s + \beta \int_0^1 \left|C''(s)\right|^2 \mathrm{d}s \,, \tag{4}$$

where α, β are positive parameters. The second term ($E_2(C)$) represents external energy which attracts the model to the target objects in the image I and is defined as:

$$E_2(C) = \lambda \int_0^1 |\nabla I(C(s))|^2 \mathrm{d}s \,, \tag{5}$$

where λ is a positive parameter and $\nabla I(C(s))$ represents the gradient of the contour.

Regardless of internal and external forces implementation of an active contour based models, the evolving curve C in Ω, as the boundary of an open subset ω of Ω (i.e. $\omega \subset \Omega$ and $C = \partial\omega$) is represented by a Lipschitz function $\phi : \Omega \to \mathbb{R}$ such that:

$$\begin{cases} C = \partial\omega = \{(x,y) \in \Omega : \phi(x,y) = 0\} \,, \\ \text{inside}(C) = \omega = \{(x,y) \in \Omega : \phi(x,y) > 0\} \,, \\ \text{outside}(C) = \Omega \setminus \bar{\omega} = \{(x,y) \in \Omega : \phi(x,y) < 0\} \,. \end{cases} \tag{6}$$

Here, inside(C) denotes the region ω, outside(C) denotes the region $\Omega \setminus \bar{\omega}$.

In the classical form of its implementation, the active contour model is forced to move on locations of maxima $|\nabla I|$ under limitations provided by first two terms by minimizing the energy in Eq. 3. The boundary-based approaches such as geodesic/geometric active contours have become popular on account of their reliable performance when strong object gradients are present. However, as only the edge information is utilized, their performance is limited by the strength of the image gradient. These models are typically unable to handle object occlusion or scene clutter and as a result multiple overlapping objects are often segmented as single object.

The basic idea behind our stochastic reshaping approach is to change the behavior of the active contour and make it applicable to a range of histology/cytology images. Hence, we propose a cost function which is used inside reshaping algorithm and consisted of two components. The proposed cost function is defined as:

$$F = F_1 + F_2 \,, \tag{7}$$

where the first component (F_1) represents the internal force of the proposed cost function and it is responsible to preserve the integrity of the contour. It controls weather integrity of the border is kept or not due to shrinkage or expansion actions applied to border points P_i. It is defined as:

$$F_1 = \begin{cases} 0 \,, & \text{if contour is continuous} \,, \\ \infty \,, & \text{if contour is discontinuous} \,. \end{cases} \tag{8}$$

The second component of the cost function is defined as follows:

$$F_2 = \gamma \triangle V_{\text{texture}} + \iota \Delta V_{\text{shape}} - \eta \nabla I(C) \,, \tag{9}$$

where γ , η and ι are weighting coefficients. The first term of the F_2 forces the agent's contour toward the regions that have similar texture to its prototype. The prototype is the most similar training item to the initial state of an agent in terms of internal texture and contour's shape. Due to homogeneity of the target objects we chose centroid of the training set as the prototype. Similarly, the second term of the F_2 forces the agent's contour to get a similar shape like its prototype's shape. Finally, the third term encourages the contour toward the edges. Having $\bar{u}, \bar{v} \in \mathbb{R}^n$ as normalized texture feature vectors of ω (i.e. area bordered by the contour) and its prototype respectively, $\Delta V_{\text{texture}}$ is the city block distance between $\bar{u}$ and $\bar{v}$ at any reshaping step. Similarly, having ρ, ψ as shape feature vectors of the counter (C) and its prototype respectively and $\bar{\rho}, \bar{\psi}$ as their normalized forms, ΔV_{shape} represents the city block distance between $\bar{\rho}$ and $\bar{\psi}$ at any iteration step in the reshaping process. The final term $\nabla I(C)$ of the F_2 represents the average gradient value of the agent's contour at any reshaping step. Taking into account the requirements of reasonable computational complexity, simple shape features were utilized to shape description of the contour in every reshaping step. The shape feature vector is defined as follows:

$$\rho = (\rho_1, \rho_2, \rho_3, \rho_4) \,, \tag{10}$$

where $\rho_1 = P_c$ is the perimeter of contour, $\rho_2 = A_c$ is the area limited by the contour and $\rho_3 = R_c$ is the roundness of the contour which is defined as:

$$R_c = \frac{4\pi A_c}{P_c^2} \,. \tag{11}$$

The last item of shape feature vector, $\rho_4 = E_c$ represents the eccentricity of the contour which is defined as:

$$E_c = \frac{d_{\max}}{d_{\min}} \,, \tag{12}$$

where $d_{\max}$, $d_{\min}$ are the length and the width of contour's bounding box respectively.

The reshaping process is described in Table 1. The three major components of the reshaping algorithm are: the *"compute distance to centroid"*, *"Shrink"* and *"Expand"* actions. The *"compute distance to centroid"* component includes extraction of shape, texture and gradient features of the current state of an agent and calculate the cost of its current state using Eq. 7 in every reshaping state (initial, shrunk or expanded). According to the algorithm a trial shrinkage or expansion of the agent will be accepted if the value of cost function F of Eq. 7 in every step becomes less than its value in the previous step. In other words, iterative changes of contour made by *Shrink* and *Expand* actions should decrease the value of cost function. Otherwise, the effect made by shrinkage or expansion actions on the contour will be rolled back.

Table 1. *Reshaping procedure.*

Input: $C \cup \omega$, contour and body pixels of the rectangular agent.
Output: New $C \cup \omega$ fitting region of the interest.
$Cost_{\text{initial}} \Leftarrow$ compute rectangular agent's distance to centroid using cost function F
$Cost_{\min} \Leftarrow Cost_{\text{initial}}$
repeat
  $C_t, \omega_t \Leftarrow$ Shrink(C, ω)
  $Cost_t \Leftarrow$ compute shrunk agent's distance to centroid using cost function F
  if $Cost_t < Cost_{\min}$ **then**
    $Cost_{\min} \Leftarrow Cost_t, C, \omega \Leftarrow C_t, \omega_t$
  end if
  $C_t, \omega_t \Leftarrow$ Expand(C, ω)
  $Cost_t \Leftarrow$ compute expanded agent's distance to centroid using cost function F
  if $Cost_t < Cost_{\min}$ **then**
    $Cost_{\min} \Leftarrow Cost_t, C, \omega \Leftarrow C_t, \omega_t$
  end if
until ($Cost_{\min} < a \times Cost_{\text{initial}}$)

The shrinkage action starts with selection of a random shrink point, P_{shrink}, from the list of agent's border points. Then, the contour points which are located in distance r of shrink point will be shrunk in such a way that the integrity of contour is kept. Similarly, expansion starts with selection of a random expansion point, P_{expand} , such that the Euclidean distance between the expansion point and shrink point is greater than a distance threshold, d_t. In order to avoid overlapping of expansion and shrinkage areas on the contour and keep them far from each other, P_{expand} should be located on the position of contour so that $d_t > 2 \times r$. After locating the P_{expand} in a proper position, the contour points that are located in distance r of the expand point will be expanded in such a way that the integrity of contour is kept. Fig. 5 depicts a schematic view of the proposed reshaping process.

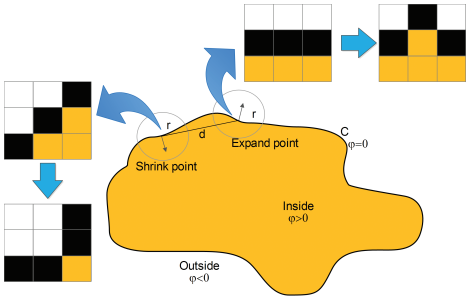

Fig. 5. *A schematic view of stochastic contour reshaping process. In every expansion or shrinkage event the state of the shrunk and expanded points are changed according to the predefined rules applied in* 3×3 *neighborhood window of these points.*

Fig. 6 represents a reshapable agent imposed on an example image. The evolution of the agent's contour is shown from left to right.

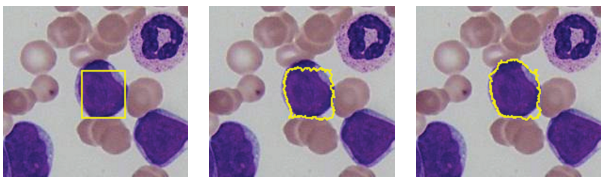

(a) (b) (c)

Fig. 6. *The contour evolution of a rectangular agent due to stochastic reshaping process from left to right. (a) The rectangular detected target object, (b) Agent's contour after 50 reshaping iterations. (c) Agent's contour after150 reshaping iterations.*

METHOD VALIDATION

In order to evaluate the performance of the proposed method, the accuracy of the method is measured in both detection and segmentation steps.

Furthermore, the segmentation quality of the method is compared with a state of the art method. In the detection level the accuracy is measured by calculation of the detection precision and its recall. The precision can be defined as the probability that detector's signal was recognized correctly. The recall is the probability that all the ground truth objects are recognized. The detection procedure is applied to the data set images and true positive (Tp), false negative (Fn) and false positive (Fp) events is determined using the ground truth information of the target objects. The precision and recall were computed as follows:

$$\text{Precision} = \frac{Tp}{Tp+Fp}\,, \tag{13}$$

$$\text{Recall} = \frac{Tp}{Tp+Fn}\,. \tag{14}$$

In the segmentation level, the stochastic reshaping algorithm is applied to the detected rectangular agents and the segmentation similarity index or segmentation agreement to the ground truth is measured. The results are compared with the segmentation results of a state of the art method (region growing based method). Two segmentation similarity indices (the Zijdenbos and the Jaccard) are used to measure the segmentation performance. The Zijdenbos similarity index, as shown by Zijdenbos *et al.* (1994), is a well-known metric for performance assessment of any region-based segmentation method. It measures the percentage of the overlapping ratio between the two shapes A (automatic segmented area) and M (manually segmented area or ground truth). It is defined as:

$$ZSI = 2 * \frac{|A \cap M|}{|A| + |M|}\,, \tag{15}$$

where A and M are the binary images generated by the proposed method and manual segmentation of image (ground truth), respectively.

In addition to ZSI similarity index, the Jaccard similarity index is also calculated to provide comprehensive evaluation of the method. The Jaccard similarity index is defined as:

$$JSI = \frac{|A \cap M|}{|A \cup M|}\,. \tag{16}$$

Furthermore, the segmentation error indices are calculated via:

$$EF = \frac{\bar{M} \cap A}{M}\,, \tag{17}$$

$$MF = \frac{M \cap \bar{A}}{M}\,, \tag{18}$$

where the EF stands for extra fraction and shows the over segmentation fraction and the MF stands for miss fraction and represents the under segmentation fraction of any segmentation method.

RESULTS

The experimental results are organized into two subsections. In the first part, we report the manner of the parameters choice and the performance of the rectangular detection algorithm. Afterwards, in the second part of the results, we report the parameters choice of the reshaping algorithm and the segmentation quality of the proposed method using ZSI, JSI, EF and MF indices. Then, the segmentation results are compared to the results of a region growing based method.

DETECTION RESULTS

Three main parameters that influence the detection accuracy of the rectangular detection procedure are: the number of quantized colors (k), the scanning window size (s_{rec}) and the distance of rectangular region to the centroid of training set in the feature space (t_{dist}). Considering trade-off between the performance and computational cost, we have run several experiments and set different values to these parameters to find optimal combination of the parameters experimentally. Setting fixed values to k and t_{dist} and changing the value of window size we noticed that the optimal value for this parameter is the average size of training items bounding boxes. Similarly, having a fixed value to the window size and changing the values of $k \in \{16, 32, 64\}$ and $t_{\text{dist}} \in [0, 1]$, we measured the precision and recall of the detection procedure. Fig. 7 depicts the precision-recall curves of the detection procedure. For each value of the parameter k (*i.e.*, the number of quantized colors) there is a curve which is built up based on different t_{dist} values.

As it is obvious from the figure, the detection accuracy for the curves with $k = 64, 32$ is considerably higher than the curve with $k = 16$. Taking into account that the detection performance for $k = 64$ colors is slightly higher than $k = 32$ as well as detection procedure for $k = 64$ colors needs 64×64 co-occurrence matrices, we chose $k = 32$ colors due to the following reasons. Its performance is almost the same with the $k = 64$ and it needs twice less data structures and computational time than the case with $k = 64$ colors.

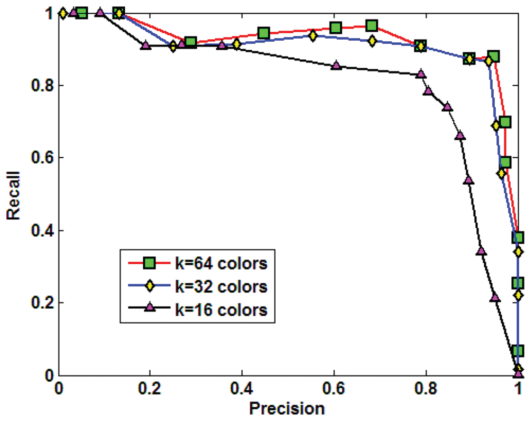

Fig. 7. *Precision vs. recall curves of the detection procedure for different numbers of quantized colors (k).*

The optimal combination of the mentioned parameters, *i.e.*, s_{rec} = average bounding box size of the training items, k=32 and $t_{\text{dist}} = 0.53$, resulted in acceptable detection accuracy with precision = 0.94 and recall = 0.88.

SEGMENTATION RESULTS

The main influencing parameters on segmentation performance are the three weighting coefficients of the Eq. 9 (γ, η and ι). Moreover, the parameter $a \in [0,1]$ of Table 1 which controls the reshaping iterations has significant role in final segmentation quality. Again, to find the optimal combination of parameters we have run several experiments. Since the size of the target objects in the current dataset are homogeneous and all comparisons in the reshaping process are made to the centroid of the training set, through experiments we noticed that the influence of the size coefficient in this specific dataset is trivial. Therefore, we set the value of ι to zero then a range of values adaptively are set to the texture and the gradient weighting coefficients (γ, η) to find the their optimal values. The number of reshaping iterations has been set to a fixed number while investigating the optimal values of the γ and η parameters. The curve which is shown in Fig. 8 gives an indication of how segmentation quality changes due to changes in the values of γ and η. The optimal combination of the mentioned parameters, *i.e.*, $\gamma = 0.51$, $\eta = 0.49$ and $\iota = 0$, for a fixed number of reshaping iterations leads to segmentation agreement to the ground truth with $ZSI = 0.83$.

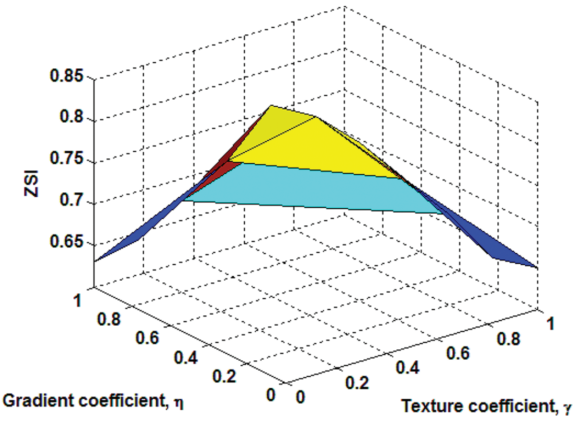

Fig. 8. *The effect of changing the values of γ, η to final segmentation agreement. the γ and η are weighting coefficients in the proposed cost function and ZSI is the segmentation similarity index.*

Having the optimal values of the weighting parameters of the cost function (γ, η and ι), regarding time efficiency and segmentation quality, a set of values has been assigned to $a \in [0,1]$ to measure its effect on final segmentation agreement. Table 2 represents the effect of the parameter a on the final segmentation agreement of the proposed method.

Table 2. *The effect of the parameter a on final segmentation agreement of the proposed method in both rectangular and reshaped levels. (ZSI_{rect}: average segmentation agreement of the images segmented by the rectangular agents, ZSI_{reshaped}: average segmentation agreement of the images segmented by the reshaped agents, iteration: the number of the reshaping iterations).*

a	ZSI_{rect}	ZSI_{reshaped}	*iteration*
1	0.78	0.785	1
0.9	0.78	0.791	58
0.8	0.78	0.795	146
0.7	0.78	0.812	198
0.6	0.78	0.818	238
0.5	0.78	0.824	303
0.4	**0.78**	**0.835**	**355**
0.3	0.78	0.837	574
0.2	0.78	0.839	611
0.1	0.78	0.841	755

As it can be seen from the Table 2 the optimal value of the parameter a is 0.4 since it is resulted in final segmentation agreement of $ZSI_{\text{reshaped}} = 0.835$. Basically lower values of the 'a' should lead to better segmentation agreement results. Since for the smaller values of the a ($a < 0.4$) the reshaping

iterations increase dramatically at the same time the segmentation agreement rises slightly, regarding time efficiency, the optimal value of this parameter is set to $a = 0.4$.

To enable more precise comparison in contrast with another state of the art segmentation method, the dataset images are segmented further with a well-known method which is based on region growing followed by thresholding used in Adiga *et al.* (2006). Table 3 provides the segmentation results for both rectangular and reshaped levels of the proposed method contrasted with the results of the Adigas method.

Table 3. *The segmentation results of the proposed method in both rectangular and reshaped levels in contrast with Adiga's method. ($\overline{ZSI}$, $\overline{JSI}$: similarity indices, $\overline{EF}$, $\overline{MF}$: segmentation errors, time: processing time per image)*

Method	$\overline{ZSI}$	$\overline{JSI}$	$\overline{EF}$	$\overline{MF}$	*time*
Proposed rect	0.78	0.60	0.18	0.14	10.1
Proposed reshaped	0.83	0.67	0.09	0.18	301.4
Adiga's	0.78	0.56	0.15	0.13	7.03

Here, the $\overline{ZSI}$ and $\overline{JSI}$ are average similarity indices between segmented images and the ground-truth, the $\overline{EF}$ and $\overline{MF}$ are average segmentation errors and *time* shows the mean processing time per image in seconds.

As it can be seen from Table 3 the first two rows of the table represent the results of the proposed method in both rectangular and reshaped levels and the third row represents the results of the method used in Adiga *et al.* (2006). The average similarity index ($\overline{ZSI}$) of the mentioned method in the rectangular level (proposed rect) is 0.78 which significantly increased to 0.83 due to stochastic reshaping process. Similarly, the Jaccard's ($\overline{JSI}$) index increased from 0.6 to 0.67. The over segmentation error rate sank significantly by 0.09 (50%). However, there is a slight increase in under segmentation error rate.

The performance of the proposed method in rectangular level is almost the same with the Agida's methods. Whereas the proposed method in reshaped level outperforms the Agida's method considering both similarity and error indices. However, stochastic reshaping process needs more processing time to exactly delineate the borders of the target objects.

Fig. 9 depicts an example of the binary images that are used together for segmentation assessment of the methods including images produced by the proposed or Agida's method and the ground-truth.

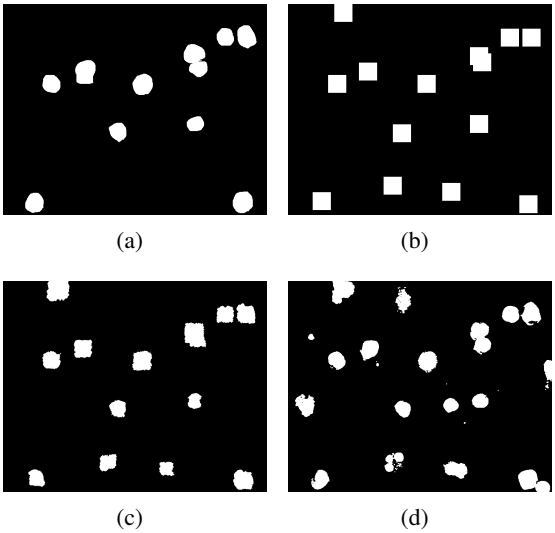

Fig. 9. *Examples of the binary images produced and used in the experiments. (a) A manually segmented ground truth, (b) A segmentation result of the proposed method in the rectangular detection step, (c) A segmentation result of the proposed method obtained from stochastic reshaping process, (d) A segmentation result of the region growing (Agida's) method used for comparison of the proposed method.*

Figs. 10 and 11 depict example images segmented by proposed and Agida's methods respectively. The target objects are identified with white dots inside and the final segmented objects borders are shown in yellow.

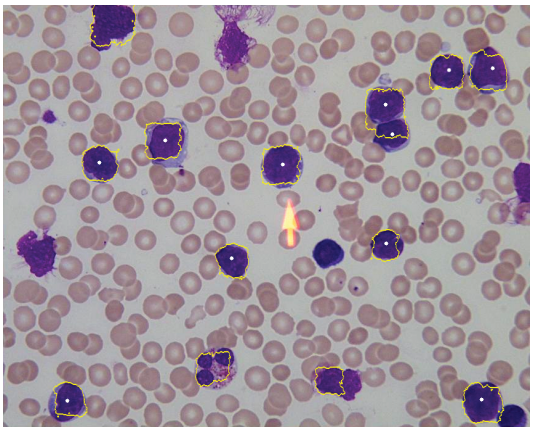

Fig. 10. *An example image segmented by proposed method. The target objects are labeled with white dots inside. The yellow contours represent method's segmentation output.*

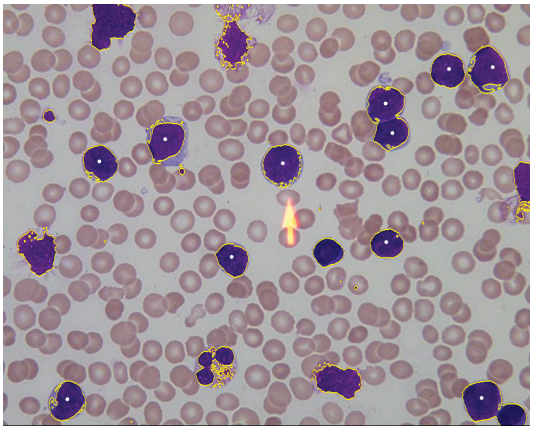

Fig. 11. *An example image segmented by region growing based (Agida's) method. The target objects are labeled with white dots inside. The yellow contours represent method's segmentation output.*

DISCUSSION

Existing bottom-up segmentation approaches like Al-Kofahi *et al.* (2010) which utilize low- or mid-level image features such as edges or gradient values, lead to poor segmentation results once applied to occluded and cluttered images (*i.e.*, images that contain complex spatial color patters). These methods are mostly unsupervised and may present acceptable time performance and skip training step. However, due to their ad-hoc nature, the edge- gradient based methods may fail even once they applied to rather similar subcategories of a specific image type. Furthermore, in real daily pathological routine, pathologists might be interested to a specific subgroup of the target objects for instance malignant cells or lymphoblasts in the case. This confirms the need for a flexible supervised method with the ability of being tuned and trained to specific categories of images.

To overcome the mentioned limitations, we proposed a supervised method which utilizes both low- and high level image features. Since the method utilizes content, shape and gradient information, it is robust enough to handle various subcategories of stained histocytology images. The processing pipeline of the method consisted of rectangular detection and segmentation components. The stochastic reshaping component could be optionally activated in the cases that there is a need for more precise delineation of the target objects. Unlike level set methods, the proposed method can handle segmentation of multiple regions on a single image. Another significant property of the method is that it can be adapted to various types of the histocytology images. The adaption could be carried out by adjusting weighting parameters related to the texture, shape and gradient terms of the proposed cost function (Eq. 8). For instance if there is no clear borders in an image dataset and the target objects are described mainly by their texture rather than other features, the gradient weighting parameter (η) should be set to a smaller value than the texture parameter (γ). However, finding the optimal combination of the parameters is a challenge that needs to be addressed by experiments.

The segmentation performance of the proposed method is compared with another state of the art method. Although both methods including the proposed one are not extremely precise, according to Table 3 the proposed method demonstrated statistically better segmentation performance than Agida's method. However, due to the unsupervised nature of the Agida's method it needs less processing time than the proposed method. The final segmentation performance of the proposed method is dependent to the initial rectangular detection. Although stochastic reshaping algorithm can converge to the object's borders in the cases of improper initialization, however it needs significant amount of processing time. Hence the proper initialization effects on both processing time and segmentation quality. The proposed method matched to the ground-truth with the average *ZSI* score of 0.83. According to Zijdenbos *et al.* (1994), it is generally accepted that a $ZSI > 0.7$ represents very good agreement. Therefore, the average agreement of the proposed method in reshaped level is appropriate. The prototype software developed based on the proposed method could be considered as a potential tool for pathologists in daily diagnostic routines and it could be also utilized in the research projects.

CONCLUSION

A new method is proposed for rectangular detection and segmentation of the immature cells found in peripheral blood (lymphoblasts). The method is robust enough to be tuned and applied to the other similar histocylogy images. It demonstrated appropriate level of detection accuracy (precision $=$ 0.94, recall $=$ 0.88) and segmentation agreement with the ground truth ($\overline{ZSI} = 0.83$). The prototype software developed based on the method could be considered as a potential CAD tool for diagnosis of the acute lymphoblastic leukemia in the clinical process. Moreover, it can be used by the researchers who are investigating the computer aided analysis of the histocytology images.

REFERENCES

Adiga U, Malladi R, Fernandez-Gonzalez R, de Solorzano C (2006). High-throughput analysis of multispectral images of breast cancer tissue. IEEE T Image Process 15(8):2259–68.

Ali S, Madabhushi A (2012). An integrated region-, boundary-, shape- based active contour for multiple object overlap resolution in histological imagery. IEEE Trans Med Imag 31(7):1448–60.

Al-Kofahi Y, Lassoued W, Lee W, Roysam B (2010). Improved automatic detection and segmentation of cell nuclei in histopathology images. IEEE Trans Biomed Eng 57:841–52.

Chan T, Vese L (2001). Active contours without edges. IEEE T Image Process 10(2):266–77.

Gurcan MN, Boucheron LE, Can A, Madabhushi A, Rajpoot NM, Yener B (2009). Histopathological image analysis: A review. IEEE Rev Biomed Eng 2:147–71.

Kass M, Witkin A, Terzopoulos D (1988). Snakes: Active contour models. INT J Comput Vision 1(4):321–31.

Korde VR, Bartels H, Barton J, Ranger MJ (2009). Automatic segmentation of cell nuclei in bladder and skin tissue for karyometric analysis. Anal Quant Cytol Histol 31(2):83–9.

Kovalev V, Dmitruk A, Safonau I, Frydman M, Shelkovich S (2011). A method for identification and visualization of histological image structures relevant to the cancer patient conditions. In: Real P, Diaz-Pernil D, Molina-Abril H, Berciano A, Kropatsch W, eds. Lect Not Comput Sci 6854:460–8.

Labati R, Piuri V, Scotti F (2011). All-idb: The acute lymphoblastic leukemia image database for image processing. In: Proc 18th IEEE Int Conf Image Process. Sep 11–14. Brussels, Belgium. 2045–8.

Li G, Liu T, Nie J, Guo L, Chen J, Zhu J, Xia W, Mara A, Holley S, Wong S (2008). Segmentation of touching cell nuclei using gradient flow tracking. J Microsc 231(1):47–58.

Mulrane L, Rexhepaj E, Penney S, Callanan JJ, Gallagher WM (2008). Automated image analysis in histopathology: a valuable tool in medical diagnostics. Expert Rev Mol Diagn 8:707–25.

Wang L, Shi J, Song G, Shen IF (2007). Object detection combining recognition and segmentation. In: Yagi Y, Kang S, Kweon I, Zha H, eds. Lect Not Comput Sci 4843:189-99.

Wienert S, Heim D, Saeger K, Stenzinger A, Beil M, Hufnagl P, Dietel M, Denkert C, Klauschen F (2012). Detection and segmentation of cell nuclei in virtual microscopy images: A minimum-model approach. Sci Rep 2:503.

Zijdenbos A, Dawant B, Margolin R, Palmer A (1994). Morphometric analysis of white matter lesions in mr images: method and validation. IEEE Trans Med Imag 13(4):716–24.

Image Anal Stereol 2013;32:101-105 doi:10.5566/ias.v32.p101-105
Original Research Paper

EXACT SIMULATION OF A BOOLEAN MODEL

CHRISTIAN LANTUÉJOUL✉

MinesParisTech, 35 rue Saint-Honoré, 77305 Fontainebleau, France
e-mail: christian.lantuejoul@mines-paristech.fr
(Received February 27, 2013; revised April 4, 2013; accepted May 5, 2013)

ABSTRACT

A Boolean model is a union of independent objects (compact random subsets) located at Poisson points. Two algorithms are proposed for simulating a Boolean model with non uniformly bounded objects in a bounded domain. The first one applies only to stationary models. It generates the objects prior to their Poisson locations. Two examples illustrate its applicability. The second algorithm applies to stationary and non-stationary models. It generates the Poisson points prior to the objects. Its practical difficulties of implementation are discussed. Both algorithms are based on importance sampling techniques, and the generated objects are weighted.

Keywords: Boolean model, importance sampling, Minkowsky functionals, Steiner formula.

INTRODUCTION

The Boolean model is certainly one of the most currently used random set models in mathematical morphology, stochastic geometry and spatial statistics. It is defined as the union of a family of independent random compact subsets (denoted for short as "objects") located at the points of a locally finite Poisson process. It is stationary if the objects are identically distributed (up to their location) and the Poisson process is homogeneous, and non-stationary otherwise.

Despite its widespread use, it seems that little attention has been paid to the following problem: How to perform *exact simulations* of a Boolean model in a bounded domain?

The solution to that problem is not straightforward, unless the objects are uniformly bounded. The difficulty lies in that the intersection of a Boolean model and a bounded domain is also a Boolean model, but its parameters are different. The more remote the object to the domain, the less chance they have to hit it. On the other hand, the larger the objects, the more chance they have to hit the domain.

After a brief reminder on the Boolean model, this problem is investigated. Although most emphasis is placed on the stationary case because of its possible connections with stereology, the general case is also treated in a second part of the paper. Two examples serve to illustrate the algorithms and their implementations.

Here is the set of notation that will be used throughout the paper. Unless specified, the workspace is the d-dimensional Euclidean space $\mathbb{R}^d$ with Lebesgue measure v_d. The origin of $\mathbb{R}^d$ is denoted by o. More generally, points are denoted by lower case letters, subsets by capital letters and family of subsets by calligraphic letters. If $x \in \mathbb{R}^d$ and $A \subset \mathbb{R}^d$, $\tau_x A$ stands for the translation of A w.r.t. vector $\vec{ox}$. The dilation of A by another subset B is defined as

$$\delta_B A = \{x \in \mathbb{R}^d : \tau_x B \cap A \neq \varnothing\} .$$

DEFINITION AND MAIN PROPERTIES

The basic ingredients of a Boolean model are

(i) a *Poisson point process* $\mathscr{P}$ with an intensity function $\theta = (\theta_x, x \in \mathbb{R}^d)$ that is assumed to be locally integrable.

(ii) a family of nonempty and *mutually independent compact random subsets* $(A_x, x \in \mathbb{R}^d)$. A_x is called the *object* located at x. If it takes simple shapes, then its statistical properties can be specified by elementary descriptors (e.g., distribution of its radius for a disk). For more intricate shapes, the hitting functional of A_x can be considered (Matheron, 1975). It assigns each compact subset K of $\mathbb{R}^d$ (in short $K \in \mathscr{K}$) the probability that it intersects with A_x,

$$T_x(K) = P\{A_x \cap K \neq \varnothing\} , \qquad K \in \mathscr{K} . \quad (1)$$

Definition 1 *A Boolean model is a union of objects located at Poisson points,*

$$X = \bigcup_{x \in \mathscr{P}} A_x .$$

Our objective is to simulate the Boolean model in a compact domain, say Z. Insofar as this mainly consists of simulating the objects of X that intersect with Z, it is crucial to assume their number to be almost surely finite. Under this assumption, it can be shown (Lantuéjoul, 2002) that the number of objects hitting any compact subset K of Z is Poisson distributed with mean

$$\vartheta(K) = \int_{\mathbb{R}^d} \theta_x T_x(K)\, \mathrm{d}x\,, \qquad K \in \mathscr{K}(Z)\,. \tag{2}$$

In particular, the avoiding functional of $X \cap Z$, defined for each $K \in \mathscr{K}(Z)$ as

$$Q_{X\cap Z}(K) = P\{(X \cap Z) \cap K = \varnothing\} = P\{X \cap K = \varnothing\}$$

is equal to

$$Q_{X\cap Z}(K) = \exp\bigl(-\vartheta(K)\bigr) \qquad K \in \mathscr{K}(Z)\,. \tag{3}$$

STATIONARY CASE

ALGORITHM

In this case, the intensity function is constant, say θ, and all objects have the same hitting functional, up to a translation

$$T_x(K) = T_o(\tau_{-x}K)\,. \tag{4}$$

In what follows, it is convenient to write

$$T_o(K) = \int_{\mathscr{K}} \mathrm{d}F(A)\, 1_{A\cap K\neq\varnothing}\,,$$

where F (symbolically) denotes the distribution of the parameters of A_o. Then we have

$$T_x(K) = \int_{\mathscr{K}} \mathrm{d}F(A)\, 1_{\tau_x A\cap K\neq\varnothing}\,.$$

Applying this formula to Eq. 2 and permuting integrals, the mean number of objects hitting Z becomes

$$\vartheta(Z) = \theta \int_{\mathscr{K}} \mathrm{d}F(A) v_d\bigl(\delta_A Z\bigr) = \theta E\bigl\{v_d\bigl(\delta_A Z\bigr)\bigr\}, \tag{5}$$

which gives the following expression for the avoiding functional of $X \cap Z$.

$$Q_{X\cap Z}(K) = \exp\left(-\theta \int_{\mathscr{K}} \mathrm{d}F(A) v_d\bigl(\delta_A K\bigr)\right)\,.$$

Let us write it slightly differently

$$Q_{X\cap Z}(K) = \exp\left(-\vartheta(Z) \int_{\mathscr{K}} \mathrm{d}F^Z(A)\, \frac{v_d(\delta_A K)}{v_d(\delta_A Z)}\right), \tag{6}$$

which involves a weighted version F^Z of F

$$\mathrm{d}F^Z(A) = \frac{\mathrm{d}F(A) v_d(\delta_A Z)}{E\{v_d(\delta_A Z)\}}\,. \tag{7}$$

An interpretation of Eq. (6) is as follows: $X \cap Z$ is the union of a Poisson number (mean $\vartheta(Z)$) of independent objects of the form $\tau_{\dot{x}}A$ where A is distributed like F^Z and $\dot{x}$ is a uniform point over $\delta_A Z$. Hence the simulation algorithm:

Algorithm 1

(i) set $X = \varnothing$*;*

(ii) generate $n \sim \mathscr{P}\bigl(\vartheta(Z)\bigr)$*;*

(iii) if $n = 0$*, return* $X \cap Z$ *and stop;*

(iv) generate $A \sim dF^Z$*;*

(v) generate $x \sim \mathscr{U}(\delta_A Z)$*;*

(vi) put $X = X \cup \tau_x A$*,* $n = n-1$ *and goto (iii).*

The main difficulty with this algorithm is step *(iv)*: How to simulate the weighted distribution $\mathrm{d}F^Z$? The next section shows that interesting simplifications arise when the objects are convex.

CONVEX OBJECTS

Such algorithmic simplifications actually arise only when the simulations are performed within a ball-shaped domain. Accordingly, it is advantageous to firstly extend the simulation field to a ball, then perform the simulations in the extended domain, and finally restrict the simulations produced to the actual simulation field. The choice of the ball is unimportant, as long as it encloses the simulation field. One possibility is the ball circumscribed to the simulation field.

In what follows, the simulation field Z is assumed to be a ball, say $B(o,\rho)$. Then Steiner formula applies and shows that the mean number of objects hitting Z depends only on the expected Minkowski functionals of the objects:

$$\vartheta(Z) = \theta \sum_{k=0}^{d} \binom{d}{k} E\{W_k(A)\}\rho^k. \tag{8}$$

Moreover, dF^Z can be simulated as a mixture of distributions of objects weighted by their Minkowski functionals:

$$\begin{aligned}\mathrm{d}F^Z(A) &= \mathrm{d}F(A)\frac{\sum_{k=0}^d \binom{d}{k} W_k(A)\rho^k}{\sum_{k=0}^d \binom{d}{k} E\{W_k(A)\}\rho^k} \\ &= \sum_{k=0}^{d} p_k\, \mathrm{d}F_k(A)\,,\end{aligned}$$

with

$$\mathrm{d}F_k(A) = \frac{\mathrm{d}F(A)W_k(A)}{E\{W_k(A)\}} \qquad k = 0, ..., d, \qquad (9)$$

and

$$p_k = \frac{\binom{d}{k} E\{W_k(A)\}\rho^k}{\sum_{l=0}^{d} \binom{d}{l} E\{W_l(A)\}\rho^l} \qquad k = 0, ..., d. \qquad (10)$$

Using this mixture of weighted distributions, the algorithm for simulating dF^Z becomes

Algorithm 2

(i) generate $k \sim p$;

(ii) generate $A \sim dF_k(A)$;

(iii) return A and stop.

The following two examples show how this algorithm can be implemented.

Example 1

The objects are balls and their radii follow independent exponential distributions with mean $1/a$

$$P\{R > r\} = \exp(-ar) \, .$$

Starting from Eq. 5, the mean number of objects hitting Z is

$$\vartheta(Z) = \theta E\left\{\omega_d(\rho + R)^d\right\} = \frac{\theta d! \omega_d}{a^d} \sum_{k=0}^{d} \frac{(a\rho)^k}{k!} \, ,$$

where $\omega_d = \pi^{d/2}/\Gamma(d/2+1)$ is the d-volume of the unit ball.

The next step is the simulation of $dF_k(A)$. Actually, it can also be written $dF_k(r)$ because the only random element of A is its radius. If $A = B(o,r)$, then $W_k(A) = \omega_d r^{d-k}$ and $E\{W_k(A)\} = \omega_d (d-k)!/a^{d-k}$. Plugging these values into Eq. 9, we obtain

$$\mathrm{d}F_k(r) = \frac{a \exp(-ar)(ar)^{d-k}}{(d-k)!} \, .$$

This is a gamma distribution with parameter $d-k+1$ and scale factor a. A simple way to simulate it is to consider $-\ln(u_1 \cdots u_{d-k+1})/a$ where $u_1, ..., u_{d-k+1}$ are independent uniform values on $]0,1[$.

As an illustration, Fig. 1 shows a simulation of a Boolean model of discs with exponential radii. The displayed simulation field is a 7×5 rectangle. The Poisson intensity is $\theta = 10$ and the parameter a of the exponential distribution has been chosen equal to 7.22 so as to provide a background proportion of 30%.

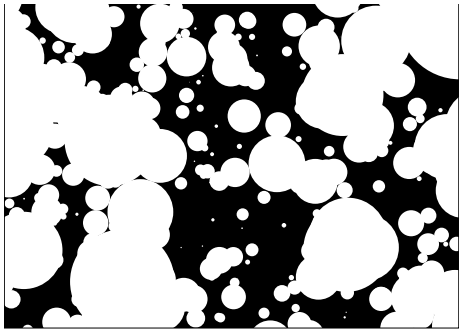

Fig. 1. *Simulation of a Boolean model of discs with exponential radii.*

Example 2

Here is a somewhat more elaborate example, even if the Boolean model considered is only two-dimensional. The objects are typical Poisson polygons derived from a network of Poisson lines with intensity λ, see Fig. 2.

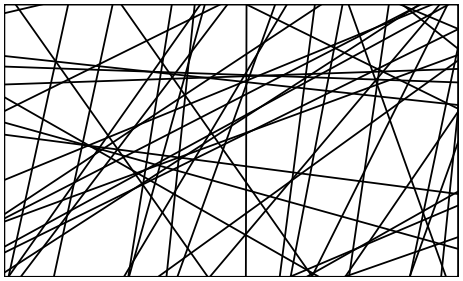

Fig. 2. *Realization of a Poisson line process. The polygons delimited by the lines are Poisson polygons.*

These polygons have been extensively studied in Miles (1969) and Matheron (1975). In particular their expected Minkowski functionals are

$$E\{W_0(A)\} = \frac{1}{\pi\lambda^2} \;\; E\{W_1(A)\} = \frac{1}{\lambda} \;\; E\{W_2(A)\} = \pi \, .$$

Using these expected values, Eq. (8) gives

$$\vartheta(Z) = \frac{\theta}{\pi\lambda^2}(1 + \pi\lambda\rho)^2 \, .$$

Not so simple is the simulation of $\mathrm{d}F^Z(A) = p_0 F_0(A) + p_1 F_1(A) + p_2 F_2(A)$. The explicit values for the weights are

$$p_0 = \frac{1}{(1+\pi\lambda\rho)^2} \, , \qquad p_1 = \frac{2\pi\lambda\rho}{(1+\pi\lambda\rho)^2} \, ,$$

$$p_2 = \frac{\pi^2\lambda^2\rho^2}{(1+\pi\lambda\rho)^2} \, .$$

With probability p_0, a polygon must be simulated from F_0. The standard procedure to do this consists of generating Poisson lines sequentially by increasing

distance from the origin. The procedure is continued until the generation of additional lines no longer affects the polygon containing the origin.

With probability p_1 a polygon must be simulated from F_1. To do this, a polygon is first generated from F_0, and then split by a uniformly oriented line through the origin. It remains to select at random one of the two polygons thus delimited (see Fig. 3).

With probability p_2 a polygon must be simulated from F_2. The algorithm proposed by Miles (1974) consists of taking the intersection between a polygon generated from F_0 and a cone delimited by two random rays emanating from the origin (see Fig. 3). Both rays are uniformly oriented and separated by an angle with p.d.f. $f(\varphi) = \varphi \sin\varphi/\pi$.

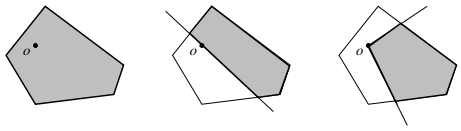

Fig. 3. *Weighted polygons generated from distributions F_0 (left), F_1 (middle) and F_2 (right).*

To illustrate the construction, a simulation of a Boolean model of Poisson polygons is depicted in Fig. 4. With a Poisson intensity θ and a Poisson line intensity λ respectively set to 10 and 1.625, the background proportion is close to 30%.

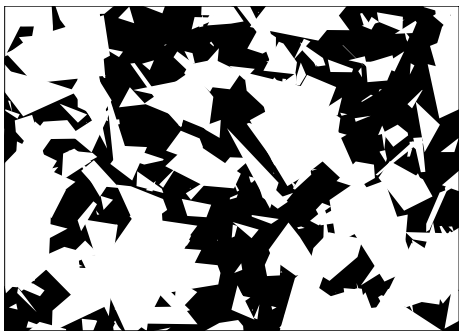

Fig. 4. *Simulation of a Boolean model of Poisson polygons.*

NON STATIONARY CASE

ALGORITHM

Let us start again with Eq. 3 that provides the avoiding functional of $X \cap Z$, and let us write it like

$$Q_{X\cap Z}(K) = \exp\left(-\vartheta(Z)\frac{\vartheta(K)}{\vartheta(Z)}\right) ,$$

provided that $\vartheta(Z) > 0$ (if $\vartheta(Z) = 0$, then $X \cap Z = \varnothing$ a.s.). On the other hand, Eq. 2 can be used to derive the following expansion

$$\frac{\vartheta(K)}{\vartheta(Z)} = \int_{\mathbb{R}^d} \frac{\theta_x T_x(Z)}{\vartheta(Z)} \frac{T_x(K)}{T_x(Z)}\, \mathrm{d}x ,$$

which shows that $\vartheta(K)/\vartheta(Z)$ is the hitting functional of some object of Z, say A^Z. More precisely, A^Z is located according to the pdf

$$f(x) = \frac{\theta_x T_x(Z)}{\vartheta(Z)} , \qquad x \in \mathbb{R}^d . \tag{11}$$

Moreover, the conditional hitting functional of A^Z given its location x is equal to

$$\frac{T_x(K)}{T_x(Z)} = P\{(A_x \cap Z) \cap K \neq \varnothing \mid A_x \cap Z \neq \varnothing\} . \tag{12}$$

A^Z is called a *typical object hitting Z*.

The interest of typical objects lies in the following property (Lantuéjoul, 2002):

Proposition 1 *$X \cap Z$ is the union of a Poisson number (mean $\vartheta(Z)$) of typical objects hitting Z.*

Indeed, we can readily check that the avoiding functional of such a union of typical objects coincides with that of $X \cap Z$:

$$\sum_{n=0}^{\infty} \exp\big(-\vartheta(Z)\big) \frac{\vartheta^n(Z)}{n!} \left(1 - \frac{\vartheta(K)}{\vartheta(Z)}\right)^n = \exp\big(-\vartheta(K)\big) .$$

From this proposition, the following algorithm is derived for simulating a Boolean model, even non stationary, in the domain Z.

Algorithm 3

(i) set $X = \varnothing$;

(ii) generate $n \sim \mathscr{P}\big(\vartheta(Z)\big)$;

(iii) if $n = 0$, return X and stop;

(iv) generate a typical object A^Z hitting Z;

(v) put $X = X \cup A^Z$, $n = n - 1$ and goto (iii).

PRACTICAL IMPLEMENTATION

Algorithm 3 calls for several remarks. Step *(ii)* assumes that $\vartheta(Z)$ is explicitly known, but this is not always the case because the integral of $\theta_x T_x(Z)$ may not be mathematically tractable. Moreover, step *(iv)* requires simulating the pdf (Eq. 11) that specifies the location of the typical objects hitting Z. This distribution may have a complicated expression. Step *(iv)* also involves generating conditionally typical objects given their locations. It is possible to generate objects A_x sequentially till one is produced that hits Z. This algorithm can be easily implemented but lacks efficiency.

In order to alleviate these difficulties, rejection and coupling methods can be resorted to. A typical approach is to consider another Boolean model X' that *dominates* X, in the sense that its ingredients satisfy the following three properties:

(i) its Poisson intensity function θ' satisfies $\theta'_x \geq \theta_x$ (at each point x)

(ii) its population of objects (A'_x) satisfies $A'_x \supset A_x$

(iii) there exists an algorithm to conditionally simulate A_x given A'_x.

Then the idea is firstly to generate the objects of X' hitting Z. Then each generated object A'_x is saved with probability θ_x/θ'_x and discarded with the complementary probability $1 - \theta_x/\theta'_x$. Finally, each remaining object A'_x is replaced by a new object A_x generated using the conditional algorithm mentioned in (iii). A simulation of X in Z is given by the union of these new objects in Z.

Hence, a Boolean model can effectively be generated whenever it is dominated by another Boolean model that is numerically tractable and can be simulated. There is no general rule for building such a dominating model. This must be done on a case by case basis.

ACKNOWLEDGEMENTS

The topic of this paper was presented at the S4G Conference, June 25-28, 2012 in Prague, Czech Republic. The author thanks P. Calka for fruitful discussions about the simulation of weighted Poisson polygons.

REFERENCES

Lantuéjoul C (2002). Geostatistical simulations: Models and algorithms. Berlin: Springer.

Matheron G (1975). Random sets and integral geometry. New York: Wiley.

Miles RE (1969). Poisson flats in Euclidean spaces. Adv Appl Prob 1:211-37.

Miles RE (1974). A synopsis of Poisson flats in Euclidean spaces. In: Harding EF, Kendall DG, eds. Stochastic geometry. New York: Wiley. pp. 202–27.

Image Anal Stereol 2013;32:107-115 doi:10.5566/ias.v32.p107-115
Original Research Paper

3D RECONSTRUCTION AND ANALYSIS OF THE FRAGMENTED GRAINS IN A COMPOSITE MATERIAL

LUC GILLIBERT✉ AND DOMINIQUE JEULIN

Centre de Morphologie Mathématique, Mathématiques et Sytèmes, Mines ParisTech, 35, rue Saint Honoré, 77305 Fontainebleau, France
e-mail: luc.gillibert@cmm.ensmp.fr, dominique.jeulin@cmm.ensmp.fr
(Received June 6, 2012; revised May 20, 2013; accepted June 9, 2013)

ABSTRACT

X-ray microtomography from solid propellant allows studying the microstructure of fragmented grains in damaged samples. A new reconstruction algorithm of fragmented grains for 3D images is introduced. Based on a watershed transform of a morphological closing of the input image, the algorithm can be used with different sets of markers. Two of them are compared. After the grain reconstruction, a multiscale segmentation algorithm is used to extract each fragment of the damaged grains. This allows an original quantitative study of the fragmentation of each grain in 3D. Experimental results on X-ray microtomographic images of a solid propellant fragmented under compression are presented and validated.

Keywords: clustering, damage, mathematical morphology, reconstruction, segmentation, solid propellant.

INTRODUCTION

Propellants are composite materials made of linear elastic brittle grains embedded in a visco-elastic elastomer matrix. Damage can occur in the brittle grains of solid propellants under the action of a mechanical shock, inducing a possible unsafe behavior of the propellant. In order to characterize the progression of damage in such composite materials, it is interesting to analyze their microstructure at different steps of the fragmentation, as initiated in Gillibert and Jeulin (2011a).

In the present paper, specimens of this material were fragmented under compression generated by the impact of a mass, and examined by means of microtomographic images obtained on a high-resolution micro-CT system. From these 3D images, the goal is to estimate some statistics on each grain, that should be relevant to the progression of the 3D damage: the specific surface area of its cracks, the volume fraction of its cracks, the number of fragments and the size distribution of its fragments. For this purpose, original grains have to be reconstructed from the image of the fragmented material. Then, each fragment must be extracted, and must be associated to its initial grain.

In this paper, we first introduce the type of materials and of 3D images that are studied. Then the original algorithm for the reconstruction of the particles from the observed fragmented image, based on two types of segmentation (one based on the h-minima, and one using the K-means clustering algorithm) is presented. Then a multiscale segmentation based on the stochastic watershed gives a 3D images of individual fragments. Finally, 3D image analysis measurements provide a statistical analysis of the local damage in the material, which gives a new approach to the local 3D study of damage in materials. The steps of our approach are illustrated by Fig. 1.

MATERIALS AND 3D IMAGES

The studied images are obtained by X-ray microtomography with a Skyscan 1172 high-resolution micro-CT system at the CEA Gramat, a public laboratory affiliated with the Atomic Energy and Alternative Energies Commission. The material samples are a solid propellant in three states: the initial material, and fragmented materials with two steps of degradation generated by mechanical impacts. For all the studied images, a voxel is 3.6 µm. The original diameter of the grains is 400 µm, but there are many small fragments in the damaged specimens.

The following images ares studied:

- MAT1 is a $1014 \times 1155 \times 250$ voxels image ($3650.4 \times 4158 \times 900$ µm^3). A slice of this image is illustrated in Fig. 2. A mechanical impact is obtained from a 2 kg mass falling 15 cm.
- MAT2 is a $1035 \times 1008 \times 428$ voxels image ($3726 \times 3628.8 \times 1540.8$ µm^3). It is a reference material without any mechanical impact (Fig. 3). However it contains some rare cracks.
- MAT3 is a $1116 \times 1104 \times 424$ voxels image ($4017.6 \times 3974.4 \times 1526.4$ µm^3). A mechanical

impact is obtained from a 2 kg mass falling 30 cm, with a 9.5 cm rebound (Fig. 4).

Measuring the evolution of local damage in such materials is a challenge, requiring to extract the crack network in grains for their individual study. As seen in Fig. 2 and Fig. 4, the crack network is complex and many grains are highly fragmented, so that it is not easy to recover the initial grains from the image. The purpose of the algorithms developed in this paper is to give a reliable and automatic method to provide local estimates of the damage.

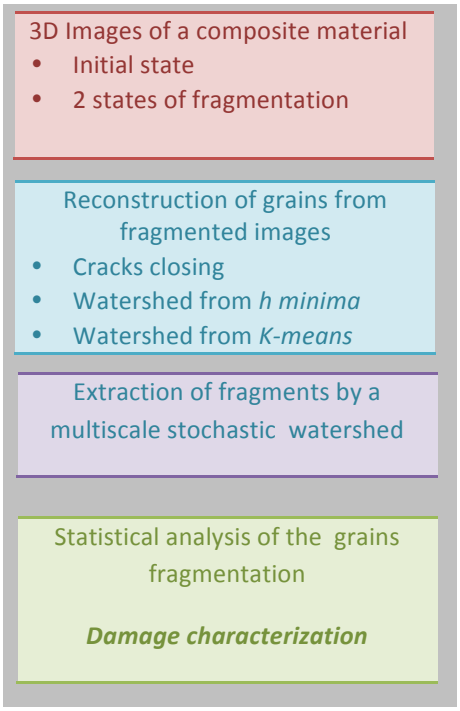

Fig. 1. *Flowchart of the study of fragmented media.*

RECONSTRUCTION ALGORITHM OF THE FRAGMENTED GRAINS

A classical approach is used for removing the cracks: morphological closing and a volumic opening removing connected components of the holes with a low volume (Matheron, 1967; Serra, 1982). Then, a watershed transform on the closed image is used. Introduced in 1979 by S. Beucher, the watershed is computed from a gradient image, here the inverse of the distance map of the closed image, and from a set of markers (Beucher and Lantuéjoul, 1979).

Two possible sets of markers for this watershed are explored.

The first approach is topological and uses the h-minima filter (Soille, 2003). The minima of the inverse distance function with a depth is larger than h are used as a sets of markers. The use of the h-minima with the watershed on the distance map is very classical, but if the grains are very fragmented and if the fragments are scattered, the algorithm fails to reconstruct correctly some grains.

The second approach is based on a method of cluster analysis, the K-means clustering, which aims to partition a set of observations into K clusters (Lloyd, 1982). Here, the observations are random voxels inside the mask of the grains. The kernels of the clusters, more precisely the center of gravity of the clusters, are used as sets of markers for the watershed.

The number of classes for the K-means clustering algorithm is automatically computed from the initial image with a covariance-based approach. The algorithm is described in Faessel and Jeulin (2010): the authors use the covariance for estimating the average radius of the grains, and then estimate the number of grains in the image.

CLOSING OF THE CRACKS

The studied solid propellant has two phases: grains and matrix. Therefore, the first step of the reconstruction is to compute a binary mask for the grains. The threshold is estimated via the maximization of the interclass variance (Otsu, 1979).

After the binarization, a morphological closing of the binary mask is used. The structuring element is a rhombicuboctahedron of radius 3, providing a good approximation of a sphere of small size on the digitized image. It offers a good compromise between performance and exactness. The size of the structuring element used is the same for the three images but depends on a subjective choice that is checked by visual inspection. Results with a rhombicuboctahedron of radius of radius 2 are also acceptable, but will lead to a few additional errors in the final reconstruction (the over-segmentation of a few grains).

The remaining holes inside closed grains are removed with a volumic opening: all the connected components of the matrix with a small volume are removed. The threshold on the volume is the same for the three images but also depends on a subjective choice. This threshold is fixed to 113 voxels (corresponding to a sphere of radius 3). Results with a threshold corresponding to a sphere of radius 4 or 5 are also acceptable, but will lead to a few additional errors in the final reconstruction, generating the fusion of a few grains.

The results of this first part of the segmentation are illustrated in Fig. 2 and Fig. 5.

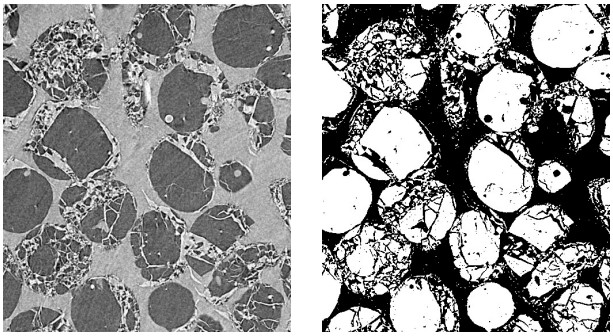

(A) (B)

Fig. 2. *(A) 3D X-ray microtomographic image of a fragmented granular material (slice). (B) Binarization by maximization of the interclass variance (slice).*

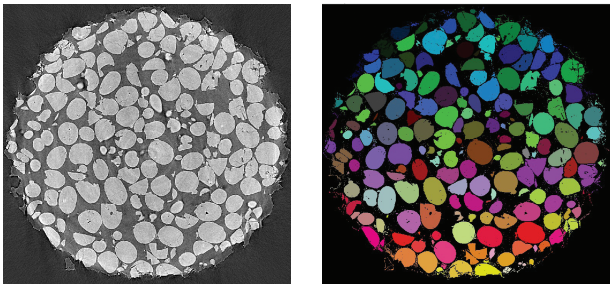

(A) (B)

Fig. 3. *(A) Original image for MAT2, the reference material without any mechanical impact (slice). (B) Watershed segmentation using markers computed from the h-minima (slice).*

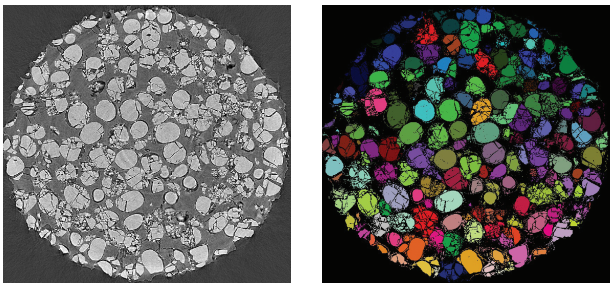

(A) (B)

Fig. 4. *(A) Original image for MAT3. An impact is obtained from a* 2 *kg mass falling* 30 *cm (slice). (B) Watershed segmentation using markers computed from the h-minima (slice).*

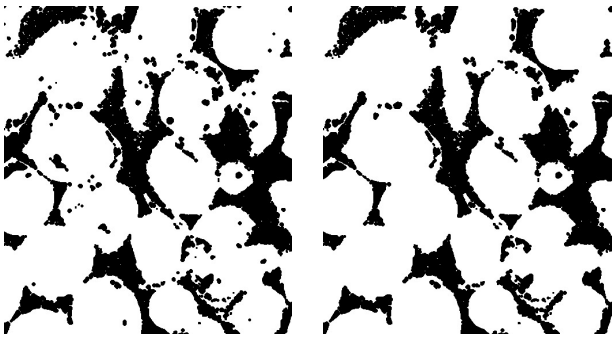

(A) (B)

Fig. 5. *(A) Morphological closing of the binary mask with a small rhombicuboctahedron (slice). (B) Removal of the holes with a volumic filter (slice).*

WATERSHED COMPUTED FROM THE MINIMA

A first segmentation to reconstruct the grains is provided by markers on selected minima of the distance map.

From the morphologically closed image, constructed in the section *Closing of the cracks*, a distance map is computed. Then, the inverse of this distance map is segmented with a watershed transform. The use of the local minima of the distance map will lead to an over-segmentation. Therefore, a prior *h*-minima transform is used on the distance map.

The *h*-minima transform suppresses all minima whose depth is less than *h*, reducing the number of local minima. The difficulty is in the choice of *h*. Using a trial and error approach and a visual inspection, it is possible to achieve a good reconstruction (Fig. 6A).

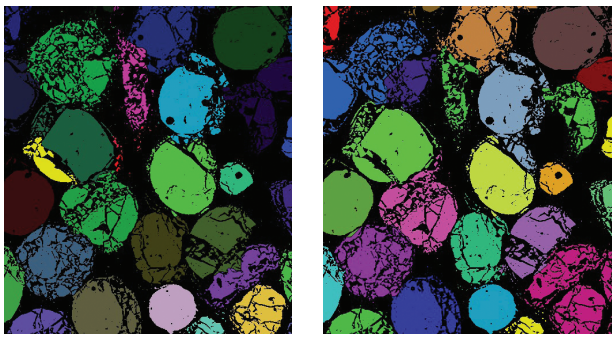

(A) (B)

Fig. 6. *(A) Watershed segmentation of the closed image after a h-minima filter (slice). (B) Watershed segmentation using markers computed from the K-means (slice).*

MARKERS COMPUTED FROM THE *K*-MEANS

For comparison, an alternative segmentation for the reconstruction of grains is obtained from markers generated by the K-means clustering algorithm.

A realization of Poisson point process is generated inside the binary mask of the image, with a low intensity. This gives a set of voxels used for a K-means clustering (Lloyd, 1982).

Given a set of voxels $\{p_1, p_2, \ldots, p_n\}$, K-means clustering aims to partition the n voxels into $K \leq n$ clusters, $\{S_1, S_2, \ldots, S_K\}$ so as to minimize the following sum of squares in each cluster: $\sum_{i=1}^{K} \sum_{p_j \in S_i} \left\| p_j - \mu_i \right\|^2$, where μ_i is the center of mass of voxels in the cluster S_i (assuming all the voxels have the same mass).

There exists several algorithms for building the set of clusters minimizing this sum. Here, the MacQueen algorithm, as implemented in the software R, is used (MacQueen, 1967).

The centers of mass μ_i are finally used as markers for the watershed transform on the distance map of the morphologically closed image constructed in the section *Closing of the cracks*.

The numbers K of classes used is directly estimated from the closed image. Considering for simplification the closed image as a realization of a Boolean model of spheres with a single radius R, it is deduced from the range of the covariance $C(h)$ equal to $2R$ (Faessel and Jeulin, 2010), obtained by the distance h for which $C(h) = V_v^2$. Then, the number of grains is deduced from this radius and from the Boolean model assumption (Jeulin, 1991): the volume fraction of the overlapping grains V_v is expressed as a function of the average number of grains per unit volume θ, by: $V_v = 1 - \exp(-\theta \frac{4}{3} \pi R^3)$.θ and consequently the total number of grains (and of markers) is deduced from V_v and R^3.

The same covariance-based approach, applied on the original thresholded image, before the morphological closing, gives an estimation of the size of the fragments. From this estimation, the intensity of the Poisson point process used for the clustering algorithm is deduced. The intensity is chosen such that each fragments receives at least several points.

The process achieves a satisfactory reconstruction of the grains, as illustrated in Fig. 6B.

MULTISCALE IMAGE SEGMENTATION

In this section, the goal is to isolate each fragment of each grain, for further morphological analysis. For the separation of the fragments, a multiscale stochastic watershed algorithm is used. The stochastic watershed segmentation was first introduced in Angulo and Jeulin (2007). The approach is based on using a large number of realizations of random markers to build a probability density function (pdf) of contours, starting from a standard watershed algorithm producing oversegmentation.

The stochastic watershed was proved to be efficient for unsupervised segmentation (Noyel *et al.*, 2007; Faessel and Jeulin, 2010). For multiscale images, the full granulometry of the image is used Gillibert and Jeulin (2011b). Using morphological openings, this granulometry can be automatically computed from the image and is used as a constraint during iterations of segmentation steps.

STOCHASTIC WATERSHED

The aim of the stochastic watershed Angulo and Jeulin (2007) is to estimate for each point of the contours of a standard watershed a probability (called here probability density function of contours) of detection from random markers.

The first method introduced for computing the stochastic watershed is based on a large number of realizations of random markers to estimate a probability density function of contours, or of surface boundaries in 3D. The random markers are generated with a uniform distribution of their coordiantes. For the present composite material, a constant background marker is added to each set of random markers. This constant background marker is extracted by thresholding the image via the maximization of the interclass variance.

For each set of markers, a constrained watershed transform is computed. Then, the Parzen window method (typically here a convolution of the probability image by a Gaussian kernel) is used to estimate the probability density function of contours from this finite set of random realizations (Parzen, 1962).

A good estimation of the probability of contours generated by the stochastic watershed requires 100 to 200 realizations (Angulo and Jeulin, 2007). However, using λ-flat zones to smoothen the local probability of contours, a stochastic watershed segmentation can be achieved with only 50 realizations (Faessel and Jeulin, 2010).

Computing a large number of watershed transforms from simulations provides good results but is a slow process, mainly in $3D$. A more efficient solution for computing stochastic watersheds is to use a graph-based approach. Probability of boundaries is directly computed with a good approximation without the use of any realization (Jeulin, 2008).

As an example, the computation of the stochastic watershed with 50 realizations of watershed transforms takes 163 minutes and 20 seconds for the MAT2 sample on 3.00 GHz Pentium 4. A similar result can be achieved in 7 minutes an 8 seconds, on the same computer, using the graph-based approach.

In Stawiaski and Meyer (2010) and Gillibert and Jeulin (2011b), the direct computation of the probability of the boundaries is obtained using a region adjacency graph deduced from the watershed, each vertex of the graph figuring a basin of attraction of the watershed, and each edge connecting two neigbouring basins. This graph-based approach leads to a multiscale stochastic watershed algorithm that is used now.

MULTISCALE STOCHASTIC WATERSHED

The main drawback of the stochastic watershed is that it is not well suited for the segmentation of objects with a wide range of scale. A variant was introduced by the authors to operate on a wide granulometric spectrum Gillibert and Jeulin (2011b). The multiscale image segmentation process is based on a simple idea: estimate the full granulometry of the image, using morphological openings, then use multiple stochastic watersheds with different numbers of markers for each size, and finally combine them to get a segmentation that is correct for each size of grains (no oversegmentation for big grains, no undersegmentation for small grains).

Many hierarchical segmentation algorithms were studied, such as the waterfalls (Beucher, 1994) or the P algorithm (Beucher and Marcotegui, 2009). Here the approach is based on the merging of the watersheds basins using a minimum spanning tree (Eppstein, 2000). In the merging process, a constraint is introduced: the granulometry of the image. The algorithm is described in Fig. 7.

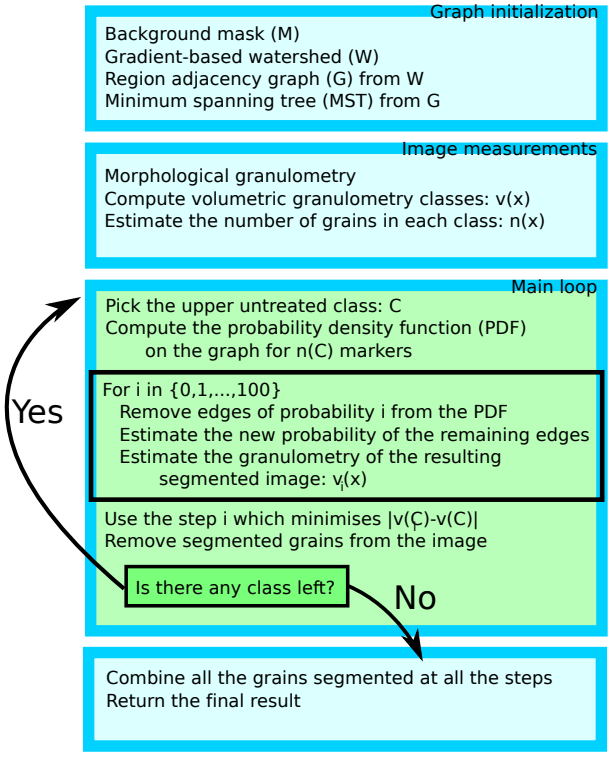

Fig. 7. *The main steps of the multiscale image segmentation process.*

The first step of the approach is to estimate the granulometry of the image, using morphological openings. From the granulometry, a small number of classes are chosen (3 classes in this paper). A good approach for this choice is to maximize the interclass variance. The total volume of the grains in each class x will be denoted $v(x)$. The number of grains in each class x is deduced from $v(x)$ and is denoted $n(x)$. It is used to generate the corresponding number of markers in the calculation of the probability of the boundaries between grains of the segmentation.

Then, the standard watershed transform is computed from the local minima of the gradient. From this watershed, the adjacency graph is constructed and a minimum spanning tree is extracted.

The first class is chosen, starting from the largest grains. The stochastic watershed is computed with a number of markers equals to $n(1)$. Based on this stochastic watershed, a first hierarchy on boundaries is computed with the merging algorithm. For each step i of the hierarchy, the granulometry of the corresponding segmentation is computed ($v_i(1)$).

In the full hierarchy, there is a size step which minimizes the difference $|v_i(1) - v(1)|$. This step is used for the segmentation of the grains in the first class. All the segmented grains are removed from the image and added to the background mask. The minimum spanning tree is updated and the next class is chosen.

The same process is applied to all the classes. When no more class is left, all the segmentations are combined together. Results are illustrated in Fig. 8. A few fragments are missing, and a few grains are oversegmented, but this errors have a small impact on the results of the measurements.

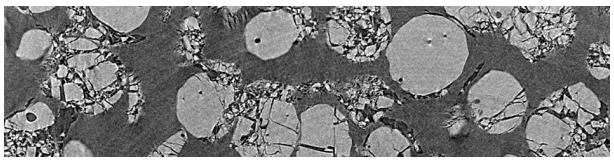

(A)

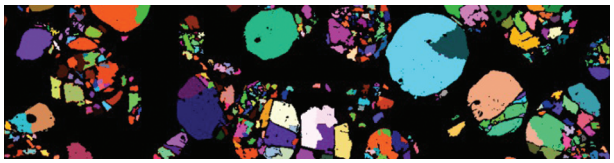

(B)

Fig. 8. *(A) Original image before multiscale segmentation (slice). (B) Final multiscale stochastic watershed segmentation (slice).*

IMAGE ANALYSIS AND MEASUREMENTS

VOLUME FRACTION AND SPECIFIC SURFACE AREA OF DAMAGED GRAINS

From the reconstructed data, the volume fraction of each grain is estimated before and after the morphological closing. From this two measurement, the volume fraction of the cracks of each grain is estimated.

For each image, grains reconstructed with the h-minima markers and grains reconstructed with the K-means markers are studied for comparison. The results for the volume fraction of the cracks, presented as normalized histograms (namely the proportion of grains in % with a given property), are shown in Figs. 9, 10 and 11. The agreement between the K-means reconstruction results and the h-minima reconstruction results is excellent, showing the robustness of our segmentations for the purpose of damage measurement.

With the number of intercepts (transitions from background to foreground) in 13 directions generated by a voxel and its first and second neighbours on the cubic grid, it is possible to estimate the surface area of each grain i from the closed reconstructed data (denoted $S_c(i)$). With the same process, the surface area of each grain before the morphological closing is estimated (denoted $S_f(i)$). From this two measurement, the surface area $S(i)$ of the cracks of each grain is estimated:

$$S(i) = S_f(i) - S_c(i) \; .$$

Due to some imperfections on the original grains, the surface area estimated with this process correspond to the surface area of the cracks, the small irregularities at the surface of the grains and the porosity.

The specific surface area S_{spec} measures the total surface area per unit of volume:

$$S_{\text{spec}}(i) = \frac{S(i)}{V(i)} \; .$$

The results for the specific surface area, presented as a normalized histogram, are shown in Fig. 12, Figs 13 and 14. Once again, the agreement between the K-means reconstruction results and the h-minima reconstruction results is excellent.

The damage on the grains is quantified from both specific surface area and volume fraction. On the sample MAT2, the reference material without any mechanical impact, the volume fraction of the cracks is low (mostly between 0 and 0.2) and the volume fraction is almost always 0. On the sample MAT3, impacted with a 2 kg mass falling 30 cm, with a 9.5 cm rebound, there is only 6% of the grains with a zero specific surface area of the cracks, and the volume fraction of the cracks is mostly between 0.2 and 0.5.

The sample MAT1, impacted with a 2 kg mass falling 15 cm, is less damaged than the sample MAT3. This is visible on both specific surface area and volume fraction. On the sample MAT1 there is only 8% of the grains with a zero specific surface area of the cracks, and the volume fraction of the cracks is mostly between 0.1 and 0.4.

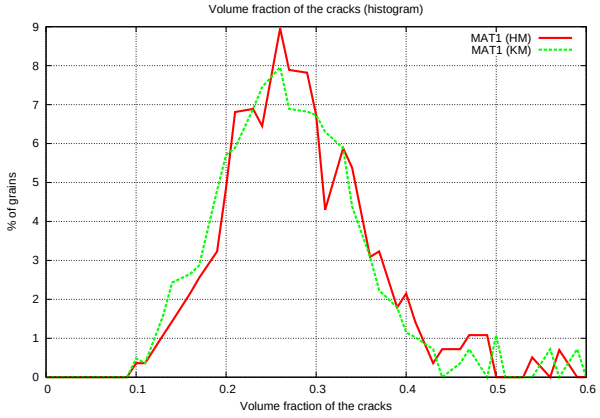

Fig. 9. *Histogram of the volume fraction of the cracks for MAT1. HM are the grains reconstructed with the h-minima markers and KM are the grains reconstructed with the K-means markers.*

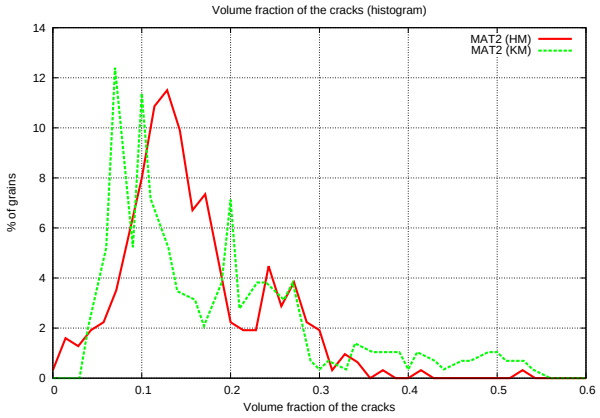

Fig. 10. *Histogram of the volume fraction of the cracks for MAT2. HM are the grains reconstructed with the h-minima markers and KM are the grains reconstructed with the K-means markers.*

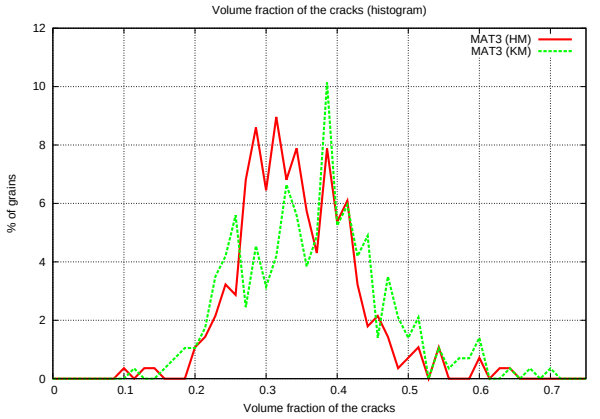

Fig. 11. *Histogram of the volume fraction of the cracks for MAT3. HM are the grains reconstructed with the h-minima markers and KM are the grains reconstructed with the K-means markers.*

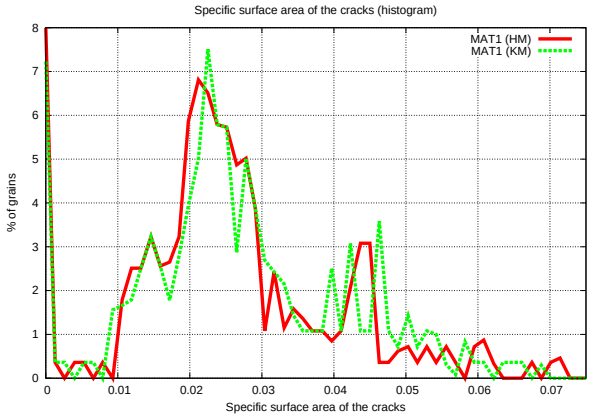

Fig. 12. *Histogram of the specific surface area of the cracks for MAT1 (given in μm^{-1}). HM are the grains reconstructed with the h-minima markers and KM are the grains reconstructed with the K-means markers.*

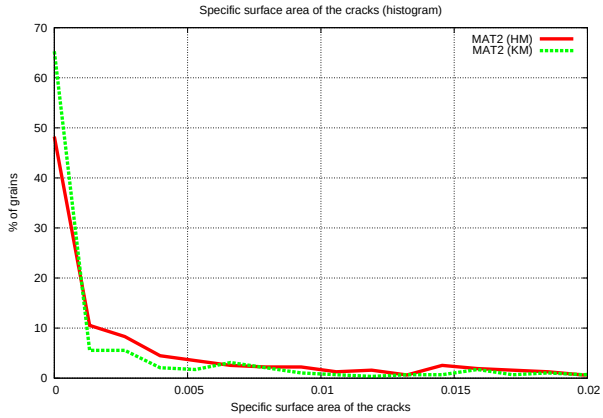

Fig. 13. *Histogram of the specific surface area of the cracks for MAT2 (given in μm^{-1}). HM are the grains reconstructed with the h-minima markers and KM are the grains reconstructed with the K-means markers.*

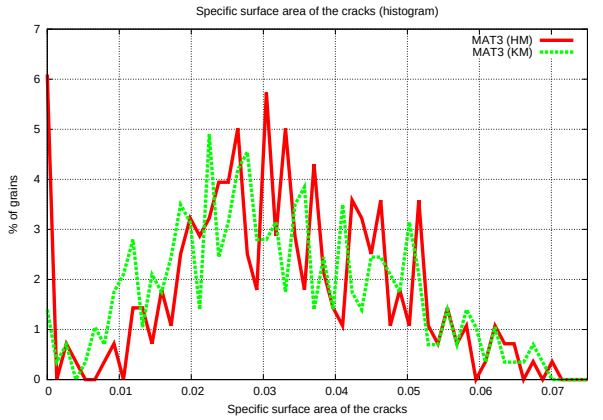

Fig. 14. *Histogram of the specific surface area of the cracks for MAT3 (given in μm^{-1}). HM are the grains reconstructed with the h-minima markers and KM are the grains reconstructed with the K-means markers.*

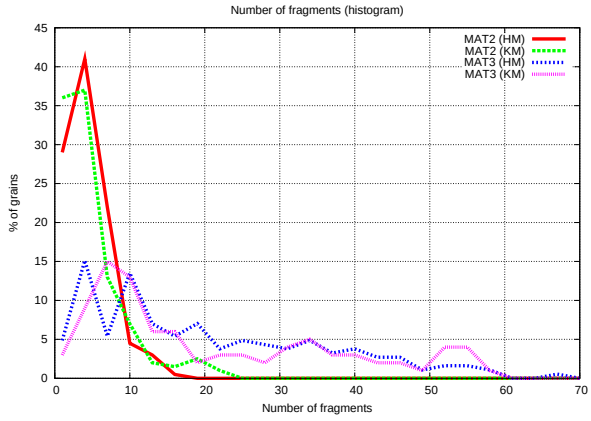

Fig. 15. *Histogram of the number of fragments for MAT2 and MAT3. HM are the grains reconstructed with the h-minima markers and KM are the grains reconstructed with the K-means markers.*

NUMBER OF FRAGMENTS

With the multiscale stochastic watershed algorithm introduced in the the previous section, the separation of the fragments can be achieved. Using the labels computed with the reconstruction algorithm, each segmented fragment is associated to its original grain.

Therefore, it is possible to know the number of fragments in each grain. This number includes the grain itself and is therefore larger or equal to 1. From this number, a normalized histogram is estimated, as illustrated in Fig. 15 for samples MAT2 and MAT3.

For the fragmented grains (MAT3), a three scale stochastic watershed is used. For the reference material without any mechanical impact, a simple stochastic watershed, without any additional steps, gives a correct segmentation.

As for the specific surface area and volume fraction, the damage of the grains can be quantified from these normalized histograms, the initial material showing almost no fragmentation, as compared to the shocked material, MAT3. The results obtained from the two types of segmentation are pretty close, showing again the robustness of the used segmentation techniques.

We can observe from the normalized histogram that many grains are very fragmented (≥ 30 fragments per grain, as seen in Fig. 15).

CONCLUSION

The proposed algorithm gives a satisfactory reconstruction of the fragmented grains with both markers sets. Visual inspection reveals that the K-means markers give better results when the grains are highly fragmented and if the fragments are scattered, but the boundaries of the grains are less accurate. The h-minima markers give correct boundaries between grains but fail to reconstruct a few grains.

In both cases, the closing of the grains depends on two parameters: the radius of the rhombicuboctahedron used and the volume of the holes. The h-minima markers require an additional parameter: h. The number of clusters used for the computation of the K-means is directly deduced from the image. Therefore, the K-means depend on less parameters and is less user-dependent.

The two algorithms require a similar time for the reconstruction. The reconstruction of the sample MAT2, using the K-means approach, requires 18 minutes and 12 seconds on a 3.00 GHz Pentium 4. The reconstruction of the same sample requires 19 minutes and 15 seconds using the h-minima approach.

Both approaches are very useful in order to generate data on the damage of materials from a fully automated 3D image analysis. The reproducibility of results on fragmentation obtained from two segmentation methods is very good. The analysis proves that the methods provide 3D damage measurements consistent with the mechanical impacts applied on the materials. They will provide useful information for the fully automatic characterization of damage in various conditions, helping to improve the reliability of solid propellants. A similar approach can be followed for the quantitative analysis of the progression of damage in materials, starting from 3D images.

ACKNOWLEDGMENTS

This work was supported by a grant from DGA (contract 2009 34 0006). The authors are grateful to Alain Fanget (CEA Gramat) for his advice during this study.

REFERENCES

Angulo J, Jeulin D (2007). Stochastic watershed segmentation. In: Banon GJF, Barrera J, Braga-Neto U, Hirata NST, eds. Proc 8th Int Symp Math Morpho (ISMM) 1:265–76.

Beucher S (1994). Watershed, hierarchical segmentation and waterfall algorithm. In: Serra J, Soille P, eds. Mathematical morphology and its applications to image processing. Computational Imaging and Vision 2:69–76.

Beucher S, Lantuéjoul C (1979). Use of watersheds in contour detection. In: Proc Int Worksh Image Process Real-Time Edge Motion Detect. Sept 17–21. Rennes, France.

Beucher S, Marcotegui B (2009). P algorithm, a dramatic enhancement of the waterfall transformation. Tech Rep. CMM/Mines Paristech.

Eppstein D (2000). Spanning trees and spanners. In: Sack JR, Urrutia J, eds. Handbook of Computational Geometry. Chap. 9, pp. 425–61. Elsevier.

Faessel M, Jeulin D (2010). Segmentation of 3D microtomographic images of granular materials with the stochastic watershed. J Microsc 239:17–31.

Gillibert L, Jeulin D (2011a). 3D reconstruction of fragmented granular materials. In: Proc 13th Int Cong Stereol (ICS-13). Beijing, China.

Gillibert L, Jeulin D (2011b). Stochastic multiscale segmentation constrained by image content. In: Soille P, Pesaresi M, Ouzounis GK, eds. Proc 10th Int Conf

Math Morpho Appl Image Signal Process (ISMM'11). Lect Not Comput Sci 6671:132–42.

Jeulin D (1991). Modèles morphologiques de structures aléatoires et de changement d'échelle. PhD Thesis. University of Caen, France.

Jeulin D (2008). Remarques sur la segmentation probabiliste. Tech. Rep. N-10/08/MM, CMM/Mines Paristech.

Lloyd SP (1982). Least squares quantization in PCM. IEEE Trans Inf Theory 28:129–37.

MacQueen JB (1967). Some methods for classification and analysis of multivariate observations. In: Cam LML, Neyman J, eds. Proc 5th Berkeley Symp Math Stat Probab, vol. 1. Berkeley: University of California Press.

Matheron G (1967). Eléments pour une théorie des milieux poreux. Paris: Masson.

Noyel G, Angulo J, Jeulin D (2007). Random germs and stochastic watershed for unsupervised multispectral image segmentation. In: Apolloni B, Howlett RJ, Jain L, eds. Proc Knowledge-Based Intell Inf Eng Syst (KES). Lect Not Comput Sci 4694:17–24.

Otsu N (1979). A threshold selection method from gray-level histograms. IEEE T Syst Man Cyb 9:62–6.

Parzen E (1962). On estimation of a probability density function and mode. Ann Math Stat 33:1065–76.

Serra J (1982). Image analysis and mathematical morphology. London: Academic Press.

Soille P (2003). Morphological image analysis: principles and applications. Secaucus, NJ, USA: Springer. 2nd ed.

Stawiaski J, Meyer F (2010). Stochastic watershed on graphs and hierarchical segmentation. In: Proc Eur Conf Math Indust. Wuppertal, Germany.

Image Anal Stereol 2013;32:117-125 doi:10.5566/ias.v32.p117-125
Original Research Paper

LÉVY-BASED ERROR PREDICTION IN CIRCULAR SYSTEMATIC SAMPLING

KRISTJANA ÝR JÓNSDÓTTIR✉ AND EVA B. VEDEL JENSEN

Department of Mathematics, Aarhus University, Ny Munkegade 118, 8000 Aarhus C, Denmark
e-mail: kyj@imf.au.dk, eva@imf.au.dk
(Received October 8, 2012; revised May 14, 2013; accepted May 15, 2013)

ABSTRACT

In the present paper, Lévy-based error prediction in circular systematic sampling is developed. A model-based statistical setting as in Hobolth and Jensen (2002) is used, but the assumption that the measurement function is Gaussian is relaxed. The measurement function is represented as a periodic stationary stochastic process X obtained by a kernel smoothing of a Lévy basis. The process X may have an arbitrary covariance function. The distribution of the error predictor, based on measurements in n systematic directions is derived. Statistical inference is developed for the model parameters in the case where the covariance function follows the celebrated p-order covariance model.

Keywords: Fourier series, Lévy basis, planar particles, stationary stochastic processes, stereology, systematic sampling.

INTRODUCTION

A long-standing problem in stereology is variance estimation in systematic sampling. One class of problems involves estimation of an integral of the form

$$Q = \int_0^{2\pi} x(\theta)\,\mathrm{d}\theta\,, \tag{1}$$

where $x(\theta)$ is an integrable function on $[0,2\pi)$, called the measurement function. The estimator typically considered is based on circular systematic sampling and takes the form

$$\widehat{Q}_n = \frac{2\pi}{n}\sum_{i=0}^{n-1} x(\Theta + \frac{2\pi i}{n})\,, \quad n \geq 1\,,$$

where Θ is uniformly distributed in $[0, \frac{2\pi}{n})$. For instance, if Y is a bounded convex planar set containing the origin O, examples of Eq. 1 are

$$x(\theta) = \begin{cases} \frac{1}{2}r(\theta)^2 & \text{if } Q = \text{area of } Y, \\ h(\theta) & \text{if } Q = \text{boundary length of } Y, \end{cases}$$

where $r(\theta)$ and $h(\theta)$ are the radial function and the support function of Y in direction θ, respectively. The geometric identity (Eq. 1) is in these cases a consequence of polar decomposition in the plane and an identity for mean width (Schneider, 1993, Eq. 5.3.12). If instead Y is a bounded convex spatial set containing O, the volume and the surface area of Y may be estimated by a two-step procedure which involves circular systematic sampling in a section through O and the use of the cubed radial function or the squared support function (Gundersen, 1988; Cruz-Orive, 2005). Yet another example is volume estimation by the so-called vertical rotator (Jensen and Gundersen, 1993).

In Gual-Arnau and Cruz-Orive (2000), a design-based procedure of approximating the variance of $\widehat{Q}_n$, based on modelling the covariogram of $x(\theta)$ by a polynomial model, is developed. Hobolth and Jensen (2002) consider a model-based procedure, where the measurement function is assumed to be a realization of a periodic stationary stochastic Gaussian process $X = \{X(\theta) : \theta \in [0,2\pi)\}$. It is shown in Hobolth and Jensen (2002) that the covariogram model considered in the paper by Gual-Arnau and Cruz-Orive (2000) is a special case of a p-order covariance model for the stochastic process X in the model-based set-up.

The p-order covariance model is given by

$$c(\theta) = \mathrm{Cov}(X(\theta),X(0)) = \lambda_0 + \sum_{s=2}^{\infty}\lambda_s\cos(s\theta)\,,$$
$$\lambda_s^{-1} = \alpha + \beta(s^{2p} - 2^{2p})\,, \quad s \geq 2\,, \tag{2}$$

where the model parameters satisfy $p > 1/2$, $\alpha,\beta > 0$. In Hobolth *et al.* (2003), this parametric covariance function has been used in the modelling of the radial function of a random star-shaped planar particle. In this case, p determines the smoothness of the particles boundary while α and β determine the 'global' and the 'local' shape of the particle, respectively. (Note that in Eq. 2, λ_1 is set to zero which ensures that the reference point of the particle is approximately the centre of mass.) The model-based counterpart

of the design-based methodology provided in Gual-Arnau and Cruz-Orive (2000) was further developed in Jónsdóttir *et al.* (2006), where the general form of the p-order covariance model (Eq. 2) was used to obtain a more accurate approximation of the prediction error $\mathbb{E}(\widehat{Q}_n - Q)^2$.

In Hobolth and Jensen (2002) and Jónsdóttir *et al.* (2006), the process X is assumed to be Gaussian. Motivated by the fact that powers of the radial function and the support function are used in practice, we will in this paper consider non-Gaussian models, obtained as a kernel smoothing of a so-called Lévy basis. As we will show, it is possible under the Lévy-based model to derive the distribution of the error predictor $\widehat{Q}_n - Q$ which may be markedly non-Gaussian for the moderate sizes of n used in practice.

Lévy-based modelling has been popular in recent years, e.g. in the modelling of turbulent flows, spatio-temporal growth, spatial point processes and random fields (Barndorff-Nielsen and Schmiegel, 2004; Jónsdóttir *et al.*, 2008; Hellmund *et al.*, 2008; Jónsdóttir *et al.*, 2013). More specifically, we will consider stochastic processes of the form

$$X(\theta) = \mu + \int_0^{2\pi} k(\theta - \phi) Z(\mathrm{d}\phi) \,, \quad \theta \in [0, 2\pi) \,,$$

where μ determines the mean of the process, Z is a homogeneous and factorizable Lévy basis on $[0, 2\pi)$ and k is a deterministic kernel function. In principle, any covariance model, including the p-order covariance model, can be induced under this modelling framework, by assuming a specific form of the kernel function (see the next section). Under the p-order model, it is easy to control the local and global fluctuations of the stochastic process X. The Lévy-based models with p-order covariance thus constitute a flexible and tractable model class. In particular, this model class has more structure than the non-Gaussian models considered in Hobolth *et al.* (2003) and this allows us to derive distributional results.

The composition of the remaining part of the paper is as follows. First, a theoretical background for stationary periodic processes with period 2π, based on kernel smoothing of a Lévy basis, is given. Then, estimation of $\mathbb{E}(\widehat{Q}_n - Q)^2$ under the general Lévy-based model is discussed. The distribution of the error predictor $\widehat{Q}_n - Q$ under the Lévy-based model is derived, and it is shown how to estimate this distribution. An example of random particles simulated from a Lévy-based model is given together with the distribution of the n-point area estimator of these particles. Finally, a discussion is provided. Some technical derivations are deferred to an appendix.

LÉVY-BASED STOCHASTIC PROCESSES ON THE CIRCLE

This section provides an overview of stationary periodic processes on $[0, 2\pi)$ based on integration with respect to a Lévy basis. For further details on the general theory on Lévy bases, in particular, the integration with respect to a Lévy basis, the reader is referred to Barndorff-Nielsen and Schmiegel (2004) and Hellmund *et al.* (2008).

Let $X = \{X(\theta) : \theta \in [0, 2\pi)\}$ be a 2π periodic stationary stochastic process on $[0, 2\pi)$, given by

$$X(\theta) = \mu + \int_0^{2\pi} k(\theta - \phi) Z(\mathrm{d}\phi) \,, \quad \theta \in [0, 2\pi) \,, \quad (3)$$

where μ determines the mean of the process, Z is a homogeneous and factorizable Lévy basis on $[0, 2\pi)$ and k is an even periodic kernel function with period 2π and a Fourier representation

$$k(\theta) = \xi_0 + \sum_{s=1}^{\infty} \xi_s \cos(s\theta) \,. \quad (4)$$

The model (Eq. 3) is the continuous analogue of the following discrete model

$$X(\theta) = \mu + \sum_{\phi} k(\theta - \phi) Z(\phi) \,,$$

where the sum is over an equally spaced set of angles and the random variables $Z(\phi)$ are independent and identically distributed, the common distribution being infinitely divisible. The integral in Eq. 3 is formally defined as a limit in probability (Rajput and Rosinski, 1989). A spatio-temporal version of Eq. 3 has previously been considered in Jónsdóttir *et al.* (2008).

The Lévy basis Z is extended by $Z(A + 2\pi m) = Z(A)$ for all $m \in \mathbb{Z}$ and all Borel sets $A \in \mathscr{B}([0, 2\pi))$. A Lévy basis has the property that $Z(A_1), \ldots, Z(A_n)$ are independent when $A_1, \ldots, A_n \in \mathscr{B}([0, 2\pi))$ are disjoint and $Z(A)$ is infinitely divisible for any $A \in \mathscr{B}([0, 2\pi))$. The assumption of homogeneity implies that all the finite-dimensional distributions of Z are translation invariant.

If Z is Gaussian, the integral in Eq. 3 exists if k is L^2-integrable with respect to the Lebesgue measure on $[0, 2\pi)$. When Z is a so-called Lévy jump basis (*e.g.*, Gamma or inverse Gaussian Lévy basis), the integral exists if k is integrable with respect to the Lebesgue measure on $[0, 2\pi)$ and if $\int_{\mathbb{R}} |r| V(dr) < \infty$, where V is the Lévy measure associated with Z. These results follow from Hellmund *et al.* (2008, Lemma 1).

An important entity associated with a Lévy basis is its spot variable Z' which is infinitely divisible. Without loss of generality we will in what follows assume that the spot variable Z' is centered, $Z' = W - \mathbb{E}(W)$, where W is an infinitely divisible random variable.

The following theorem characterizes the distribution of the stochastic variable $X(\theta)$.

Theorem 1. *The stochastic variable $X(\theta)$ has the cumulant generating function*

$$\begin{aligned} K_X(t) &= \log \mathbb{E}(\mathrm{e}^{tX(\theta)}) \\ &= t(\mu - 2\pi\xi_0\mathbb{E}(W)) + \int_0^{2\pi} K_W(tk(\phi))\,\mathrm{d}\phi\ , \end{aligned} \tag{5}$$

where $K_W(t)$ is the cumulant generating function of W. Moreover, the derivatives of $K_X(t)$ are given by (when they exist)

$$\begin{aligned} K_X'(t) &= \mu - 2\pi\xi_0\mathbb{E}(W) + \int_0^{2\pi} K_W'(tk(\phi))k(\phi)\,\mathrm{d}\phi\ , \\ K_X^{(r)}(t) &= \int_0^{2\pi} K_W^{(r)}(tk(\phi))k(\phi)^r\,\mathrm{d}\phi\ , \quad r \geq 2\ , \end{aligned} \tag{6}$$

where $K_W^{(r)}(t)$ denotes the r'th derivative of $K_W(t)$.

Proof. The result is obtained by using that the cumulant generating function of the integral $f \bullet Z = \int_0^{2\pi} f(\theta)Z(d\theta)$ of a function f with respect to a homogeneous and factorizable Lévy basis Z is given by

$$K_{f\bullet Z}(t) = \int_0^{2\pi} K_{Z'}(tf(\theta))\,\mathrm{d}\theta\ , \tag{7}$$

where Z' is the spot variable associated with Z, *cf.* Hellmund *et al.* (2008, Eq. 10). □

It follows that the cumulants of the stochastic variable $X(\theta)$ are given by

$$\begin{aligned} &\kappa_1(X(\theta)) = \mu, \\ &\kappa_r(X(\theta)) = \kappa_r(W)\int_0^{2\pi} k(\phi)^r\,\mathrm{d}\phi\ , \quad r \geq 2\ , \end{aligned}$$

where $\kappa_r(W)$ denotes the r-th cumulant of the stochastic variable W. Possible choices of the distribution of W are the Gaussian, Gamma and inverse Gaussian distributions. When the kernel function is proportional to an indicator function, $k(\theta) = c\mathbf{1}_A(\theta)$ for $A \in \mathscr{B}([0,2\pi))$, the marginal distribution of $X(\theta)$ will be of the same type as that of W. Otherwise, the marginal distribution will not be as simple, but the process X will inherent the name of the distribution of the underlying spot variable, *e.g.*, when W is Gamma distributed, X is called a Gamma Lévy process, irrespectively of the choice of the kernel function. We will typically assume that $\kappa_2(W) = 1$, *i.e.*, the skewness and kurtosis of W are equal to the third and fourth cumulant, respectively. In Table 1, we give the cumulant generating function, third and fourth cumulants of W for the three distributions mentioned above. Note that as W has unit variance, the Gamma and inverse Gaussian Lévy bases are only determined by a single parameter $\eta > 0$. The Lévy measures V of the Gamma and inverse Gaussian Lévy bases satisfy the condition $\int_{\mathbb{R}} |r|V(\mathrm{d}r) < \infty$ for the existence of the integral in Eq. 3, *cf.* Hellmund *et al.* (2008, Example 3).

In principle, any covariance function can be modelled within this set-up. This can be seen, using the theorem below.

Theorem 2. *The stochastic process X has a mean value μ and a covariance function*

$$c(\theta) = \lambda_0 + \sum_{s=1}^{\infty} \lambda_s \cos(s\theta)\ , \quad \theta \in [0, 2\pi)\ ,$$

where

$$\lambda_0 = 2\pi\xi_0^2\kappa_2(W)\ , \quad \lambda_s = \pi\xi_s^2\kappa_2(W)\ , \quad s \geq 1\ . \tag{8}$$

Proof. Using that

$$\begin{aligned} c(\theta) &= \mathrm{Cov}(X(\theta), X(0)) \\ &= \kappa_2(W)\int_0^{2\pi} k(\theta - \phi)k(-\phi)\,\mathrm{d}\phi\ , \end{aligned}$$

we easily obtain Eq. 8. □

Using Theorem 2, we can construct the candidate kernel k that induces a given covariance function c. For instance, if c follows the p-order model (Eq. 2), then k is of the form specified in Eq. 4 with

$$\begin{aligned} \xi_0 &= \sqrt{\frac{\lambda_0}{2\pi\kappa_2(W)}}\ , & \xi_1 &= 0\ , \\ \xi_s &= \frac{1}{\sqrt{\pi\kappa_2(W)[\alpha + \beta(s^{2p} - 2^{2p})]}}\ , & s &\geq 2\ . \end{aligned}$$

This choice of kernel will for a Gaussian Lévy basis give a well-defined integral in Eq. 3 if $p > 1/2$, while for a Gamma or an inverse Gaussian basis the integral is well-defined if $p > 1$.

Table 1. *Examples of the distribution of W, together with the corresponding cumulant generating function, and the third and fourth cumulants.*

distribution	Gaussian	Gamma	Inverse Gaussian
W	$N(0,1)$	$\Gamma(\eta,\sqrt{\eta})$	$IG(\eta^3,\eta)$
$K_W(t)$	$t^2/2$	$-\eta\log(1-t/\sqrt{\eta})$	$\eta^4(1-\sqrt{1-2t/\eta^2})$
$\kappa_3(W)$	0	$2/\sqrt{\eta}$	$3/\eta^2$
$\kappa_4(W)$	0	$6/\eta$	$15/\eta^4$

ESTIMATING $\mathbb{E}(\hat{Q}_n - Q)^2$ UNDER THE LÉVY-BASED MODEL

In Hobolth and Jensen (2002), the focus was on the prediction error $\mathbb{E}(\widehat{Q}_n - Q)^2$. If the covariance function of X has the following Fourier expansion

$$c(\theta) = \lambda_0 + \sum_{s=1}^{\infty} \lambda_s \cos(s\theta)\,, \quad \theta \in [0, 2\pi)\,,$$

then it was shown in Hobolth and Jensen (2002) that

$$\mathbb{E}(\widehat{Q}_n - Q)^2 = \sum_{k=1}^{\infty} \lambda_{nk}\,, \tag{9}$$

where λ_{nk} is the Fourier coefficient of order $n \cdot k$ in the Fourier expansion of the covariance function of X. Note that in Hobolth and Jensen (2002), circular systematic sampling on $[0,1)$ instead of $[0,2\pi)$ is considered, so Eq. 9 represents an adjusted version of Hobolth and Jensen (2002, Eq. 8).

In Hobolth *et al.* (2003), a procedure for estimating the prediction error under a Gaussian p-order model was developed, based on a Fourier expansion of X

$$X(\theta) \stackrel{d}{=} A_0 + \sum_{s=1}^{\infty} \left(A_s \cos(s\theta) + B_s \sin(s\theta)\right)\,, \quad \theta \in [0, 2\pi)\,,$$

where $\stackrel{d}{=}$ means equality in distribution and

$$A_0 = \frac{1}{2\pi}\int_0^{2\pi} X(\theta)\,\mathrm{d}\theta\,,$$
$$A_s = \frac{1}{\pi}\int_0^{2\pi} X(\theta)\cos(s\theta)\,\mathrm{d}\theta\,,$$
$$B_s = \frac{1}{\pi}\int_0^{2\pi} X(\theta)\sin(s\theta)\,\mathrm{d}\theta\,.$$

When X is a periodic stationary Gaussian process, the Fourier coefficients of X become independent and normally distributed, $A_s \sim B_s \sim N(0,\lambda_s)$. As suggested in Hobolth *et al.* (2003), the parameters α and β in the p-order model can then be estimated using maximum likelihood estimation based on the first S Fourier coefficients,

$$L_{0,S}(\alpha,\beta) = \prod_{s=2}^{S} \frac{1}{2\pi\lambda_s(\alpha,\beta)} \exp\left(-\frac{(a_s^2+b_s^2)}{2\lambda_s(\alpha,\beta)}\right), \tag{10}$$

where $\lambda_s(\alpha,\beta)$, $s = 2,\ldots,S$, satisfy (2) and a_s and b_s, $s = 2,\ldots,S$, denote discretized Fourier coefficients of X.

In this section, we will show that this procedure can be used under the general Lévy-based model. The following theorem gives the distribution of the Fourier coefficients and their relations under the general Lévy-based model. In the Gaussian case, the theorem can be found *e.g.*, in Dufour and Roy (1976).

Theorem 3. *The stationary Lévy-based stochastic process X can be written in terms of its Fourier coefficients as*

$$X(\theta) = A_0 + \sum_{s=1}^{\infty} \left(A_s \cos(s\theta) + B_s \sin(s\theta)\right)\,, \quad \theta \in [0, 2\pi)\,,$$

where $A_0 = \mu + \xi_0 Z([0,2\pi))$,

$$A_s = \xi_s \int_0^{2\pi} \cos(s\phi) Z(\mathrm{d}\phi)$$
$$B_s = \xi_s \int_0^{2\pi} \sin(s\phi) Z(\mathrm{d}\phi)\,. \tag{11}$$

Moreover, the Fourier coefficients are pairwise uncorrelated and the Fourier coefficients of order s have the same distribution which is characterized by the cumulant generating function $K_{A_s}(t) = K_{B_s}(t) = K_U(t\xi_s)$, where

$$K_U(t) = \int_0^{2\pi} K_W(t\cos(\theta))\,\mathrm{d}\theta\,.$$

Proof. Writing the kernel function in terms of its Fourier representation and then calculate the Fourier coefficients of X gives Eq. 11. The Fourier coefficients are uncorrelated as for all $r, s \geq 1$,

$$\mathrm{Cov}(A_s, B_r) = \kappa_2(W) \int_0^{2\pi} \cos(s\phi)\sin(r\phi)\,\mathrm{d}\phi = 0\,,$$

and

$$\mathrm{Cov}(A_s, A_r) = \kappa_2(W) \int_0^{2\pi} \cos(s\phi)\cos(r\phi)\,\mathrm{d}\phi = 0\,,$$
$$\mathrm{Cov}(B_s, B_r) = \kappa_2(W) \int_0^{2\pi} \sin(s\phi)\sin(r\phi)\,\mathrm{d}\phi = 0\,,$$

for all $r, s \geq 1, r \neq s$. The cumulant generating function of A_s is given by

$$\begin{aligned} K_{A_s}(t) &= \int_0^{2\pi} K_{Z'}(t\xi_s \cos(s\phi))\,\mathrm{d}\phi \\ &= \frac{1}{s}\int_0^{2\pi s} K_{Z'}(t\xi_s \cos(\phi))\,\mathrm{d}\phi = K_U(\xi_s t)\,, \end{aligned}$$

and a similar argument shows that $K_{B_s}(t) = K_U(\xi_s t)$. □

The cumulant generating function of A_s and B_s yield simple expressions for their cumulants, which are given by

$$\kappa_1(A_0) = \mu\,, \quad \kappa_r(A_0) = 2\pi\xi_0\kappa_r(W)\,, \quad r \geq 2\,,$$

and

$$\kappa_r(A_s) = \kappa_r(B_s) = 2\pi\xi_s^r \frac{(r-1)!!}{r!!}\kappa_r(W)1(r \text{ even})\,,$$

for $s \geq 1$ and $r \geq 1$. Here and in the following, we let for a positive integer n,

$$n!! = \begin{cases} 2\cdot 4\cdots n\,, & \text{if } n \text{ even}, \\ 1\cdot 3\cdots n\,, & \text{if } n \text{ uneven}. \end{cases}$$

This means that A_s and B_s have mean, variance, skewness and kurtosis of the following form:

$$\kappa_1(A_s) = 0\,, \quad \kappa_2(A_s) = \pi\xi_s^2\kappa_2(W)\,,$$
$$\gamma_1(A_s) = 0\,, \quad \gamma_2(A_s) = \frac{3}{4\pi}\gamma_2(W)\,,$$

where $\gamma_2(W)$ is the kurtosis of W. Moreover, the normalized Fourier coefficients of order $s = 1, 2, \ldots$, obtained by $\tilde{A}_s = A_s/\xi_s$ and $\tilde{B}_s = B_s/\xi_s$, will all have the same distribution characterized by the cumulant generating function $K_U(t)$.

From Theorems 2 and 3, it follows that for a non-Gaussian Lévy basis Z the Fourier coefficients will be uncorrelated with variance $\lambda_s(\alpha, \beta)$. Furthermore, the distribution of the Fourier coefficients in the non-Gaussian and Gaussian model only differs in even cumulants of order four and higher. Therefore, Eq. 10 can be regarded as a pseudo-likelihood function for (α, β) also in the non-Gaussian case.

Fig. 1 shows the small difference in the saddlepoint densities of the normalized Fourier coefficients and the Gaussian density for different values of η in the case of a Gamma Lévy basis. Furthermore, a simulation study indicated that the estimates of (α, β) are robust against deviations from Gaussianity in the underlying distribution, but the mean square error of the estimates increases somewhat as η decreases.

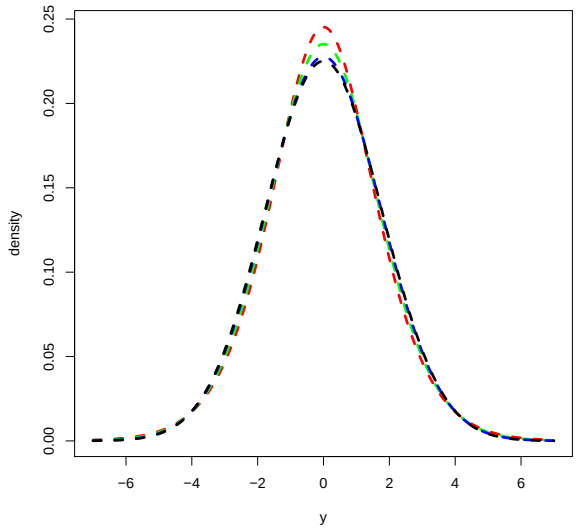

Fig. 1. *The saddlepoint density of the normalized Fourier coefficients for $\eta = 2$ (red line), $\eta = 4$ (green line) and $\eta = 16$ (blue line). The density in a Gaussian model is shown for comparison (black line).*

THE DISTRIBUTION OF $\hat{Q}_n - Q$ UNDER THE LÉVY-BASED MODEL

In the previous section, we have seen that the method developed in Hobolth *et al.* (2003) for estimating $\mathbb{E}(\widehat{Q}_n - Q)^2$ based on a Gaussian process is robust against departures from the distributional assumption. In this section, we will derive the distribution of the error predictor $\widehat{Q}_n - Q$ which may be markedly non-Gaussian.

Theorem 4. *Under the Lévy-based model, the error predictor is distributed as*

$$\widehat{Q}_n - Q \sim 2\pi \int_0^{2\pi} k_n(\phi) Z(\mathrm{d}\phi)\,, \tag{12}$$

where

$$k_n(\phi) = \sum_{s=1}^{\infty} \xi_{sn}\cos(sn\phi)\,.$$

The distribution of $\widehat{Q}_n - Q$ is characterized by its cumulant generating function

$$K_{\widehat{Q}_n - Q}(t) = \int_0^{2\pi} K_W(2t\pi k_n(\phi))\,\mathrm{d}\phi\ .$$

Proof. Recall that

$$\widehat{Q}_n = \frac{2\pi}{n}\sum_{i=0}^{n-1} X(\Theta + \frac{2\pi i}{n})\ , \quad (n \geq 1)\ ,$$

where Θ is uniformly distributed in $[0, 2\pi/n)$. Without loss of generality we can assume that $\Theta = 0$ as the distribution of $\widehat{Q}_n$ does not depend on Θ. The result given in Eq. 12 is obtained by observing that the mean of the kernel functions is given by

$$\frac{1}{n}\sum_{j=0}^{n-1} k(\frac{2\pi j}{n} - \phi) = \xi_0 + \sum_{s=1}^{\infty} \xi_{sn}\cos(sn\phi)\ .$$

The expression for the cumulant generating function of $\widehat{Q}_n - Q$ is a consequence of Eq. 7. □

As the cumulant generating function of $\widehat{Q}_n - Q$ has a simple form, its cumulants are easily available. In particular, it enables us to obtain a saddlepoint approximation of its density. An alternative is to use Theorem 4 for simulating the distribution of $\widehat{Q}_n - Q$.

Example. Let us consider a Lévy-based model (Eq. 3) for X with a Gamma Lévy basis Z and k chosen such that the covariance function of X follows a p-order model. Under this model the Fourier coefficients A_s, and B_s, $s \geq 1$, of $X(\theta)$ have mean, variance, skewness and kurtosis,

$$\kappa_1(A_s) = 0\ , \quad \kappa_2(A_s) = \pi\xi_s^2 = \lambda_s(\alpha,\beta)\ ,$$
$$\gamma_1(A_s) = 0\ , \quad \gamma_2(A_s) = \frac{9}{2\pi\eta}\ .$$

This model may, for instance, be used to model the squared radial function of random star-shaped planar particles containing the origin. Fig. 2 shows examples of particles simulated from such a model, using different values of η. The value of p, α and β was $p = 2$, $\log\alpha = 6$ and $\log\beta = -3$. We used $\eta = 2, 4, 16$; a low value of η corresponds to an underlying distribution with a heavy tail. The value of η controls the frequency and size of the irregularities of the boundary of the particles. Small values of η will produce particles with few large fluctuations on the particle boundary and less smaller fluctuations. Higher values of η will produce particles with more frequently occurring moderate fluctuations across the boundary.

Fig. 3 shows the corresponding saddlepoint densities of the estimated area of the particles for two different values of n. □

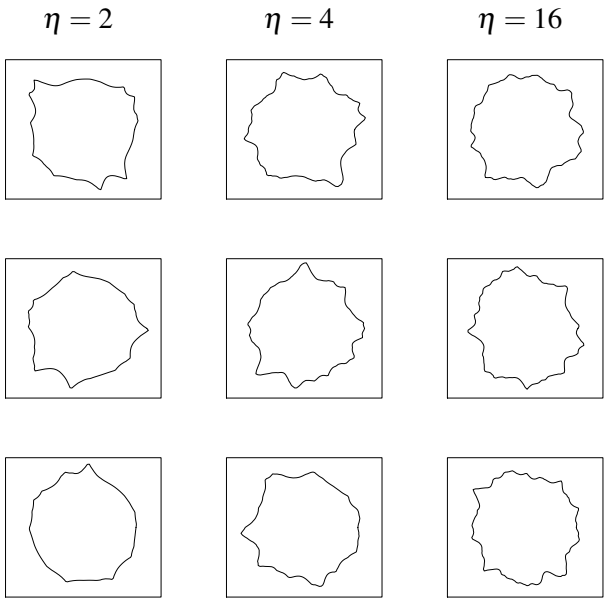

Fig. 2. *Realizations of particles obtained by assuming that the squared radial function is given by a Gamma Lévy process with a p-order covariance function. The values of p, α and β were $p = 2$, $\log\alpha = 6$ and $\log\beta = -3$. Each column corresponds to realizations for a fixed value of η ($\eta = 2, 4, 16$).*

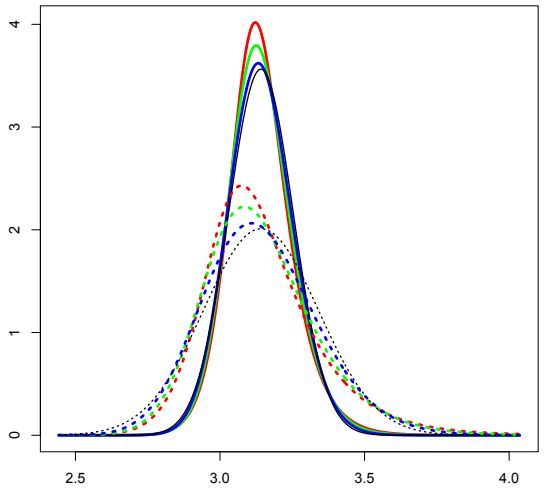

Fig. 3. *The saddlepoint density of the n-point area estimate for $n = 5$ (stippled) and $n = 10$ (full line). The different colours represent densities for the three particles considered: $\eta = 2$ (red lines), $\eta = 4$ (green lines) and $\eta = 16$ (blue lines). Densities for a Gaussian model is shown for comparison (black lines).*

In applications, it is needed to estimate the parameter η of the underlying Lévy basis Z, *i.e.*, the parameter of the distribution of W. For a given kernel function k, we have a simple expression for the cumulant generating function of X and its derivatives (when they exist), *cf.* Theorem 1. We suggest estimating the parameter η determining the Lévy basis by considering the saddlepoint approximation of the density of $X(\theta)$. For more details on saddlepoint approximations, *cf.* Jensen (1995). The first order saddlepoint approximation of the density is given by

$$\tilde{f}(x) = \frac{1}{\sqrt{2\pi K_X''(\hat{t}(x))}} \mathrm{e}^{K_X(\hat{t}(x)) - \hat{t}(x)x},$$

where $\hat{t}(x)$ is the solution to the saddlepoint equation

$$K_X'(t) = x\,.$$

Note that the saddlepoint equation is non-linear when Z is non-Gaussian, but can be solved numerically, using a Newton method for a given kernel function k. A better approximation of the density of $X(\theta)$ is obtained by multiplying the density with the correction factor

$$c(\hat{t}(x)) = 1 + \frac{K_X^{(4)}(\hat{t}(x))}{8K_X''(\hat{t}(x))^2} - \frac{5}{24}\left(\frac{K_X^{(3)}(\hat{t}(x))}{K_X''(\hat{t}(x))^{3/2}}\right)^2.$$

Given an estimation of the kernel function k we can establish a pseudo-likelihood function based on the observations of the stochastic process X given by

$$L(\eta) = \prod_{i=1}^{n} \tilde{f}(x(\theta_i))\,.$$

Here, $\tilde{f}(x(\theta_i))$ is calculated using the approximated kernel function

$$\hat{k}_S(\theta) = \sum_{s=2}^{S} \hat{\xi}_s \cos(s\theta)\,,$$

where $\hat{\xi}_s = \sqrt{\lambda_s(\hat{\alpha},\hat{\beta})/\pi}$ is obtained using the estimates of (α,β). Note that we need to normalize the densities $\tilde{f}(x_i)$ for each value of η, when maximizing the likelihood function $L(\eta)$. If the estimated likelihood function is an increasing function of η, this suggests that the underlying Lévy basis is Gaussian.

The cumulant generating function and its derivatives have simple analytic expressions, when the underlying Lévy basis is a Gamma basis or Inverse Gaussian basis. These expressions can be derived by combining Theorem 1 and Table 1. For a Gamma Lévy process the cumulant generating function of $X(\theta)$ and its derivatives are given by

$$K_X(t) = t(\mu - 2\pi\xi_0\sqrt{\eta}) - \eta\int_0^{2\pi} \log\left(1 - \frac{tk(\phi)}{\sqrt{\eta}}\right)\mathrm{d}\phi\,,$$

$$K_X'(t) = \mu - 2\pi\xi_0\sqrt{\eta} + \eta\int_0^{2\pi} \frac{k(\phi)}{\sqrt{\eta} - tk(\phi)}\,\mathrm{d}\phi\,,$$

$$K_X^{(r)}(t) = (r-1)!\eta\int_0^{2\pi} \frac{k(\phi)^r}{(\sqrt{\eta} - tk(\phi))^r}\,\mathrm{d}\phi\,, \quad r \geq 2\,.$$

For an inverse Gaussian Lévy process the cumulant generating function of $X(\theta)$ and its derivatives are given by

$$K_X(t) = t(\mu - 2\pi\xi_0\eta^2) + \eta^4\int_0^{2\pi}\left(1 - \sqrt{1 - \frac{2tk(\phi)}{\eta^2}}\right)\mathrm{d}\phi\,,$$

$$K_X'(t) = \mu - 2\pi\xi_0\eta^2 + \eta^3\int_0^{2\pi} \frac{k(\phi)}{\sqrt{\eta^2 - 2tk(\phi)}}\,\mathrm{d}\phi\,,$$

$$K_X^{(r)}(t) = (2r-3)!!\eta^3\int_0^{2\pi} \frac{k(\phi)^r}{(\eta^2 - 2tk(\phi))^{r-\frac{1}{2}}}\,\mathrm{d}\phi\,, \quad r \geq 2\,.$$

In both cases, the saddlepoint approximation of the density of $X(\theta)$ are easily obtainable using numerical integration and a Newton algorithm for finding the saddlepoint. Note that the saddlepoint approximation of the density function for an arbitrary η can be written in terms of the saddlepoint approximation of the density, the cumulant generating derivatives and saddlepoint solution for $\eta = 1$.

CONCLUSION AND PERSPECTIVES

We have developed a Lévy-based error prediction in circular systematic sampling. In contrast to previous model-based methods, we consider a flexible class of non-Gaussian measurement functions based on kernel smoothing of a homogeneous Lévy basis. In particular, we have derived the distribution of the error predictor in circular systematic sampling. The modelling framework allows us to consider in principle any given covariance structure of the measurement function, in particular the popular p-order covariance model which enables controlling the local and global fluctuations of the measurement function.

Relation to generalized p-order models. Note that as the Lévy-based process X is strictly stationary, it can be shown that X has a polar expansion of the form

$$X(\theta) = \mu + \sqrt{2}\sum_{s=0}^{\infty}\sqrt{C_s}\cos(s(\theta - D_s))\,,$$

where the random variables

$$C_s = \frac{1}{2}(A_s^2 + B_s^2) = \lambda_s Z_s\,, \quad D_s \sim U[0, \frac{2\pi}{s}]\,, \quad s \geq 1\,,$$

are independent, *cf.* the Appendix, and $\mathbb{E}(Z_s) = 1$. Here, the variable Z_s can be expressed as

$$Z_s = \frac{1}{2\pi\kappa_2(W)} \int_0^{2\pi} \int_0^{2\pi} \cos(s(\theta-\phi)) Z(\mathrm{d}\theta) Z(\mathrm{d}\phi) \, .$$

This shows that the Lévy-based models are closely related to the generalized p-order models proposed in Hobolth *et al.* (2003), but the Lévy-based models have more structure that allows for derivation of distributional results.

Modelling particles in 2D and 3D. The model (Eq. 3) can be used directly to model the shape of featureless two-dimensional particles by assuming that a particle Y is a stochastic deformation of a template particle Y_0. If r_0 is a radial function of a template particle, we let the radial function of Y be of the form $R(\theta) = r_0(\theta) + X(\theta)$, where X is a zero mean Lévy-based stochastic process. The strength of this technique is two-folded. Firstly, the global and local fluctuations of the Lévy-based stochastic process are controlled by the variance of the Fourier coefficients which are determined by the kernel function. Secondly, the underlying Lévy basis determines the frequency and size of the irregularities of the process. Finally, the methodology presented can be extended to model the shape of three-dimensional featureless particles, by considering Lévy-based processes on the unit sphere $\mathbb{S}_2$. Hansen *et al.* (2011) consider three-dimensional Lévy particles using different covariance models. The focus is here on the Hausdorff dimension of the boundary of particles obtained using a Gaussian basis.

Approximations of densities. The saddlepoint approximation was applied here to obtain an approximation of the density of $X(\theta)$ in the Lévy-based stochastic model. As the cumulant generating function is easily obtainable for stochastic convolutions of the type

$$X(\xi) = \int f(\eta - \xi) Z(\mathrm{d}\eta) \, , \quad \xi \in \mathbb{R}^n \, ,$$

where $f : \mathbb{R}^n \to \mathbb{R}$ and Z is a homogeneous Lévy basis on $\mathbb{R}^n$, the saddlepoint approximation of the density is an attractive tool for studying Lévy-based convolution models in general. For the stochastic processes considered here, other types of approximations of densities can also be considered based on approximating A_s and B_s by differences of variables from the same family of distributions as W. As an example one could consider approximating the density of the Fourier coefficients by a type II McKay distribution (Holm and Alouini, 2004), when the underlying Lévy basis is a Gamma Lévy basis.

Choice of kernel function. Finally, it should be emphasized that assuming that the kernel function is even does not affect the flexibility of the induced covariance model. When k is not necessarily even,

$$k(\theta) = \xi_0 + \sum_{s=1}^{\infty} (\xi_{s,1} \cos(s\theta) + \xi_{s,2} \sin(s\theta)) \, ,$$

the covariance function of X is given by

$$C(\theta) = 2\pi\xi_0^2 + \pi \sum_{s=1}^{\infty} (\xi_{s,1}^2 + \xi_{s,2}^2) \cos(s\theta) \, , \quad \theta \in [0, 2\pi) \, .$$

Moreover, the Fourier coefficients of the process X will still be uncorrelated and have the same distribution described by the cumulant generating function

$$K_{A_s}(t) = \int_0^{2\pi} K_W(t\xi_{s,1}\cos\phi - t\xi_{s,2}\sin\phi) \, \mathrm{d}\phi \, ,$$

and cumulants given by

$$\begin{aligned} \kappa_r(A_s) &= \kappa_r(B_s) \\ &= 2\pi(\xi_{s,1}^2 + \xi_{s,2}^2)^{r/2} \frac{(r-1)!!}{r!!} \kappa_r(W) 1(r \text{ even}) \, . \end{aligned}$$

APPENDIX: A NOTE ON POLAR EXPANSION OF A STATIONARY PROCESS

Consider a stationary process $X = \{X(\theta) : \theta \in [0, 2\pi)\}$ with Fourier expansion

$$X(\theta) = A_0 + \sum_{s=1}^{\infty} (A_s \cos(s\theta) + B_s \sin(s\theta)) \, ,$$

and Polar expansion

$$X(\theta) = \mu + \sqrt{2} \sum_{s=0}^{\infty} \sqrt{C_s} \cos(s(\theta - D_s)) \, ,$$

where $C_s = \frac{1}{2}(A_s^2 + B_s^2)$ and $sD_s = \arctan(B_s/A_s)$, $s \geq 1$. It is easily seen that

$$X(\theta + h) = A_0 + \sum_{s=1}^{\infty} (A_s(h) \cos(s\theta) + B_s(h) \sin(s\theta)) \, ,$$

where

$$\begin{pmatrix} A_s(h) \\ B_s(h) \end{pmatrix} = \begin{pmatrix} \cos(sh) & \sin(sh) \\ -\sin(sh) & \cos(sh) \end{pmatrix} \begin{pmatrix} A_s \\ B_s \end{pmatrix} = V \begin{pmatrix} A_s \\ B_s \end{pmatrix} ,$$

and V is a rotation matrix. As for each $h \in [0, 2\pi)$, $\{X(\theta) : \theta \in [0, 2\pi)\}$ and $\{X(\theta + h) : \theta \in [0, 2\pi)\}$ have the same distribution,

$$\begin{pmatrix} A_s \\ B_s \end{pmatrix} \sim \begin{pmatrix} A_s(h) \\ B_s(h) \end{pmatrix} = V \begin{pmatrix} A_s \\ B_s \end{pmatrix} .$$

We now have that

$$E_s := \begin{pmatrix} A_s/\sqrt{A_s^2+B_s^2} \\ B_s/\sqrt{A_s^2+B_s^2} \end{pmatrix} \sim V \begin{pmatrix} A_s/\sqrt{A_s^2+B_s^2} \\ B_s/\sqrt{A_s^2+B_s^2} \end{pmatrix} = VE_s\,,$$

and consequently E_s is uniformly distributed on the unit circle, *i.e.*, $\arctan(B_s/A_s)$ is uniformly distributed on $[0,2\pi)$ and D_s is uniformly distributed on $[0,2\pi/s)$. Now consider the conditional distribution of $\sqrt{2C_s} = \sqrt{A_s^2+B_s^2}$ given E_s. As

$$\sqrt{2C_s} \mid E_s = e_s \sim \sqrt{2C_s} \mid VE_s = e_s\,,$$

the conditional distribution does not depend on e_s and hence $\sqrt{2C_s}$ is independent of E_s and D_s.

ACKNOWLEDGEMENTS

The authors want to express their gratitude to Jan Pedersen for fruitful discussions. This research was supported by MINDLab and Centre for Stochastic Geometry and Advanced Bioimaging, supported by the Villum Foundation.

REFERENCES

Barndorff-Nielsen OE, Schmiegel J (2004). Lévy based tempo-spatial modeling; with applications to turbulence. Uspekhi Mat Nauk 159:63–90.

Cruz-Orive LM (2005). A new stereological principle for test lines in three-dimensional space. J Microsc 219:18–28.

Dufour JM, Roy R (1976). On spectral estimation for a homogeneous random process on the circle. Stoch Proc Appl 4:107–20.

Gual-Arnau X, Cruz-Orive LM (2000). Systematic sampling on the circle and the sphere. Adv Appl Prob SGSA 32:628–47.

Gundersen HJG (1988). The nucleator. J Microsc 151:3–21.

Hansen LV, Thorarinsdottir TL, Gneiting T (2011). Lévy particles: Modelling and simulating star-shaped random sets. Research report 4, CSGB, Department of Mathematical Sciences, Aarhus University. Submitted.

Hellmund G, Prokešová M, Jensen EBV (2008). Lévy-based Cox point processes. Adv Appl Prob SGSA 40:603–29.

Hobolth A, Jensen EBV (2002). A note on design-based versus model-based variance estimation in stereology. Adv Appl Prob SGSA 34:484–90.

Hobolth A, Pedersen J, Jensen EBV (2003). A continuous parametric shape model. Ann Inst Statist Math 55:227–42.

Holm H, Alouini MS (2004). Sum and difference of two squared correlated Nakagami variates in connection with the McKay distribution. IEEE Trans Commun 52:1367–76.

Jensen EBV, Gundersen HJG (1993). The rotator. J Microsc 170:35–44.

Jensen JL (1995). Saddlepoint Approximations. Oxford: Clarendon Press.

Jónsdóttir KY, Hoffmann LM, Hobolth A, Jensen EBV (2006). On variance estimation in circular systematic sampling. J Microsc 222:212–6.

Jónsdóttir KY, Rønn-Nielsen A, Mouridsen K, Jensen EBV (2013). Lévy based modelling in brain imaging. Scand J Stat, in press.

Jónsdóttir KY, Schmiegel J, Jensen EBV (2008). Lévy-based growth models. Bernoulli 14:62–90.

Rajput R, Rosinski J (1989). Spectral representation of infinitely divisible processes. Prob Theory Relat Fields 82:451–87.

Schneider R (1993). Convex Bodies: The Brunn-Minkowski Theory. Cambridge: Cambridge University Press.

FORTHCOMING MEETINGS

2013

11th European Congress of Stereology and Image Analysis (ECS 2013) & 5th Workshop 3D Imaging, Analysis, Modelling and Simulation of Macroscopic Properties
Kaiserslautern, Germany
July 8–12
http://www.mathematik.uni-kl.de/~ecs/

ICSIA 2013, 3rd International Conference on Signal, Image Processing and Applications
Barcelona, Spain
August 10–11
http://www.sie-edu.sg/icsia/cfp.htm

MC 2013, Microscopy Conference 2013
Regensburg, Germany
August 25–30
http://mc2013.dge-homepage.de/

EMAG 2013, The Electron Microscopy and Analysis Group Conference
York, UK
September 3–6
http://emag-iop.org

ICIP 2013, IEEE International Conference on Image Processing
Melbourne, Australia
September 15–18
http://www.ieeeicip.org/

Bioimaging 2013, 2nd International Symposium in Applied Bioimaging - from Molecule to Men
Porto, Portugal
October 3-4
http://www.bioimaging2013.ineb.up.pt/

2014

23rd Australian Conference on Microscopy and Microanalysis & 2014 International Conference on Nanoscience and Nanotechnology
Adelaide, Australia
February 2–6
http://www.aomevents.com/ACMMICONN

Inter/Micro 2014, 65th Annual Applied Microscopy Conference
Chicago, IL, USA
July 14–18
http://www.mcri.org/home/section/101/inter-micro

Microscopy & Microanalysis 2014 - Annual Meeting of the Microscopy Society of America and the Microbeam Analysis Society
Hartford, CT, USA
August 3–7
http://www.microscopy.org/events/events.cfm

IMC 2014, 18th International Microscopy Congress
Prague, Czech Republic
September 7–12
http://www.imc2014.com/

2014	ICIP 2014, IEEE International Conference on Image Processing Paris, France October 27–30 http://www.icip2014.com/

Stereology courses

1. Bern, Schweiz, August and September, 2013
   http://www.stereology.unibe.ch/

2. Cambridge, England, 1st–4th September, 2013
   http://onlinesales.admin.cam.ac.uk/browse/extra_info.asp?compid=1&modid=2&prodid=654&deptid=206&catid=373

3. Sandbjerg Manor, Sønderborg, Denmark, 24th–25th September, 2013
   https://service.health.au.dk/modules/Course/mypage/coursecalendar.

In the summer of 2015, the International Society for Stereology will organize its fourteenth international conference.

This is by all means the major event for the advancement of stereology, image analysis and related disciplines.

After Beijing in October 2013, we really look forward to receive passionate proposals from all continents.

If, you want to meet this challenge and organize a memorable congress, you are invited to send a proposal by September 30th to:

Dr. Claudia REDENBACH
redenbach@mathematik.uni-kl.de
ISS Secretary, Mathematics Department
University of Kaiserslautern
Postfach 3049
67653 Kaiserslautern (Germany)

Guidelines to prepare an eligible proposal can be found on the society's website
http://www.stereologysociety.org

We really look forward to hearing from you!

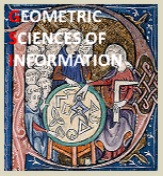

Société Mathématique de France

SMF

First International Conference

GSI'2013 - Geometric Science of Information

Paris – Ecole des Mines

28-30 August 2013

Web site: www.gsi2013.org

The objective of this SEE international Conference hosted by MINES ParisTech, is to bring together pure/applied mathematicians and engineers, with common interest for Geometric tools and their applications for Information analysis, with active participation of young researchers for deliberating emerging areas of collaborative research on "Information Geometry Manifolds and Their Advanced Applications".

Current and ongoing uses of Information Geometry Manifolds in applied mathematics are the following: Advanced Signal/Image/Video Processing, Complex Data Modeling and Analysis, Information Ranking and Retrieval, Coding, Cognitive Systems, Optimal Control, Statistics on Manifolds, Machine Learning, Speech/sound recognition, natural language treatment, etc., which are also substantially relevant for the industry.

This international conference will be an interdisciplinary event and will federate skills from Geometry, Probability and Information Theory to address the following topics among others:

- Geometric Statistics on manifolds and Lie groups
- Deformations in Shape Spaces
- Relational Metric and Discrete Metric Spaces
- Computational/Hessian Information Geometry
- Optimization on Matrix Manifolds
- Optimal Transport Theory
- Probability on Manifolds
- Divergence Geometry & Ancillarity
- Tensor-Valued Mathematical Morphology
- Machine/Manifold/Topology Learning
- Algebraic/Infinite dimensionnal/Banach Information Manifolds

Program chairs:
S. Bonnabel, J. Angulo, A. Cont, F. Nielsen, F. Barbaresco
Scientific committee: *F. Nielsen (Sony CSL, Ecole Polytechnique), M. Boyom (Montpellier Univ.), P. Byande (Montpellier Univ.), F. Barbaresco (Thales), S. Bonnabel (Mines), R. Sepulchre (Liege Univ.), M. Arnaudon (Bordeaux Univ.), G. Peyré (Paris-Dauphine Univ.), B. Maury (Paris-Sud Univ.), M. Broniatowski (UPMC Paris 6.), M. Basseville (CNRS, IRISA), M. Aupetit (CEA LIST), F. Chazal (INRIA), R. Nock (CEREGMIA - U. Antilles-Guyane), J. Angulo (Mines), N. Le Bihan (CNRS, Gipsa-Lab), J. Manton (Melbourne Univ.), A. Cont (IRCAM), A.Dessein (IRCAM), A.M. Djafari (SUPELEC), H. Snoussi (UTT Troyes), A. Trouvé (ENS Cachan), S. Durrleman (INRIA-ICM), X.Pennec (INRIA), J.F. Marcotorchino (Thales), M. Petitjean (INSERM, Paris 7), M. Deza (ENS Ulm)*
Local organization committee: *V. Alidor, J. Vieille, C. Moysan*

- **Yann OLLIVIER (Paris-Sud Univ.): "Information-geometric optimization: The interest of information theory for discrete and continuous optimization"**
- **Hirohiko SHIMA (Yamaguchi Univ.): "Geometry of Hessian Structures" dedicated to Prof. J.L. KOSZUL**
- **Giovanni PISTONE (Collegio Carlo Alberto): "Nonparametric Information Geometry"**
- **Shun-ichi AMARI (Riken): "Information Geometry and Its Applications: Survey"**

This workshop will produce two main scientific outcomes: Proceedings published in Lecture Notes by Springer for the conference and a Special Issue with accepted long papers published by Springer after the conference.

Lecture Notes in Computer Science
LNCS LNAI LNBI

The host: CSMS Supported by: IFSM

MAIN DEADLINES

1 September 2013 On-line abstract submission open
On-line registration available at the website

15 February 2014 Abstract submission deadline
Early registration deadline

1 July 2014 Standard registration deadline

SCIENTIFIC TOPICS

Instrumentation and Techniques

Electron optics and optical elements
High resolution TEM and STEM
Super-resolution light microscopy and nanoscopy imaging
Scanning electron microscopy
Analytical electron microscopy
Environmental electron microscopy
In-situ microscopic techniques and cryo-microscopies
Ultrafast and high-throughput microscopies
Electron and X-ray diffraction techniques
Electron tomography
Electron holography and lens-less imaging
Surface microscopy, spectromicroscopy and microspectroscopy
Focused ion beam microscopy and techniques
Scanning probe microscopy and near-field microscopies
X-ray, atom probe, neutron and other microscopies
Electron microscopy theory and simulations

Material Sciences

Nanoobjects and engineered nanostructures, catalytic materials
Carbon-based nanomaterials, nanotubes, fullerenes, graphenes
Thin films, coatings and surfaces
Metals, alloys and metal matrix composites
Ceramics and inorganic materials
Polymers and organic materials
Composite materials and hybrids
Semiconductors and materials for information technologies
Defects in materials and phase transformations
Porous and architectured materials
Amorphous and disordered materials, liquid crystals, quasicrystals
Magnetic, superconducting, ferroelectric and multiferroic materials
Materials in geology, mineralogy and archeology
Energy-related materials

Life Sciences

Live imaging of cells, tissues and organs
Structure and function of cells and organelles
High-resolution localization of molecular targets
and macromolecular complexes
Structure of macromolecules and macromolecular complexes
Cellular transport and dynamics
Microbiology and virology
Invertebrates and parasitology
Plant science and mycology
Gene-modified organisms and animal science
Human health and disease
Physiology and pathology
Advances in immunohistochemistry and cytochemistry
Embryology and development biology
Neuroscience

Interdisciplinary

Correlative microscopy in life and material sciences
Imaging mass spectrometry
Microscopy of single molecule dynamics
High-throughput microscopy and its applications in life and material sciences
Nanoparticles: Biomedical applications and bio-safety issues
Microscopy in forensic science
Microscopy in arts, restoration and archeology
Three-dimensional reconstructions in microscopy
Microscopic image analysis and stereology
Advances in sample preparation techniques
Multidisciplinary applications of progressive light microscopy imaging techniques
In-situ and environmental microscopy of processes in materials
and material reactions
Materials for medicine and biomaterials

CONGRESS SECRETARIAT

IMC 2014 Congress Secretariat, GUARANT International, Opletalova 22, 110 00 Praha 1, Czech Republic
Tel: +420 284 001 444 Fax: +420 284 001 448 E-mail: info@imc2014.com

Get more information and subscribe for updates at www.imc2014.com

THE CENTRE FOR MATHEMATICAL MORPHOLOGY (CMM) OF MINES PARISTECH ORGANIZES ITS 2013 SPECIALIZED TRAINING
"Image analysis: from theory to practice"
Paris, France
November 25th to 29th in Paris.

This course gives a comprehensive presentation of the morphological tools. Filtering and segmentation techniques are addressed, in 2D or 3D, for grey-tone or colour images, for still images or sequences as well as related techniques necessary to develop successful applications.

The course is organised during five full days, in a single week: lectures in the morning (9h-12h30), and practical training in the afternoon (14h-17h30). The practical training is performed with Morph-M, a multi-platform Mathematical Morphology software, developed and used in most CMM research projects**.** Demonstration will reinforce pedagogical aspects of the course.

The following topics will be addressed:

- Erosion, dilatation, opening, closing, granulometries, gradients, top-hat.
- Morphological filtering.
- Geodesy, connected operators, levellings.
- Segmentation : watershed, hierarchical segmentation, ultimate opening.
- 3D images, image sequences.
- Color processing.

All these notions will be illustrated through many examples, chosen from different application domains: bio-medicine, material science, scene analysis, multimedia, etc. The manipulation of images during practical training in the afternoons allows a full understanding of the studied notions.

You will find all the necessary information on our website:

http://cmm.ensmp.fr/ES/index_eng.htm.

Should you require any additional information, we are at your disposal.

Yours sincerely,

Catherine Moysan
Centre de Morphologie Mathématique
35 rue St Honoré
77300 Fontainebleau
Tél. 01 64 69 47 06 - Fax 01 64 69 47 07

ANNOUNCEMENT

ISS MEMBERSHIP APPLICATION/RENEWAL FOR 2013

The International Society for Stereology is a non-profit organization, whose purpose is to promote the exchange and dissemination of information about stereology among persons of various scientific disciplines and countries. The members' fees constitute the sole source of revenues of the ISS. In order to help us promote stereology, we would be pleased to welcome you as a member.

The ISS membership fee (regular members 50 €, students 25 €) includes a subscription to the journal 'Image Analysis and Stereology'

(http://www.ias-iss.org)

To renew your membership for 2013, please pay by bank transfer to the following account

IBAN: BE69 7320 1659 9478 BICCode: CREGBEBB

account owner International Society for Stereology

To pay via PayPal or to apply for a NEW membership, please send a message to

gemme@ulg.ac.be

You can also contact the ISS President and secretary/treasurer at:

gemme@ulg.ac.be

Eric Pirard
ISS President

Claudia Redenbach
ISS Secretary/treasurer

INSTRUCTIONS TO AUTHORS

Manuscript Submission. Manuscripts should be submitted electronically in PDF or Word format (first submission) and in Word or LaTex format (final submission) at Online Submission

www.ias-iss.org.

What To Submit:

- PDF or Word file of the Manuscript prepared by the author (obligatory at first submission)
- Cover Letter (obligatory)
- Supplementary Material (optional)
- Manuscript and Figures (obligatory at final submission of the accepted manuscript)
- Copyright Transfer Agreement (obligatory at final submission of the accepted manuscript)

E-mail correspondence. Should you require any information regarding article submission, please feel free to contact the Editorial Office at

ias@mf.uni-lj.si or editor.ias@mf.uni-lj.si

Guidelines for Manuscript Preparation. For rapid and accurate publication it is essential that manuscripts follow exactly the guidelines described below. Manuscript should be written in MS Word or LaTeX.

LaTeX. LaTeX style guide PDF file presents the instructions for preparing manuscripts for the Image Analysis & Stereology journal in LaTeX, and serves itself as an example of a LaTeX file conforming to the described form.

Language is English. Please be consistent. Use the same form of English (UK or American) throughout the text.

Length. Full-length research papers or full-length review articles including tables and figures with legends and references should not exceed 30 pages (30 lines per page, font size 12 pt, single column) or 15 typeset pages if prepared in LaTeX. Short research communications, reviews, communications or notes should not exceed 15 pages (7 typeset pages if prepared in LaTex) including tables and figures with legends.

Title. Short and to the point, not longer than 120 characters (including spaces); it should be written entirely in capital letters. Title should indicate the methodological aspects of the paper, which are of interest also for several fields of application. Include the running title with the surname of the first author with no more than 100 characters including spaces (*e.g.*, MACKAY CE *ET AL*: Comparison of MRI and physical sections).

Authors. Whole name(s) and family name of each author; no academic degrees or titles. Indicate who will be responsible for correspondence. Complete address of each author including an e-mail address.

Abstract. Not more than 250 words, summarizing the work presented in the manuscript, in 3rd person. Abstract should be understandable to a nonspecialist. It should be followed by a list of keywords (not more than 6) in alphabetical order.

Keywords should allow an appropriate classification of the paper in regard to the methodology and field of application.

Text. Sufficient details must be given to enable an interdisciplinary audience of the journal to understand the considered problem and methods. This includes a brief explanation of basic concepts, abbreviations and symbols, and, if available, a review paper as a reference. The manuscript should be structured with the following headings: Introduction, Materials and Methods, Results, Discussion,

Acknowledgements, and References. The headings should be placed on separate lines and written in capitals with no underlining. Avoid unnecessary subheadings. In the text do not underline words, do not use letters in bold type.

Conflict of interest. Any conflict or no conflict of interest, should be declared and described clearly and explicitly under a separate heading Conflict of Interest.

Methods which are of some general character should be emphasized. New methods or theoretical results should be given with an appropriate reasoning or derivation. Applications of methods are welcome. Appropriate real data, simulation or numerical results should be given to illustrate the main results.

Figures and Tables should be in a form and condition suitable for publication across a single column (8 cm) or a whole page (16 cm). The minimum font size of characters is 11. Figures and tables should be numbered consecutively in Arabic numerals (*e.g.*, Fig. 1; Table 1) and headed with a short title. Please mark in the manuscript (i.e., insert Fig. 1 or Table 1) where Tables or Figures should be placed in the text. Each figure and table should be accompanied by a self-explanatory legend. Please note that Figures and Tables should be included in manuscript file at first submission. At final submission (after the acceptance of the paper), all figures and tables should be uploaded as separate files, using the Supplementary files form. Ideally, all original files (manuscript, figures and tables) should be collected in a ZIP archive and uploaded as a Supplementary file. Maximum file size for upload is 50 MB.

Figures should be sent as TIFF or JPG files for raster images (bitmaps) or PS format for vector images. Files should have 600 dpi resolution for colour, greyscale images or black and white images.

Color Prints. A limited number of colour images is free of charge.

Equations should be on separate lines, with an extra spacing above and below. They should always be numbered, placing the number in brackets against the right hand margin. If a mathematical expression is to be included as a part of a sentence try to maintain the single line spacing by use of brackets (*e.g.*, (1-x)/(3-h)). Please, use an abbreviation (*e.g.*, Eq. 1) when discussing an equation in a sentence.

Units. SI units should be used wherever these exist for the parameter concerned. Units should be separated from values (*e.g.*, 5 µm, 2 mg, 1 min); exceptions are °, °C and % (*e.g.*, 90°, 37°C, 50%).

References in the text should be given in parentheses: *e.g.*, (Fish, 1971) when there is only one author; (Fish, 1971a,b) when an author has two references in the same year; (Fish, 1971; 1972) when an author has two references in different years; (Flesh and Fowl, 1954) when there are two authors; (Good *et al*., 1962) when there are more than two authors; (Flesh and Fowl, 1954; Good *et al*., 1962) when there is more than one reference; "as shown by Miller (1967), the ..." when author's name is part of a sentence. If the same authors have more than one publication in one year, then distinguish them, thus: 1985a, 1985b, etc. The reference list should be in alphabetical order and prepared according to the examples below:

Macpherson IA (1973). Soft agar technique. In: Kruse PF, Patterson IMK, eds. Tissue culture methods and application. Ch. 7. New York: Academic Press, 276-81.

Osler AG (1976). Complement: Mechanisms and functions. Englewood Cliffs: Prentice Hall, 51-5.

Solter NA, Wasserman SI, Austen KF (1976). Cold urticaria: release into circulation of histamine and eosinophilic chemotactic factor of anaphylaxis during cold challenge. N Engl J Med 294: 687-90.

Bengtsson S, Solheim BG (1992). Enforcement of data protection, privacy and security in medical information. In: Lun KC, Degoulet P, Piemme TE, Rienhoff O, eds. MEDINFO 92. Proceedings of the 7th World Congress on Medical Informatics, 1992 Sep 6-10; Geneva, Switzerland. Amsterdam: North-Holland, 1561-5.

"Personal communications", "unpublished observations" and "in preparation" should be given in the text and should not appear in the reference list.

Page Numbering. Pages in the manuscript should be numbered in Arabic numerals starting with the cover page.

Supplementary Materials are images, movies, data sets, and other files that support and augment the content of a manuscript. They are intended for publication only in the Online version of Image Analysis & Stereology. These materials should be referenced in the manuscript, and then accessed via the online Journal.

Supplementary Materials generally fall into the following categories
1. Extra Tables
2. Extra Figures
3. Datasets and Movies

Guidelines for submitting Supplementary Materials: Supplementary Materials must be submitted with the manuscript at the time of submission at Step 4 of the submission process. Supplementary Materials must be accompanied by a complete set of legends, one legend for each supplemental item. They must be referenced in the manuscript body at least once.

Cover letter This letter must be submitted in a text-box in the first step of the submission process. The letter must contain the following:

1. A brief statement of the significance of the paper.
2. Information about conflict of interest: Any conflict or no conflict of interest, should be declared and described clearly and explicitly.
3. A statement that all of the authors have directly participated in the planning, execution, or analysis of the study and resulting paper, and have read and approved the version submitted. **Please define the contribution of each author separately – without this statement the paper will not be processed for peer review!**
4. The authors confirm that the submitted manuscript has been either written or reviewed for quality of language by a native English speaker or alternatively professionally edited. Please note that manuscripts written in poor English will be rejected without possibility for further consideration.
5. (Optional) The contact information of any suggested reviewers (names, addresses, and e-mail).

Manuscripts submitted without a cover letter will not be processed for peer review.

Copyright Transfer Agreement After the manuscript has been accepted for publication in Image Analysis & Stereology the Copyright Transfer Agreement will be sent to the corresponding author. All authors engaged in the manuscript need to sign the form.

Submission Preparation Checklist As part of the submission process, authors are required to check off their submission's compliance with all of the following items, and submissions may be returned to authors that do not adhere to these guidelines.

1. The submission has not been previously published, nor is it before another journal for consideration (or an explanation has been provided in the Cover Letter).
2. The initial submission file is in PDF. The original manuscript files in Microsoft Word or LaTeX will be uploaded at final submission of the accepted manuscript.
3. The text adheres to the stylistic and bibliographic requirements outlined in the Author Guidelines, which is found in About the Journal.
4. References are in the correct format for this journal. All references listed in the reference list are cited in the text, and vice versa. Where available, DOI or URL for the references have been provided.
5. If the submission uses copyrighted material from other sources (including the Web), permission has been obtained for its use; the sources are appropriately noted in the text.
6. Submission is accompanied with a cover letter, written in accordance to the Author Guidelines, found in About the Journal.